Evaluation of Atmospheric Correction Algorithms over Turbid Waters

Editor: Cédric Jamet

Authors:

Sean Bailey, Sundarabalan V. Balasubramanian, Xianqiang He, Cédric Jamet, Thomas Schroeder, Palanisamy Shanmugam, Knut Stamnes and Sindy Sterckx

International Ocean Colour Coordinating Group (IOCCG)

IOCCG, Darmouth, Canada

Submit date: 08 July 2024

Evaluation of Atmospheric Correction Algorithms over Turbid Waters

Edited by:

Cédric Jamet

Report of an IOCCG Scientific Working Group chaired by Cédric Jamet with contributions from (in alphabetical order):

Sean Bailey, SAIC/NASA, USA

Sundarabalan V. Balasubramanian, Univ. Littoral Côte d'Opale, CNRS, Univ. Lille, UMR 8187 - LOG - Laboratoire d'Océanologie et de Géosciences, F-62930 Wimereux, France and XXXXX

Xianqiang He, State Key Laboratory of Satellite Ocean Environment Dynamics, Second Institute of Oceanography, Ministry of Natural Resources, China

Cédric Jamet, Univ. Littoral Côte d'Opale, CNRS, Univ. Lille, UMR 8187 - LOG - Laboratoire d'Océanologie et de Géosciences, F-62930 Wimereux, France

Thomas Schroeder, CSIRO, Australia

Palanisamy Shanmugam, Indian Institute of Technology, India

Knut Stamnes, Stevens Institute of Technology, USA

Sindy Sterckx, VITO, Belgium

Table of contents

IOCCG Technical Series Report on Evaluation of atmospheric correction over turbid waters

IOCCG WG members:

Sean Bailey, SAIC/NASA, USA

Sundarabalan V. Balasubramaniana, Univ. Littoral Côte d'Opale, CNRS, Univ. Lille, UMR 8187 - LOG - Laboratoire d'Océanologie et de Géosciences, F-62930 Wimereux, France and XXXXX

Xianqiang He, State Key Laboratory of Satellite Ocean Environment Dynamics, Second Institute of Oceanography, Ministry of Natural Resources, China

Cédric Jamet, LOG/ULCO, France, chair

Kevin Ruddick, REMSEM/RBINS, Belgium

Thomas Schroeder, CSIRO, Australia

Palanisamy Shanmugam, ITT, India

Knut Stamnes, Stevens Institute of Technology, USA

Sindy Sterckx, VITO, Belgium

Introduction

This IOCCG Technical report is the result of an IOCCG Scientific Working Group (WG) on the evaluation of atmospheric correction algorithms over optically-complex waters that started in 2014. This report aims at being a complementary updated report of the IOCCG report # 10 which primarily focused on open ocean waters and standard atmospheric correction algorithms.

Optically-complex waters, especially turbid waters, have been the focus of several research efforts in the past decades and the IOCCG working group felt it was time not only to provide a comprehensive evaluation of the most common atmospheric correction schemes used in the ocean color community but also to provide guidance to the end-users where to use a specific atmospheric correction algorithm depending on the predominant optical water type (OWT).

As the reader may already know, the atmospheric correction process is vital to get accurate ocean color radiometry, i.e. the remote sensing reflectance (R_{rs}). While this process is somewhat easy in open ocean waters (due to the fact that the ocean can be considered totally absorbing of Sunlight in the near-infrared spectral range), it is more complicated in optically-complex waters that are often encountered in coastal and inland waters.

Remote sensing of coastal and inland waters is difficult because:

- these areas are highly variable in space and time
- the surrounding can affect the signal measured by the remote sensor (straylight contamination or adjacency effects)
- the aerosols are non-maritime (e.g., dust, smoke) and can be absorbing. These conditions are not considered by most available atmospheric correction algorithms
- high values of total suspended matter (SPM) and/or high colored dissolved organic matter concentrations (CDOM) can be observed, which complicate the estimation of R_{rs}(NIR) and the correction of the Bidirectional Reflectance Distribution Function (BRDF). High concentrations of SPM can also saturate the remote sensor
- there are anthropogenic emissions such as NO_2 absorption in the Ultra-Violet (UV) and visible (VIS) parts of the spectrum overlapping with the absorption of CDOM

In this report, the WG decided to focus mainly on turbid waters (non-zero R_{rs}(NIR)). This is mainly due to the availability of long-term time series of in-situ measurements in these coastal areas. The evaluation of the atmospheric correction algorithms has been done using MODIS-AQUA images. It does not mean that this report is focused on MODIS-AQUA, it is just an application. The main reason why MODIS-AQUA has been chosen is that it was the only remote sensor to have short-wave infra-red (SWIR) bands over a long-time period when the WG started and MODIS-AQUA provides the longest time series of Ocean Color Radiometry (20-+ years). Since then, the Sentinel-3A and -B OLCI as well as S-NPP, NOAA-20 and NOAA-21 VIIRS sensors have been launched. However, we believe that the results of this evaluation can be applicable to OLCI and VIIRS as the wavelengths are very similar and the principles of most algorithms are not sensor dependent (only the quality of the sensor changes such as the Signal-to-Noise Ratio, SNR). NN-based algorithms, however, require sensor-specific training data. As the application of this report is on MODIS-AQUA, atmospheric correction algorithms using the 709 nm band (Moore et al., 1999) or the OLCI 1020 nm band (Gossn et al., 2019) were not included in this study.

After briefly presenting the different atmospheric correction algorithms included in the round-robin in Chapter 1, the three datasets used for the evaluation are presented in Chapter 2 and the definition of the match-ups and optical water types are provided in Chapter 3. Then the results based on these three datasets including sensitivity studies are presented in Chapters 4 and 5. The final Chapter 4 of this Technical Report discusses the environmental conditions that can occur and further complicate atmospheric correction when observing coastal and inland waters such as adjacency effects and absorbing aerosols, which have not been considered in the algorithm inter-comparison of this report.

I. Atmospheric correction over turbid waters

This chapter presents first the basis of the atmospheric correction and then the selected algorithms. The selection was based on availability of the algorithms, on the popularity of algorithms and on the willingness of the developers to share the code of their algorithm and/or to process the data. We tried to select algorithms that the community uses or is interested in and based on different hypotheses so we could investigate the sensitivity of the outputs to those hypotheses.

1) Principles of the atmospheric correction

The purpose of the atmospheric correction process is to remove the contribution of the atmosphere to the signal measured by the remote sensor, leading to the estimation of the remote-sensing reflectance R_{rs}, i.e. the ocean color radiometry. The signal measured by the remote sensor at the top-of-the atmosphere can be decomposed into several terms (Gordon and Wang 1994; Gordon, 1997, IOCCG, 2010; Mobley et al., 2016; Frouin et al., 2019):

$$L_{TOA}=L_R+L_a+L_{ra}+T.L_g+t.L_{wc}+t.L_w \quad (1)$$

with

- L_{TOA}, the radiance measured at the top of the atmosphere
- L_R, the radiance due to air molecules (Rayleigh scattering)
- L_a, the radiance due to aerosols (aerosols scattering)
- L_{ra}, the radiance due to the interaction between the aerosols and the air molecules (aerosols-Rayleigh scattering)
- L_g, the radiance due to specular reflection of Sunlight by the sea surface (Sun glint)
- L_{wc}, the radiance due to white caps
- L_w, the water-leaving radiance (the final parameter of interest)
- T, the direct transmittance
- t, the diffuse transmittance

The Rayleigh scattering, the whitecaps radiance, the Sun glint contributions as well as the gas absorption can be estimated from ancillary data (Mobley et al., 2016).

So, the atmospheric correction process aims at estimating the contribution of the aerosols using the Rayleigh-corrected radiance:

$$L_{rc}=L_{TOA}-L_R=L_a+L_{ra}+t.L_w=L_A+t.L_w \quad (2)$$

The reflectance is often used to develop AC and to process ocean color images. Eq.2 can be rewritten, considering that $\rho=\pi L/F_0.\cos\theta_0$ with F_0; the extraterrestrial solar irradiance and, θ_0 the solar zenith angle.

Over open ocean waters, the water-leaving radiance can be considered negligible (black pixel assumption) in the near-infrared (NIR) bands so the Rayleigh-corrected measured signal is only due to aerosols. Using the NIR bands allows the aerosol models and optical properties to be estimated. But in more optically-complex waters, such as turbid waters (which are the main focus of this report), the black pixel assumption is not true anymore, as there is a contribution of the water to the top-of-atmosphere signal (IOCCG, 2010). To overcome this challenge, many atmospheric correction algorithms were developed in the past two decades for the major past and current ocean color remote

sensors. They can be grouped into five different categories: (1) assignment of the hypothesis on the NIR aerosols or water contributions (Hu et al., 2010; Ruddick et al., 2010; Vanhellemont and Ruddick, 2021), (2) use of the shortwave infrared bands (Wang and Shi, 2005; Wang and Shi, 2007; Wang, 2007; Shi and Wang, 2009; Chen et al., 2014; He and Chen, 2014; Gossn et al., 2021), (3) use of blue or ultra-violet (UV) bands (He et al., 2004; Oo et al., 2008; He et al., 2012; Giao et al., 2021a, 2021b; Liu et al., 2021; Wang et al., 2021), (4) correction or modeling of the non-negligible ocean in the NIR (Moore et al., 1999; Siegel et al., 2000; Stumpf et al., 2003; Lavender et al., 2005; Bailey et al., 2010; Ahn and Park, 2020; Xue et al., 2021; Wang et al., 2022), and (5) coupled ocean/atmosphere inversion based on artificial neural networks (Doerffer and Schiller, 2007; Schroeder et al., 2003, 2007, 2022; Fan et al., 2017, 2020, 2021; Ssenyonga et al., 2021) or optimization techniques (Chomko et al., 2003; Stamnes et al., 2003; Jamet et al., 2004, Brajard et al., 2006, 2012; Kuchinke et al., 2009; Steinmetz et al., 2011; Ibrahim et al., 2022).

2) Choice of algorithms

The algorithms used in this evaluation have been chosen based on their availability and use by the ocean color community. The goal was not to have all published atmospheric correction algorithms but to have algorithms that are based on different hypotheses to try to understand how these hypotheses impact the accuracy of the retrievals.

a) NASA standard AC (Bailey et al., 2010)

The Bailey et al. (2010) approach estimates the NIR reflectance through an iterative approach based on a reflectance retrieval in the red (670 nm). The initial condition is based on the black-pixel assumption, from which an estimate of the visible water reflectance is obtained. The backscatter coefficient in the red (at 670 nm) is estimated by inversion of the reflectance. This inversion assumes that the dominant absorption component is water, although an empirical estimate of the particulate absorption is employed as well. The backscatter slope parameter defined by Lee et al. (2010) is derived from the retrieved reflectance spectrum and is used to propagate the backscatter coefficient from the red into the NIR (748 and 869 nm, for MODIS-AQUA). This propagated backscatter coefficient is used in a forward model to retrieve an estimate of water reflectance in the NIR which is subtracted from the signal prior to the next iteration of the atmospheric correction. The iteration is continued until convergence of the red reflectance or a maximum iteration threshold is reached.

b) NIR-SWIR AC (Wang and Shi, 2007)

This method combined the historic NASA atmospheric correction algorithm (Gordon and Wang, 1994) for the open ocean waters with an atmospheric correction method using the Short-Wave-Infra-Red (SWIR) bands (Wang and Shi, 2005). The switch is based on a turbidity index (Shi and Wang, 2007). The principle of the SWIR AC is the same as that of Gordon and Wang (1994), which considers the ocean to be black in the SWIR bands. The epsilon parameter is calculated in the SWIR bands and then used to estimate the aerosol optical properties and models. The version used in this report is the version implemented in the SeaDAS software.

c) MUMM AC (Ruddick et al., 2000)

This algorithm replaces the assumption that the water leaving radiance is zero in the NIR by the assumptions of spatial homogeneity of the 748/869 nm ratios for aerosol and water-leaving reflectances over the subscene of interest. The ratio of ρ_A reflectances at 748 and 869 nm is named ε and is considered as a calibration parameter to be calculated for each sub-scene of interest. In addition,

the ratio of ρ_w at 748 and 869 nm, named α, is also considered as a calibration parameter and is fixed to a value of 1.945 for the MODIS-AQUA sensor (Ruddick et al., 2000, 2006). These assumptions are used to extend to turbid waters the Gordon and Wang (1994) algorithm (thereafter referred to as GW94). Using the definition of α and ε, the equations defining $\rho_A(748)$ and $\rho_A(869)$ become:

$$\rho_A(748) = \varepsilon(748,869).\left[\frac{\alpha.\rho_{cor}(869)-\rho_{cor}(748)}{\alpha-\varepsilon(748,869)}\right] \quad (3)$$

$$\rho_A(869) = \left[\frac{\alpha.\rho_{cor}(869)-\rho_{cor}(748)}{\alpha-\varepsilon(748,869)}\right] \quad (4)$$

The atmospheric correction algorithm can be summarized thus:

(1) Enter the atmospheric correction routine (i.e. GW94) to produce a scatter plot of Rayleigh-corrected reflectances $\rho_{cor}(765)$ and $\rho_{cor}(785)$ for the region of study. Select the calibration parameter ε on the basis of this scatter plot.

(2) Reenter the atmospheric correction routine with data for Rayleigh-corrected reflectances $\rho_{cor}(748)$ and $\rho_{cor}(869)$ and use Eqs. (2) and (3) to determine $\rho_A(748)$ and $\rho_A(869)$, taking account of non-zero water-leaving reflectances.

(3) Continue as for the standard GW94 algorithm.

d) SWIRE AC (He and Chen, 2014)

A new shortwave infrared extrapolation (SWIRE) method is used to correct the NIR bands. The Rayleigh-corrected reflectances in the SWIR bands (1.24, 1.64, and 2.13 µm) are used to determine an exponential function with respect to wavelength, which is used to correct the NIR bands (0.748 and 0.869 µm) for sediment scattering and hence estimate the aerosol scattering reflectances in these bands. The Rayleigh-corrected reflectances can be fitted with an exponential function in the NIR and SWIR bands for open ocean waters while only in SWIR for turbid waters. The fitted function is called the extrapolated Rayleigh-corrected reflectance and is used to calculate the epsilon parameter. Then the Gordon and Wang AC approach is applied.

e) NN-based OC-SMART AC (Fan et al., 2017, 2021)

OC-SMART is based on Multi-Layer Neural Networks (MLNNs) methods for retrieval of aerosol optical depth (AOD) and R_{rs} values (Fan et al., 2017, 2021). A radiative transfer model for the coupled atmosphere-water system (AccuRT, Stamnes et al., 2018) is used to simulate the top of the atmosphere (TOA) radiances (L_{toa}) and R_{rs} values simultaneously, and this dataset is used to train MLNNs to determine AOD and R_{rs} values directly from L_{toa} radiances. Application of these MLNN algorithms to MODIS Aqua images in several coastal areas shows that they are accurate (no negative R_{rs} values), robust, and resilient to contamination due to Sun glint or adjacency effects of land and cloud edges. These MLNN algorithms are very fast once the neural networks have been properly trained and are therefore suitable for operational use. A significant advantage is that they do not need SWIR bands, which implies significant cost reduction for dedicated OC missions. These MLNN algorithms have been extended for application to extreme atmospheric conditions (i.e. strongly polluted continental aerosols) over turbid coastal water by including appropriate aerosol and ocean bio-optical models to generate the required training datasets. Application of these extended MLNN algorithms to VIIRS images over areas with extreme atmospheric and marine conditions (such as the Yellow Sea and the East China Sea) shows very promising results.

OC-SMART is freely available at http://www.rtatmocn.com/oc-smart/ and version v1.0 was used.

f) NN-based FUB AC (Schroeder et al., 2007)

The Artificial Neural Networks (ANN) algorithm deployed for this working group comparison was adapted to an approach previously developed by Schroeder (2005) Schroeder et al. (2007a) for MERIS but on the basis of a different learning algorithm. In contrast to atmospheric correction algorithms based on the *Black-Pixel* assumption - the ANN method does not attempt to decouple atmospheric and oceanic light fields. Rather, it performs the correction directly on a pixel-by-pixel basis from the full TOA spectrum.

A scalar version of the Matrix-Operator-MOdel (MOMO) was used to simulate the light field in a coupled ocean-atmosphere system and to build a large database of more than 20 million reflectance spectra at the bottom of the atmosphere (BOA) and at the top of the atmosphere (TOA). A variety of different sun and observing angles as well as different concentrations of oceanic and atmospheric constituents were considered in the simulations, which were subsequently used to develop the ANN algorithm. The only difference in this study is the adoption of MODIS spectral band settings. ANN was implemented as a 3-layer perceptron and in this application represents a nonlinear function mapping between the TOA spectral reflectance (input) and the BOA spectral reflectance (output). Within such a network each layer consists of neurons – which are the basic, linear or non-linear, processing nodes. Each neuron is connected with each neuron of the next layer by a weight. The weights – in statistical term the free parameters - were estimated during a supervised learning procedure during which the network "learned" to associate an input vector $\vec{x}$ with a given output vector $\vec{y}$. The weights between two layers can be expressed as a matrix **W** and the complete analytic function represented by a 3-layer network is then given by the following equation:

$$\vec{y} = S_2 \times \{W_2 \times S_1(W_1 \times \vec{x})\} \quad (5)$$

In our case the activation function is linear for the output layer (S_2) and non-linear (logistic) for the hidden layer (S_1). Training of a network consisted of minimizing the sum of squared errors between all input and output training vectors by adapting the weight matrices ($\mathbf{W_1}$,$\mathbf{W_2}$) iteratively using a Limited Memory Broyden-Fletcher-Goldfarb-Shanno algorithm. The training data were extracted randomly from the simulated data base. In detail, we extracted 100,000 spectra at BOA and TOA, of which one input vector $\vec{x}$ consisted of the full TOA spectral reflectance in MODIS ocean color bands 8-16 (λ=[412.5-869.5] nm), the angular information of the observing geometry transformed into Cartesian coordinates, the cosine of the sun zenith cos(θ_0) and the surface pressure *P*.

The associated output vector $\vec{y}$ contains the log-transformed remote sensing reflectance at BOA in the MODIS bands 8-15 (λ=[412.5-748] nm) and aerosol optical thickness (AOT) at four AERONET wavelengths (440, 550, 670 and 870 nm).

As there are no direct pathways to obtain the optimum network architecture, a series of 170 different networks were trained by varying the number of hidden layers, the number of neurons on the hidden layers and several noise levels. Training was stopped for each configuration after 1,000 iteration cycles over the full training data set of 100,000 spectra and monitored by the Mean Squared Error (MSE). The best performing network was selected based on the results obtained from match-up analysis – the ANN method therefore had the advantage in this AC comparison that it was tuned to the in-situ

measurements. Its architecture consisted of 14 input nodes, 80 hidden layer neurons, and 12 neurons for the output layer trained with a random noise level of 0.8% for the TOA reflectance, 0.1% for each the geometry inputs and 2% for the surface pressure.

g) Polymer AC (Steinmetz et al., 2011)

The Polymer atmospheric correction algorithm (Steinmetz et al, 2011) is an advanced full-spectrum coupled spectral matching algorithm for ocean colour. It was originally developed for the atmospheric correction of MERIS observations, in particular in presence of sun glint contamination, but has been extended to many other sensors. This algorithm relies firstly on a water reflectance model based on Park and Ruddick (2005) having only two unknown parameters, the chlorophyll concentration and the particulate backscattering, to represent a large variability of the oceanic and coastal waters. Secondly, it relies on a model for the atmosphere and surface reflectance, whose particularity is to be represented as a linear combination of three terms: $\rho_{ag}(\lambda) = T_0(\lambda)c_0 + c_1\lambda^{-1} + c_2\rho_{mol}(\lambda)$. This analytical formulation does not rely on aerosol models and allows fitting accurately not only the aerosol reflectance, but also other complex atmospheric and surface effects, in particular the residual sun glint. This formulation essentially relies on the general fact that atmospheric effects in $\rho_{ag}(\lambda)$ are spectrally smooth.

An iterative optimization scheme is applied pixel by pixel, using the Nelder-Mead simplex method, to retrieve the water and atmospheric parameters simultaneously. The final values of $\rho_{ag}(\lambda)$ are subtracted from the observation, so that the final water reflectance is not the output of the model, and preserves fine spectral features from the observation.

Polymer is freely available for non-commercial purposes on www.hygeos.com/polymer.

h) Gaussian-spectral relationships SS14 (Singh and Shanmugam, 2014)

To mitigate the correction by the water constituents, a correction factor, κ, is introduced which is defined in terms of band ratio to determine the extent of radiance contributed by various optically active water constituents in the NIR bands (Singh and Shanmugam, 2014). In the spectral shape parameter (SSP) aerosol correction algorithm (Singh et al., 2019), κ helps in identifying the primary water types by obtaining the spectral slopes from Rayleigh-corrected reflectance (ρ_{rc}) band ratios. The algorithm calculates the spectral slopes using the Violet (415 nm), Blue (490 nm), Green (536 nm), Red (667 nm), Fluorescence (684 nm), and NIR (747 nm) bands. At the initial stage of κ estimation algorithm, its value is assumed as unity for all the pixels, assuming the reflectance image covers only the clear open oceanic water pixels, and its value gets updated based on the ratios of the Rayleigh-corrected reflectance ρ_{rc} as follows:

1. The ratio of green and blue bands is sensitive to suspended sediments, and for such water types, the value of κ, i.e., will always be greater than one.

2. Likewise, the ratio between red and violet becomes greater than one for extremely turbid waters.

3. The ratio between the two red bands, becomes useful for low-moderate productive waters and helps to identify in-water blooms.

4. The ratio between NIR and red bands, helps to identify the pixels dominated by floating algal blooms in highly productive waters.1

Once the spectral band ratios are determined for all the pixels, the maximum value is considered the final value of κ and used to correct water contribution in the NIR bands. Unlike the standard aerosol estimation algorithm(Gordon and Wang, 1994), which assumes the water signal as zero at the NIR wavelengths and often overestimates aerosol contributions at the visible wavelengths in turbid and productive waters (Singh and Shanmugam, 2014; Wang and Shi, 2007), this SSP algorithm does not follow such assumptions and is found to be highly accurate in aerosol estimation even in such water types where the water signal is usually non-zero at the NIR wavelengths (Banerjee and Shanmugam, 2021).

i) UV-based AC (He et al., 2012)

The principle of the UV-AC algorithm is based on the fact that the water-leaving radiance at ultraviolet wavelengths can be neglected as compared with that at the visible light wavelengths or even near-infrared wavelengths in most cases of highly turbid waters due to the strong absorption by detritus and colored dissolved organic matter. In turbid waters, the water-leaving radiances increase largely at longer VIS wavelengths and NIR due to strong particulate scattering, yet the strong combined absorption by detritus and CDOM contents cause a rapid decrease of the water-leaving radiance at the UV band. In extremely turbid waters, the water-leaving radiance at the UV band is much lower than at the NIR band. In such turbid coastal and inland waters, the UV band is more suited than the NIR band for estimating the aerosol scattering radiance. Since most of the launched satellite ocean color sensors do not have UV bands, the shortest wavelength (usually at 412 nm) can be used. Taking the SeaWiFS as an example, the shortest waveband (412 nm) was used as the reference to estimate the aerosol scattering radiance. Assuming that the water-leaving reflectance at 412 nm can be neglected in highly turbid waters, we can estimate the aerosol scattering reflectance at 412 nm [$\rho_a(412) = \rho_{rc}(412)$]. Based on the extrapolation method, the aerosol scattering reflectance at 865 nm can be estimated as follows:

$$\{\rho_a(865) = \rho_{rc}(412)\ exp\ [c(412 - 865)] \tag{6}$$

$$c = \frac{ln\ [\rho_{rc}(765)/\rho_{rc}(865)]}{(865-765)} \tag{7}$$

For applications to satellite images from past and current sensors, the UV-AC algorithm was applied to the whole target region which may include not only the turbid waters, but also some of the clear waters. To avoid the overestimation of the aerosol scattering reflectance in clear waters, the $\rho_a(865nm)$ is limited to $\rho_{rc}(865nm)$. Specifically, when the estimated $\rho_a(865nm)$ is larger than the $\rho_{rc}(865nm)$, it will be set as $\rho_{rc}(865nm)$. Finally, a "white" aerosol scattering reflectance spectrum is assumed for the entire target region, and the aerosol scattering reflectance at all bands will be equal to $\rho_a(865nm)$.

j) NN-based C2RCC AC (Doerffer and Schiller, 2007)

C2RCC is based on artificial neural networks (ANN) (Doerrfer and Schiller, 2007; Doerrfer, 2015). The ANN are trained with large datasets of simulated top of standard atmosphere reflectances and water-leaving reflectances. The model of the atmosphere is based on analysis of AERONET data of coastal sites. The water-leaving reflectances are simulated using the Hydrolight software for a large number of different water constituents, including mineral particles, different species of phytoplankton, bacteria and protozoa, detritus. Then, the trained neural nets perform the inversion of the top of

standard atmosphere to estimate the water-leaving reflectances. C2RCC is similar to FUB and OC-SMART.

II. Datasets

1) Satellite dataset

For this round-robin comparison, we applied all AC to MODIS-AQUA satellite images. As mentioned, it's just an application and not an exercise dedicated to MODIS-AQUA. The MODIS-AQUA L1B were downloaded from the OPBG website: https://oceancolor.gsfc.nasa.gov/. Reprocessing version 2014.0 was used. Even if new reprocessings were released since version 2014, we do not expect the new reprocessing to change the conclusions of this report. The L1B were processed using the software SeaDAS v7.3.2 to get the Rayleigh-corrected reflectance.

2) Simulated dataset

An enhanced version of the simulated dataset developed in the IOCCG report #10 has been developed to encompass a wide range of coastal waters.

The AccuRT radiative transfer code has been used to generate the radiances at the top-of-the-atmosphere, at the top-of-the-atmosphere corrected from the gas absorptions, at the top-of-the-atmosphere corrected from the gas absorptions and the Rayleigh scattering, the aerosol and the coupled Rayleigh/aerosol radiances, the diffuse transmittance and the remote-sensing reflectance (Jin and Stamnes, 1994; Stamnes et al., 2017, 2018). The AccuRT simulations were checked against Hydrolight simulations and found to agree very well. Extensive comparisons with computations provided by Dr. X. He was also been done. These efforts are documented in the supplementary material (see files IOCCG-WG_SIM_DATA_v28 and IOCCG-WG_RTM_COMPARISONS_v16.pdf).

The aerosol models are from Ahmad et al. (2010) and the inherent optical properties (IOPs) of the seawater from the COASTCOLOUR project (Ruddick et al., 2010). In order to cover a wide range of atmospheric and water conditions, we generated 20,000 cases as follows:

For each ocean case, 4 aerosol models were randomly selected among the 80 possible models (4 aerosol configurations x 5,000 water configurations). For each of these 20,000 cases, the geometry angles were randomly selected in the following ranges:

- Solar zenith angle (θ_s = SZA): 0-70°

- Viewing zenith angle (θ_v = VZA): 0-70°

- Relative azimuth angle ($\Delta\Phi = \Phi_s - \Phi_v$ = RAA): 0-180°.

The sun-glint geometry was avoided in the simulations.

The simulated dataset has been generated for SeaWiFS, MODIS-AQUA, VIIRS, MERIS and OLCI sensors. The following files are therefore provided with the dataset:

1. "sensor_InputParameter.txt",

2. "sensor_RadianceTOA.txt",

3. "sensor_RadianceTOA gas corrected.txt",

4. "sensor_RadianceTOA gas&rayleigh corrected.txt"

5. "sensor_Rrs.txt"

6. "sensor_aerosolReflectance.txt"

7. "sensor_diffuseTransmittance.txt"

The file "sensor_InputParameter.txt" contains the input parameters for the simulations. The format is as follows: SZA, VZA, RAA, $\tau_a(865)$, angstrom(443/865), f_v, RH, CHL, CDOM, MIN.

The file "sensor_RadianceTOA.txt" includes the top of atmosphere (TOA) radiances for each simulation case. These radiances were simulated with atmospheric gas absorption, Rayleigh scattering, aerosol and ocean IOPs turned on. The number of columns in the file depends on the sensor. For example, there are 16 columns in each line for MODIS, one for each band.

The file "sensor_RadianceTOA_gas_corrected.txt" contains "atmospheric-gas-corrected" TOA radiances for each simulation case. The radiances were simulated with atmospheric gas absorption turned off, but Rayleigh scattering, aerosol, and ocean IOPs turned on. The number of columns in the file depends on the sensor. For example, there are 16 columns in each line for MODIS, one for each band. These radiances can be used to validate the atmospheric gas correction algorithm.

The file "sensor_RadianceTOA_gas&rayleigh_corrected.txt" contains "atmospheric-gas-and- Rayleigh-corrected" TOA radiances using data from "sensor_RadianceTOA_gas_corrected.txt" with the pure Rayleigh scattering radiances subtracted. The pure Rayleigh scattering radiances were simulated with only Rayleigh scattering turned on, and atmospheric gas absorption, aerosol, and ocean IOPs turned off. The number of columns in the file depends on the sensor. For example, there are 16 columns in each line for MODIS, one for each band.

The file "sensor_Rrs.txt" contains the remote sensing reflectance R_{rs} for each simulation case. The remote sensing reflectance was computed as the water leaving radiance divided by the downwelling irradiance just above the surface. The water leaving radiance was simulated as described in Appendix C. The simulation was done with atmospheric gas absorption, Rayleigh scattering, and aerosols turned on in the atmosphere. This file includes two sets of data. The first half of the columns include nadir R_{rs} values (θ_0= SZA; θ= 0; $\Delta\Phi$ = 0) and the second half of the columns include the corresponding R_{rs} values at the geometry of (θ_0= SZA; θ = VZA; $\Delta\Phi$ = RAA). For example, there are 32 columns in the file "MODIS Rrs.txt". The first 16 columns contain the nadir R_{rs} values (SZA, 0, 0) for each band, while the next 16 columns contain the corresponding R_{rs} values at geometry (SZA, VZA, RAA). The second set of R_{rs} data can be used to validate the atmospheric correction algorithm. The first set of R_{rs} data can be used to validate the BRDF algorithm.

The file "sensor_aerosolReflectance.txt" contains the reflectance for aerosols (no molecular scattering or absorption, but including molecule/aerosol interactions) at the TOA. These reflectances were computed as $Radiance_{aerosol}(TOA)/E_d(TOA)$, and correspond to $\rho_a + \rho_{ra}$ as defined by Gordon and Wang (1994). But please note that there is a factor of π difference: Gordon and Wang (1994) defines the reflectance as $\rho = \pi L/(\mu_0 F_0)$, while we use $\rho = L/(\mu_0 F_0)$. Then R_{rs} is calculated as $R_{rs} = \rho_w/\pi$.

The file "sensor_diffuseTransmittance.txt" contains two-way diffuse transmittance for aerosols and molecular scattering (no molecular absorption).

More information about the simulated dataset is provided in Supplementary material. The dataset is freely available at the following link: http://www.ioccg.org/data/ioccg2024_turbid_water_simulated_data.d/

3) In-situ dataset

An in-situ dataset of remote-sensing reflectance and aerosol optical thickness has been gathered. These measurements are from the AERONET-Ocean Color network (Zibordi et al., 2009b, 2021). AERONET-OC is the ocean component of the Aerosol Robotic Network (AERONET, Holben et al., 1998). It is a system of autonomous sun photometers deployed around the globe (mainly in the northern hemisphere as shown in Figure 1) providing normalized water-leaving (nL_w) radiance and the aerosol optical thickness at several wavelengths in the visible.

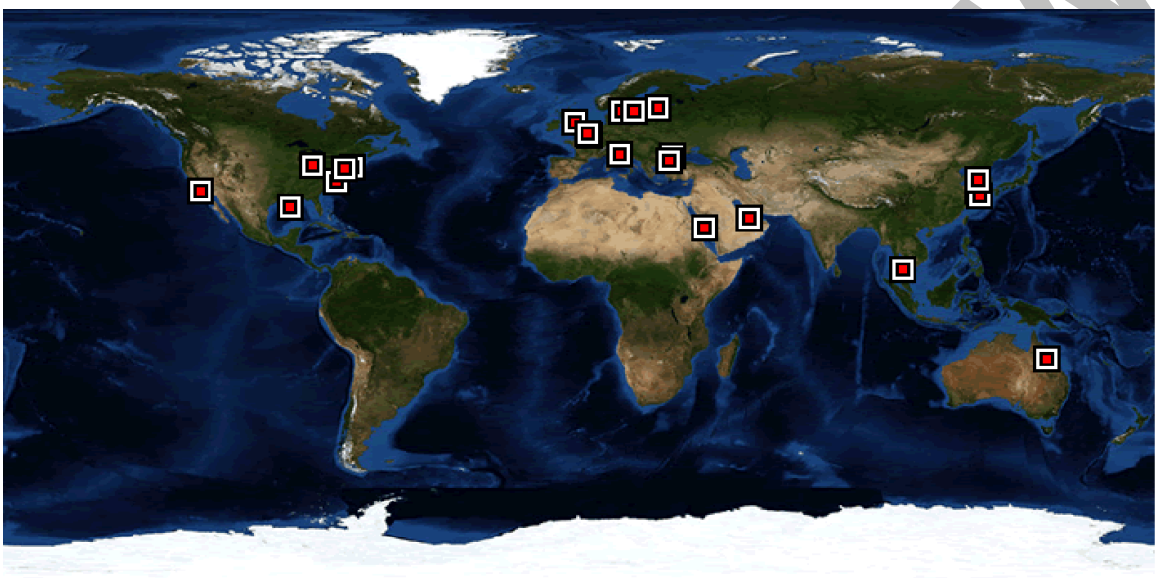

Figure 1: Maps of the global AERONET-OC stations. The stations used in this report are mentioned in table 1

The advantage of using AERONET-OC data is that the production of the measurements is standardized with identical systems and protocols, with calibration from a single source or method and with processing using the same code (Zibordi et al., 2006; 2009; 2021). Moreover, measurements are taken several times a day, every day (optimally), which leads to a high number of potential match-ups.

Table 1 presents the different AERONET-OC stations used for the match-ups exercise.

Table 1. AERONET-OC stations names, locations and number of data used

S.No	Station	Year	Lat	Lon	N
1	VENICE	2002-2015	45.31	12.50	1192
2	COVE	2006-2015	36.90	-75.71	38
3	GDLT	2005-2015	58.59	17.46	268
4	HLT	2006-2015	59.94	24.92	261
5	MVCO	2004-2015	41.30	-70.55	412
6	GLORIA	2011-2015	44.59	29.35	186
7	LUCINDA	2009-2015	-18.50	146.30	83
8	ZEEBRUGGE	2014	51.36	3.12	16

Characteristics of the selected AERONET-OC stations are provided in Feng et al. (2008); Zibordi et al. (2009, 2015, 2021); Mélin (2022); Van der Zande (2016).

III. Match-ups analysis

1) Extraction of the match-ups

The validation of the algorithms has been done through a classic match-ups analysis (Bailey and Werdell, 2006). The following steps have been taken:

1. 1-hour interval between the satellite overpass and the AERONET-OC measurement
2. Extraction over a 3-by-3-pixel box centered over the AERONET-OC station
3. 6 out of 9 pixels must be valid over the 3-by-3-pixel box
4. A coefficient of variability, CV, is calculated, i.e. standard deviation/mean values over the 3-by-3-pixel box for $R_{rs}(547)$
5. A match-ups is valid if $CV(R_{rs}(547))<0.2$
6. Calculation of the mean values over the valid pixels
7. AERONET-OC data are filtered for taking into account only turbid waters as defined by Robinson et al. (2003): $R_{rs}(667)>0.0012\ sr^{-1}$

Concha et al. (2021) studied the impact of the different steps taken into this study. Their conclusion is that the chosen validation protocol impacts the statistics and those statistics may be difficult to compare with other studies using another validation protocol.

Considering these different steps, out of 2456 possible match-ups, only 889 remained.

2) Statistical parameters

To quantitatively evaluate the performances of the algorithms the following statistical parameters have been calculated:

- Relative Error: $RE = \frac{1}{N}\sum\left(100 \times \frac{|R_{rs}^{sat} - R_{rs}^{obs}|}{R_{rs}^{obs}}\right)$
- Root-Mean-Square-Error: $RMSE = \sqrt{\left(\frac{\sum\left(R_{rs}^{sat} - R_{rs}^{obs}\right)^2}{N}\right)}$
- Slope (a) and intercept (b) of the regression line
- Bias: $BIAS = \frac{1}{N}\sum\left(100 \times \frac{R_{rs}^{sat} - R_{rs}^{obs}}{R_{rs}^{obs}}\right)$
- Correlation coefficient R^2
- Overall error (Pahlevan et al., 2021): $\beta = 100 \times sign(z)\left(10^{|Z|} - 1\right)$ with $Z = Median\left(log_{10}\left(\frac{R_{rs}^{sat}}{R_{rs}^{obs}}\right)\right)$
- Relative Bias in log (Pahlevan et al., 2021): $\alpha = 100 \times (10^{Y} - 1)$ with $Y = Median\left(\left|log_{10}\left(\frac{R_{rs}^{sat}}{R_{rs}^{obs}}\right)\right|\right)$

3) Statistical evaluation of the retrieved spectra

Aside from the classic statistical parameters, investigations on the shape of the retrieved spectra were also performed through three parameters:

- Quality Assurance Score (QAS; Wei et al., 2016): this parameter provides quantification of the full R_{rs} spectrum quality of retrievals with regards to reference spectra. The value has to be 1.
- χ^2: this parameter provides information about the full spectrum relative errors. The value has to be 0.
- the Spectral Angle Mapper (SAM; Kruse et al., 1993; Keshava, 2004): this parameter indicates the mean of the full spectrum difference between the retrieved R_{rs} and *in-situ* R_{rs} spectra. The value has to be 0°.

We considered the following wavelengths: 412, 443, 488, 531, 547, 667 nm.

Other parameters could be used to provide information about the spectral shape of the R_{rs} retrievals. For instance, Dierssen et al. (2022) developed the Quality Water Index Polynomial (QWIP).

4) Ranking of the algorithms using a score scheme

The scoring scheme developed by Müller et al. (2015) was used to classify the algorithms. It is based on the values of the slope and intercept of the linear regression, BIAS, RMSE, RE R^2 and the number of valid match-ups. The highest possible score is the number of parameters times the number of wavelengths. In our case, the maximal value is 42. This scheme converts the statistical parameters into relative scores.

The score is calculated as follows:

$$S_{tot} = \sum_{i=1}^{6} \left(S_{slope}(\lambda_i) + S_{intercept}(\lambda_i) + S_{RMSE}(\lambda_i) + S_{REL.ERR}(\lambda_i) + S_{bias}(\lambda_i) + S_{R^2}(\lambda_i) + S_N(\lambda_i)\right)$$

S_x is the normalized value between 0 and 1 for each statistical parameter. 0 is given to the lowest value and 1 to the highest value. As the highest value for one given parameter is not always the best one, the normalization has to be adapted to the statistical parameter. For instance, the correlation coefficient is the best when equal to 1 but for the relative error, the best value is 0%. To consider this, s_x was calculated as:

$$s_x(\lambda_i) = \frac{|X(\lambda_i)| - max(|X(\lambda_i)|)}{min(|X(\lambda_i)|) - max(|X(\lambda_i)|)} \quad (8)$$

for x=intercept or BIAS.

s_x was calculated as:

$$s_x(\lambda_i) = \frac{X(\lambda_i) - max(X(\lambda_i))}{min(X(\lambda_i)) - max(X(\lambda_i)|)} \quad (9)$$

for x=RE or RMSE.

s_x was calculated as:

$$s_x(\lambda_i) = \frac{X(\lambda_i)}{max(X(\lambda_i))} \quad (10)$$

for x=N.

s_x was calculated as:

$$s_x(\lambda_i) = \frac{X(\lambda_i) - min(X(\lambda_i))}{max(X(\lambda_i)) - min(X(\lambda_i))} \quad (11)$$

for x=R^2.

s_x was calculated as:

$$s_x(\lambda_i) = \frac{|1 - X(\lambda_i)| - max(|1 - X(\lambda_i)|)}{min(1 - |X(\lambda_i)|) - max(1 - |X(\lambda_i)|)} \quad (12)$$

For x=slope.

5) Optical water classes

For the classification of the optical water types proposed in this study, a self-organizing map (SOM, Kohonen, 2013) was used to initially cluster the AERONET-OC and simulated datasets in the SOM topology map. Each sample was assigned to a node (cluster center), which represents one of the possible classes. For the input layer, the normalized remote sensing reflectance (R_{rs}) at 412, 443, 488, 531, 547 and 667 nm was used. The normalization was done following the equation:

$$R_{rs\_n}(\lambda) = \frac{2}{3}(R_{rs}(\lambda) * \overline{\overline{R_{rs}}}(\lambda))/\sigma(R_{rs}(\lambda)) \quad (13)$$

where R_{rs_n} is the normalized R_{rs} spectra, $\overline{\overline{R_{rs}}}$ and $\sigma(Rrs)$ are the mean and the standard deviation of the R_{rs} spectra for the whole training dataset, respectively. The classification of the optical water types (OWT) is based on the simulated dataset.

The other initial parameters for SOM were a 100 training steps for initial covering the input space, an initial neighborhood size of 3, a hexagonal pattern for the topology function and a layer-based distance function between the layer's neurons given their position.

A 3-by-3 architecture was initially selected for the SOM, but it was deemed not sufficient to cluster the different shapes of R_{rs}. The N-by-N architecture was increased one by one, in which a 6x6 architecture was deemed sufficient. For each of the 6x6 nodes, the mean R_{rs} spectrum was calculated and this spectrum was used as a reference to regroup the classes based on the spectral shape. For each sample and each mean spectrum (36), the Euclidean distance was calculated and the minimum distance was used to select the corresponding class for each sample.

The regrouping was done manually and the 36 mean spectra were assigned to 9 classes based on the shape of each mean spectrum (Figure 2). At this step, an emphasis was given on the contribution of each IOP to the R_{rs} spectrum (Figures 3 and 4). The classes 1 and 2 correspond to highly turbid waters, with a clear plateau between 547 and 667 nm, due to the high backscattering in the red, especially for class 1. For the classes 3 to 4, R_{rs} has a more triangular shape, with a maximum at 547 nmand with R_{rs} in the blue lower than the R_{rs} in the red, an indication of waters with mixed composition. From classes 5 to 9, there is a gradual increase in the impact of the pure water absorption and scattering properties to the R_{rs} spectrum, switching the peak from green towards the blue and with an increase in the magnitude of R_{rs} in the blue wavelengths.

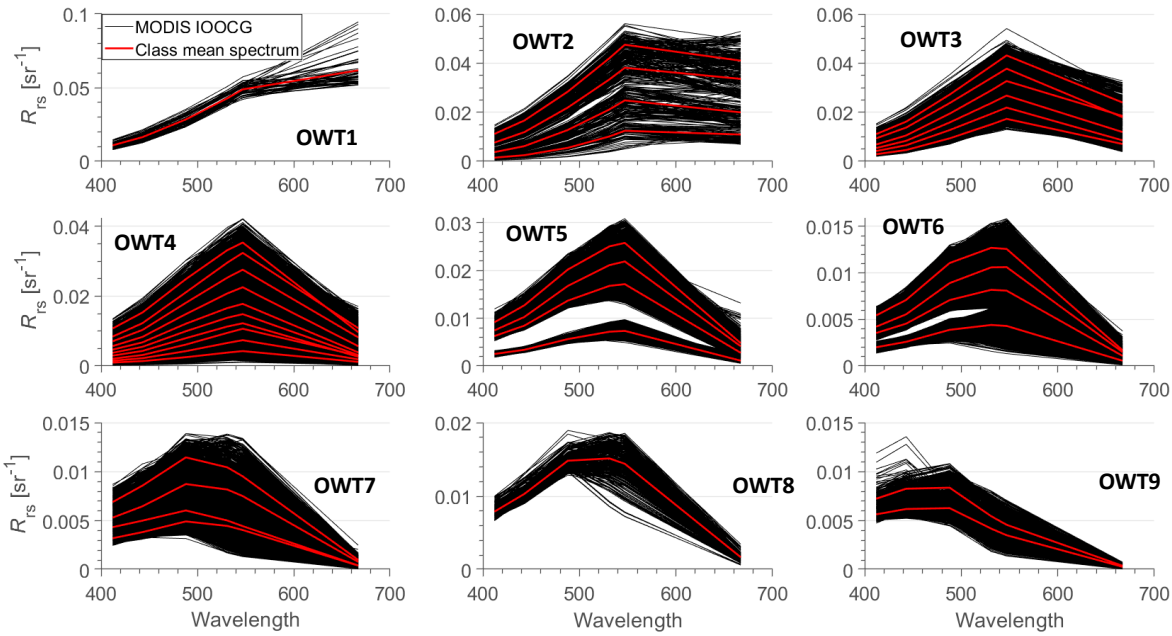

Figure 2: R_{rs} spectra and reference spectra (red) for each optical water class based on the simulated dataset.

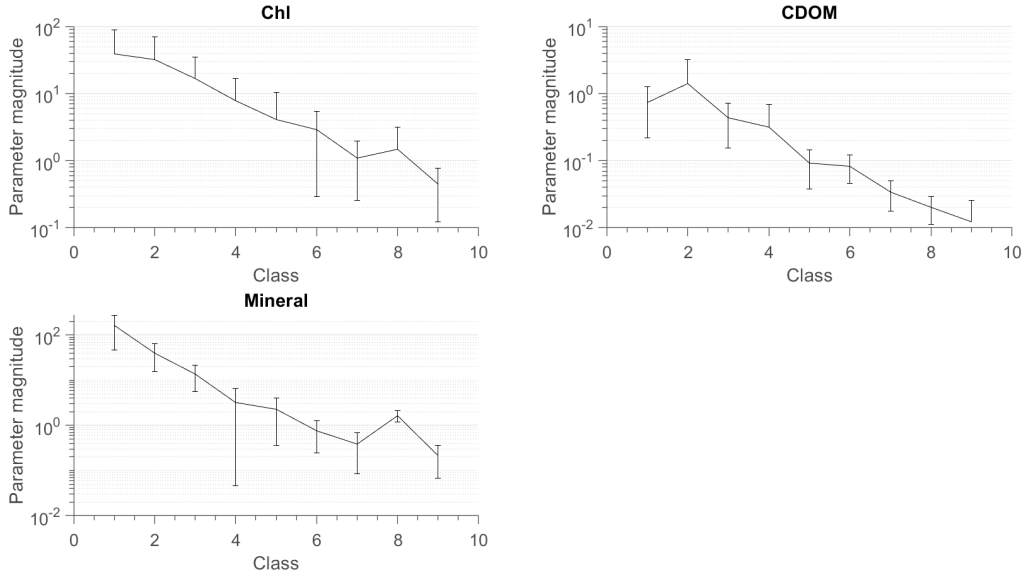

Figure 3: Values of Chlorophyll-a, CDOM and mineral concentrations for each optical water class.

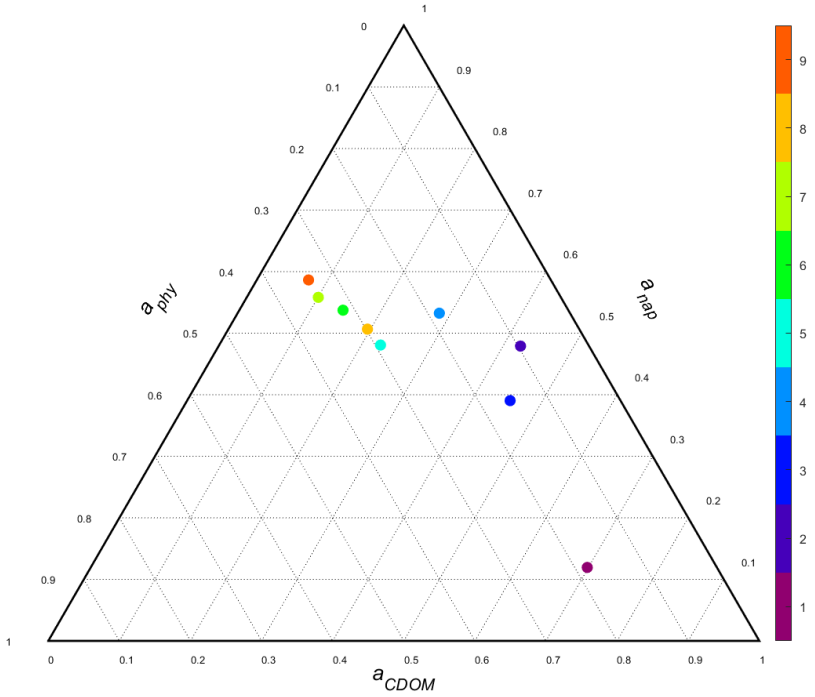

Figure 4: Triangle diagram showing the distribution of the nine optical water class depending of the values of $a_{CDOM}(443)$, $a_{phy}(443)$ and $a_{nap}(443)$.

This classification was applied to the match-ups dataset. Figure 5 shows the reference spectra and the AERONET-OC spectra for each class on the individual match-ups dataset and Figure 6 is the same but for the common match-ups dataset. For both datasets, there are no AERONET-OC spectra attached to the most turbid waters (Class 1 and 2). For the common AERONET-OC dataset, there are no spectra attached to the most oligotrophic waters (Class 9).

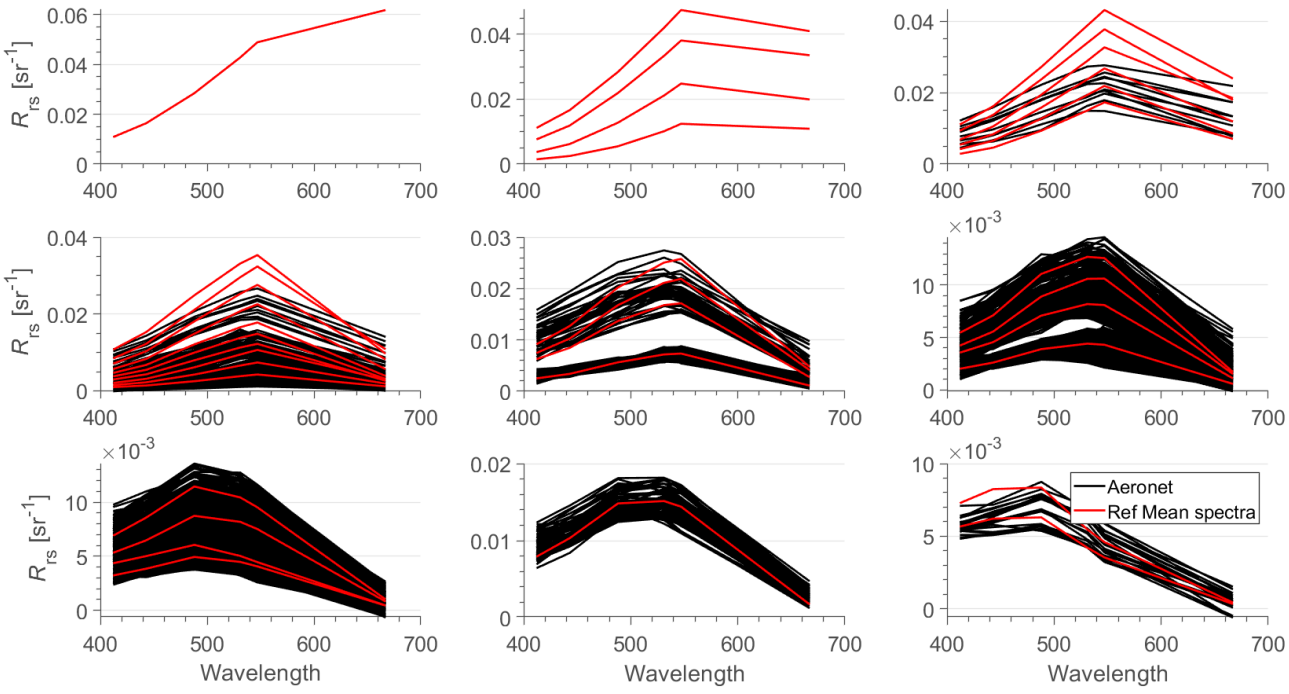

Figure 5: Spectra and reference spectra (red) for each optical water class based on the AERONET-OC total dataset. The OWTs are the same as in Figure 4. From upper-left to lower-right: OWT1 to OWT9.

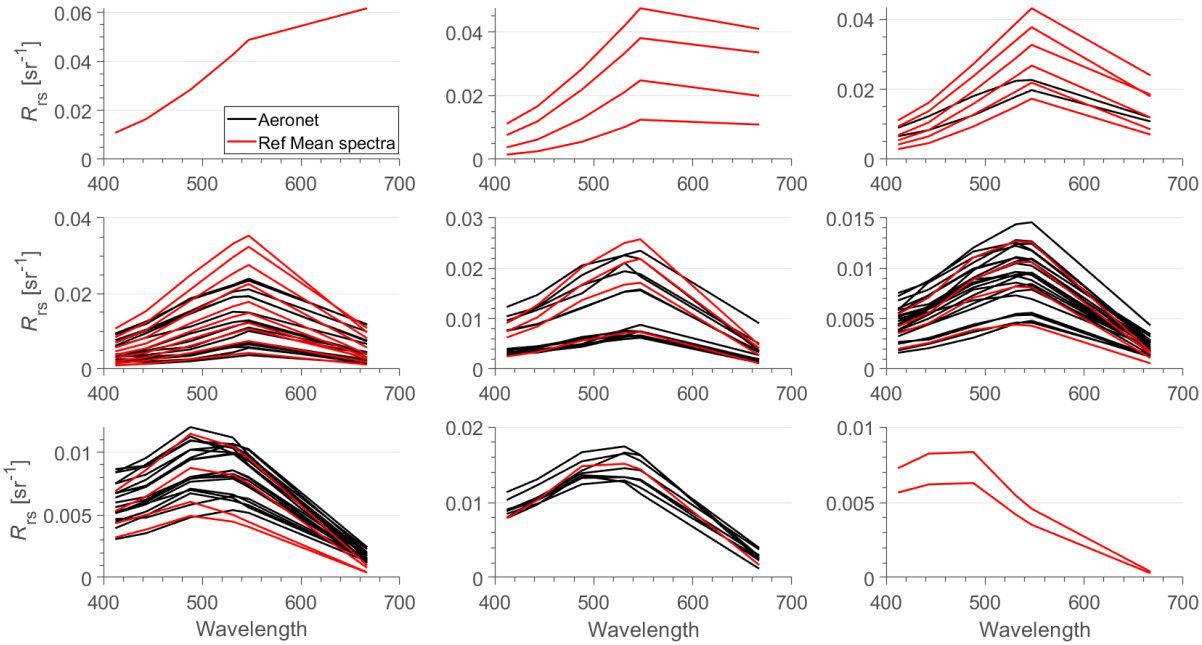

Figure 6: Spectra and reference spectra (red) for each optical water class based on the AERONET-OC common dataset. The OWTs are the same as in Figure 4. From upper-left to lower-right: OWT1 to OWT9.

Considering only turbid waters (Robinson et al., 2003), the number of spectra per optical water types for each dataset is provided in the following table.

Table 2: Number of spectra per optical water types

DATASET	OWT1	OWT2	OWT3	OWT4	OWT5	OWT6	OWT7	OWT8	OWT9
Individual match-ups	0	0	10	174	165	302	177	66	2
Common match-ups	0	0	2	16	14	24	19	8	0
Simulated	53	369	1656	6399	1898	1577	113	236	0

IV. Results on the in-situ dataset

In this section, we present the evaluation results over the in-situ dataset for two sets: the global match-ups dataset and the common match-ups dataset. The first dataset provides information about global statistics and more specifically focused on the number of match-ups and the second dataset allows us to directly compare the statistics of the retrievals from the ten AC algorithms.

1) Individual spectra match-ups analysis

We present here the results for all individual match-ups obtained by each AC algorithm. Figure 7 shows the scatterplots of the satellite-retrieved R_{rs} vs the AERONET-OC *in-situ* values for all ten AC algorithms and Table 3 provides the statistical results.

The first result concerns the number of match-ups. As shown in Table 3, the number of match-ups highly varies from 242 for SWIRE to 896 for SS14 with a total possible number of 896. Moreover, negative R_{rs} can also be retrieved in the blue or red bands. It is the case for NASA (6 at 412 nm), NIRSWIR (3 at 412 nm), MUMM (19 at 412 nm and 5 at 443 nm) and Polymer (1 at 488, 531 and 547 nm) while the other AC algorithms do not provide any negative results. These two parameters are of high importance notably for time series globally or regionally. We expect to use the AC algorithm providing the highest number of match-ups without any negative values.

Figure 7 shows that high scattering is observed at 412 and 443 nm for all AC while the scattering around the 1:1 line decreases at 488, 531 and 547 nm. It is a common behavior of AC algorithms (Goyens et al., 2013; Melin, 2022). At 412 and 443 nm, some algorithms provide high values of R_{rs} for low AERONET-OC R_{rs} (UV, SS14, SWIRE). Note that UV uses the band at 412 nm to correct from the atmosphere and is considered as the reference wavelength. This explains why the Rrs retrievals at this band are not as accurate as the ones from other AC.

This translates into the statistical parameters (Table 3). The relative errors are the highest at 412 (between 30% for FUB and 95% for SS14) and 443 nm (between 20% for NASA and NIRSWIR and 78% for SWIRE) and the lowest at 531 and 547 nm (between 12% for NASA and NIRSWIR and 30% for FUB and SWIRE at 531 nm and between 11% for NASA and 28% for FUB at 547 nm). The high scattering at 412 and 443 nm can also be seen with the slope of the regression lines with the lowest values (between 0.29 for SWIRE and 0.86 for NASA at 412 nm and between 0.61 for UV and 0.96 for NASA at 443 nm) and the closest values of the slope to 1 are obtained at 531 and 547 nm (between 0.75 for SS14 and 1.00 for NASA and NIRSWIR at 531 nm and between 0.78 for SS14 and 1.02 for NASA and NIRSWIR at 547 nm). The values of the slope are correlated with the values of the correlation coefficient R^2 with the lowest values at 412 (between 0.13 for UV and 0.74 for Polymer) and 443 nm (between 0.39 for UV and 0.87 for NASA) and the highest values at 531 (between 0.70 for C2RCC and 0.92 for NASA) and 547 nm (between 0.71 for UV and 0.92 for NASA). As the UV algorithm is mainly applicable for highly turbid waters, it is not surprising that its performance is not so good for the obtained matchups since the in-situ dataset only cover low-to-moderately turbid waters.

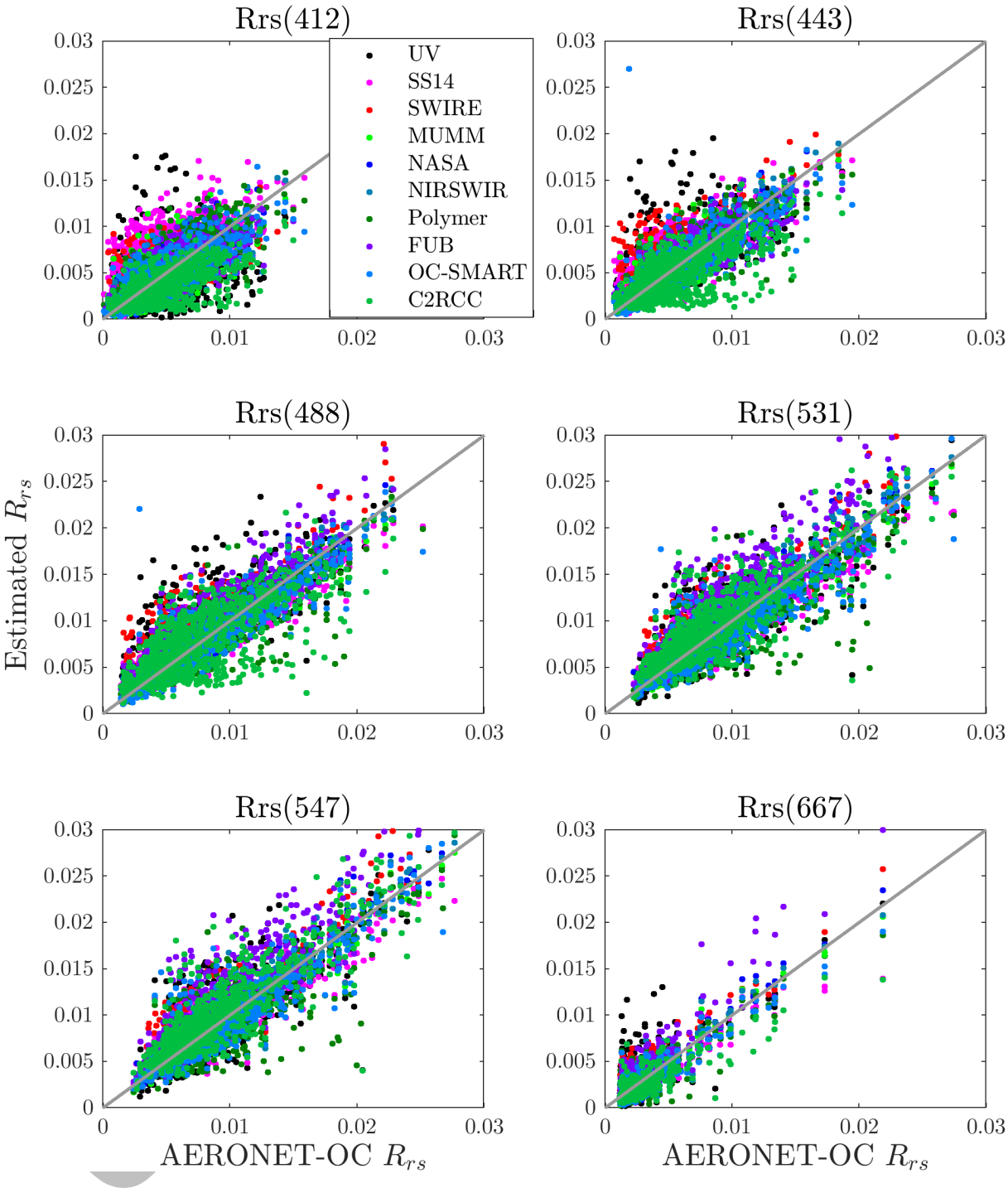

Figure 7: Scatterplots of the AC estimated R_{rs} vs in-situ R_{rs} from 412 (top left) to 667 nm (bottom right). The individual scatterplots are provided in Appendix I.

Table 3: The statistical results derived from the remote sensing reflectance, R_{rs} derived from various atmospheric correction algorithms and AERONET data R_{rs} (*RE* - mean relative error, *RMSE* – root mean square error, R^2- regression, *β- overall error, α - relative bias in log, Nvm*- number of valid data/model/wavelength).

	RE(%)	*RMSE (sr^{-1})*	Slope *(sr^{-1})*	Intercept	Bias *(sr^{-1})*	R^2	*β (%)*	*α (%)*	*Nvm*	*#<0*
		NASA STD AC Model								
R_{rs} *(412)*	33	0.00155	0.86	0.00052	0.00015	0.70	-14	74	510	6
R_{rs} *(443)*	20	0.00121	0.96	0.00028	0.00004	0.87	-0.5	38	510	0
R_{rs} *(488)*	13	0.00121	0.98	0.0000	-0.00011	0.93	-6	25	510	0
R_{rs} *(531)*	12	0.00137	1.00	-0.00025	-0.00019	0.92	-9	24	510	0
R_{rs} *(547)*	11	0.00138	1.02	0.00039	-0.00015	0.92	-8	23	510	0
R_{rs} *(667)*	24	0.00076	1.08	0.00043	-0.00023	0.92	-45	69	510	0
		NIRSWIR AC Model								
R_{rs} *(412)*	32	0.00159	0.84	0.00072	-0.00005	0.69	-9	68	431	3
R_{rs} *(443)*	20	0.00130	0.95	0.00047	0.00014	0.86	2	38	431	0
R_{rs} *(488)*	13	0.00130	0.98	0.00015	-0.00003	0.92	-4	25	431	0
R_{rs} *(531)*	12	0.00145	1.00	-0.00013	-0.00010	0.91	-7	26	431	0
R_{rs} *(547)*	12	0.00146	1.02	-0.00028	-0.00005	0.91	-6	23	431	0
R_{rs} *(667)*	25	0.00081	1.05	-0.00033	-0.00018	0.90	-41	68	431	0
		MUMM AC Model								
R_{rs} *(412)*	40	0.00200	0.68	0.000123	-0.000324	0.50	-25	93	412	19
R_{rs} *(443)*	25	0.00158	0.83	0.000902	-0.000117	0.76	-12	50	412	5
R_{rs} *(488)*	16	0.00145	0.91	0.000498	-0.000266	0.89	-15	34	412	0
R_{rs} *(531)*	13	0.00150	0.95	0.000176	-0.000337	0.90	-13	28	412	0
R_{rs} *(547)*	13	0.00144	0.97	-0.000007	-0.000250	0.91	-11	26	412	0
R_{rs} *(667)*	29	0.00082	0.99	-0.000321	-0.000336	0.90	-62	97	412	0
		SS14 AC Model								
R_{rs} *(412)*	95	0.00323	0.64	0.0394	0.00226	0.40	171	179	896	0
R_{rs} *(443)*	50	0.00227	0.69	0.00298	0.00122	0.65	64	82	896	0
R_{rs} *(488)*	26	0.00185	0.73	0.00250	0.00038	0.82	14	45	896	0
R_{rs} *(531)*	20	0.00190	0.75	0.00248	0.00022	0.82	10	38	896	0
R_{rs} *(547)*	18	0.00182	0.78	0.00222	0.00026	0.82	9	35	896	0
R_{rs} *(667)*	23	0.00081	0.79	0.00037	-0.00014	0.82	-17	57	896	0
		SWIRE AC model								
R_{rs} *(412)*	73	0.00273	0.29	0.00375	0.00017	0.13	-13	122	242	0
R_{rs} *(443)*	78	0.00331	0.64	0.00457	0.00239	0.53	106	107	242	0
R_{rs} *(488)*	52	0.00333	0.86	0.00370	0.00253	0.77	76	76	242	0
R_{rs} *(531)*	30	0.00277	0.94	0.00231	0.00178	0.82	41	43	242	0
R_{rs} *(547)*	27	0.00275	1.01	0.00165	0.00175	0.84	36	43	242	0
R_{rs} *(667)*	60	0.00153	1.02	0.00099	0.00106	0.85	111	118	242	0

	RE (%)	*RMSE (sr^{-1})*	Slope *(sr^{-1})*	Intercept	Bias *(sr^{-1})*	*R^2*	*β (%)*	*α (%)*	*Nvm*	*#<0*
		UV AC Model								
R_{rs} (412)	67	0.00327	0.35	0.0026	-0.00042	0.11	-40	244	620	0
R_{rs} (443)	51	0.00291	0.61	0.0029	0.00069	0.39	22	142	620	0
R_{rs} (488)	34	0.00286	0.81	0.0025	0.00103	0.65	15	107	620	0
R_{rs} (531)	23	0.00259	0.85	0.0012	-0.00011	0.71	-38	135	620	0
R_{rs} (547)	23	0.00359	0.90	0.0009	-0.000005	0.71	-44	137	620	0
R_{rs} (667)	53	0.00164	0.92	0.0003	-0.00013	0.59	-69	333	620	0
		Polymer AC Model								
R_{rs} (412)	31	0.00146	0.84	0.0012	0.00046	0.74	31	55	892	0
R_{rs} (443)	21	0.00146	0.81	0.0012	0.00012	0.80	12	38	892	0
R_{rs} (488)	17	0.00183	0.79	0.0014	-0.00022	0.81	-2	30	892	1
R_{rs} (531)	16	0.00220	0.78	0.0014	-0.00057	0.76	-12	33	892	1
R_{rs} (547)	16	0.00216	0.82	0.0013	-0.00029	0.75	-6	29	892	1
R_{rs} (667)	28	0.00089	0.85	0.00003	-0.00033	0.80	-47	76	892	0
		FUB AC model								
R_{rs} (412)	30	0.00152	0.70	0.0013	-0.00014	0.66	-1	70	721	0
R_{rs} (443)	25	0.00162	0.73	0.0013	-0.00023	0.74	-4	62	721	0
R_{rs} (488)	31	0.00244	0.94	0.0019	0.00144	0.81	53	60	721	0
R_{rs} (531)	30	0.00310	1.10	0.0013	0.00220	0.83	62	64	721	0
R_{rs} (547)	28	0.00327	1.16	0.0007	0.00216	0.81	59	61	721	0
R_{rs} (667)	28	0.00119	1.30	-0.00045	0.00029	0.84	11	63	721	0
		OC-SMART AC model								
R_{rs} (412)	35	0.00209	0.70	0.0011	-0.00026	0.49	-21	76	895	0
R_{rs} (443)	23	0.00165	0.80	0.00087	-0.00027	0.75	-14	49	895	0
R_{rs} (488)	15	0.00162	0.87	0.0075	-0.00028	0.85	-11	28	895	0
R_{rs} (531)	14	0.00179	0.87	0.00068	-0.00055	0.85	-16	27	895	0
R_{rs} (547)	13	0.00171	0.93	0.00044	-0.00022	0.85	-9	24	895	0
R_{rs} (667)	29	0.00082	0.88	-0.00014	-0.000430	0.86	-74	86	895	0
		C2RCC AC model								
R_{rs} (412)	37	0.00225	0.48	0.0012	-0.00114	0.43	-71	122	786	0
R_{rs} (443)	34	0.00247	0.54	0.0017	-0.00084	0.46	-27	99	786	0
R_{rs} (488)	35	0.00295	0.67	0.0027	0.00024	0.53	23	86	786	0
R_{rs} (531)	25	0.00259	0.84	0.0023	0.00082	0.70	31	56	786	0
R_{rs} (547)	23	0.00253	0.92	0.0018	0.00103	0.74	29	46	786	0
R_{rs} (667)	29	0.00106	0.71	0.0002	-0.00050	0.77	-88	98	786	0

Figure 8 shows the variation of the relative errors and the root-mean-square error as a function of wavelength. For the relative error, we can observe the "smiley" shape, already mentioned by Jamet et al. (2011), Goyens et al. (2013) and Melin (2022). However, we can observe that some algorithms are less sensitive to wavelength in term of RMSE (NIRSWIR, NASA and OC-SMART) while others are very sensitive to the wavelengths (FUB, Polymer, UV, SWIRE, C2RCC).

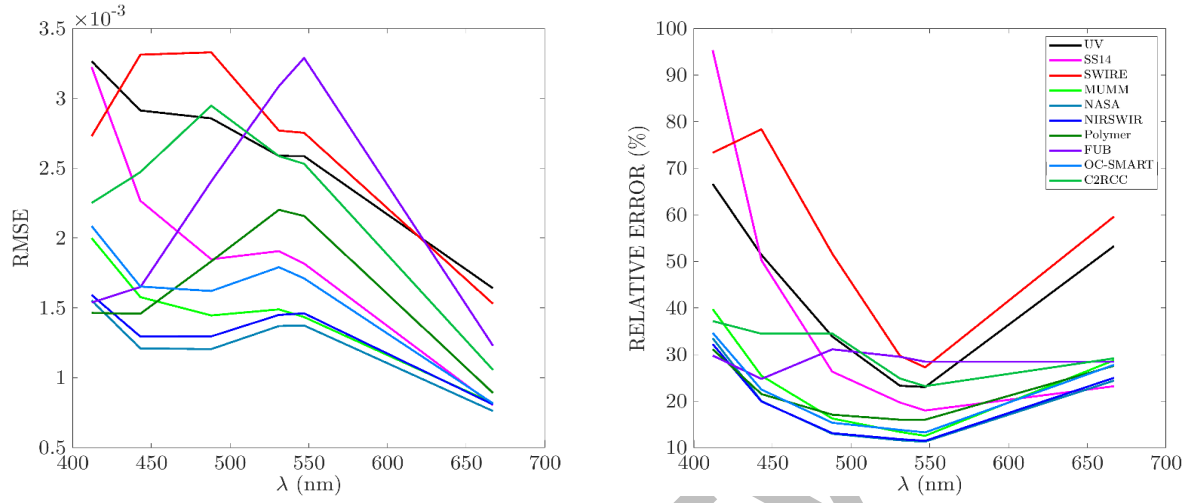

Figure 8: (a) Variation of the relative error as a function of wavelength, (b) Variation of the RMSE as a function of wavelength

Figure 9 shows a spider plot of all statistical parameters (except the intercept of the regression line). This sort of figure provides a general view of the performance of each algorithm. The values of the statistical parameters are normalized in such a way that the algorithm with the best value of a given statistical parameter gets 1 and the algorithm with the worst value of a given statistical parameter gets 0. It means that the best overall AC algorithm over our in-situ dataset is the algorithm which gets the maximum number of 1. In Figure 9, we can observe that the accuracies of the AC algorithms depend on the wavelength, as mentioned earlier. In the blue bands (412 and 443 nm), NASA, NIRSWIR, Polymer are the most accurate. At 667 nm, most of the algorithms do not provide accurate retrievals of R_{rs} as the statistical parameters are not overall consistent. At 531 and 547 nm, NASA, NIRSWIR, OC-SMART, MUMM provide accurate retrievals. Overall, NASA, NIRSWIR and OC-SMART are the most accurate AC algorithms on our *in-situ* dataset covering low-to-moderately turbid waters.

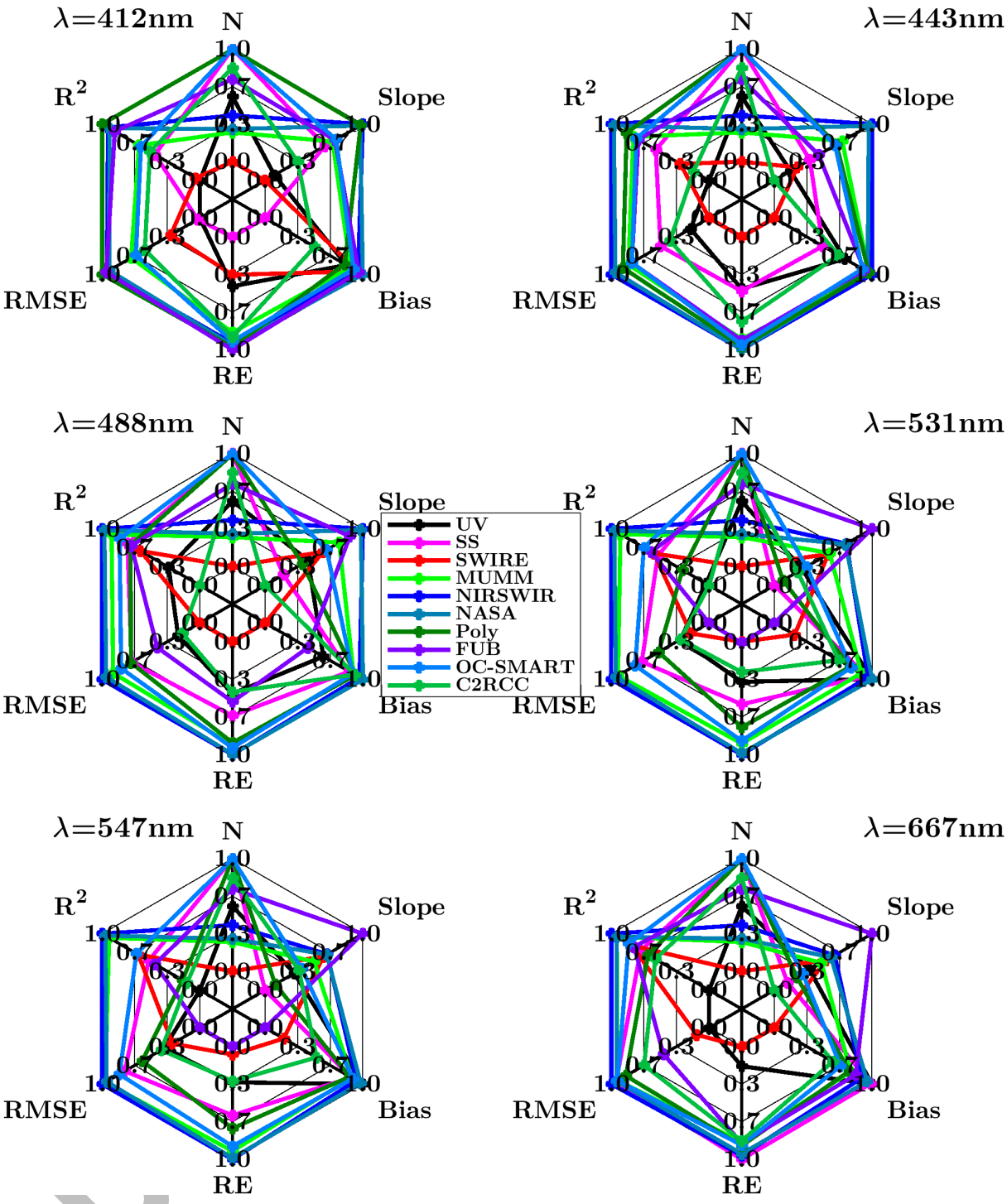

Figure 9: Spider-plot of the normalized statistical parameters as a function of wavelength

We now study the capability of the algorithms to retrieve the shape of the spectra. The previous analysis only considered the retrieval by wavelength. Here we use different statistical parameters (QAS, χ^2, SAM) to analyze the shape of the retrieved spectra. The results are presented in Table 4. We first compared the retrieved spectra to reference spectra through the QAS parameter (Wei et al., 2016). Most of the algorithms retrieve realistic spectra with values of QAS higher than 0.95 for MUMM, NIRSWIR, NASA, Polymer and OC-SMART. Two algorithms show less realistic spectra with QAS values of 0.78 (UV) and 0.82 (SWIRE). χ^2 and SAM compare the retrieved spectra to our in-situ spectra. NIRSWIR, NASA, Polymer, and OC-SMART present the lowest values of those parameters (10.70%,

11.01%, 9.59% and 10.66% for χ^2; 4.77°, 4.98°, 5.08° and 4.91° for SAM). Three algorithms (UV, SS13, C2RCC) show values of χ^2 greater than 40% (43.73%, 48.14% and 47.41%) and values of SAM greater than 9° (9.70°, 9.10° and 9.11°).

Table 4: Values of the statistical parameters calculated over the entire spectra. The bold value highlights the best value for a given statistical parameter.

ALGORITHMS	QAS	χ^2 (%)	SAM (°)	S_{tot}
UV	0.78	43.73	9.70	18.24
SS14	0.91	48.14	9.10	27.61
SWIRE	0.82	32.92	8.18	15.91
MUMM	0.95	15.30	5.59	34.59
NIRSWIR	0.96	10.70	**4.77**	37.55
NASA	0.96	11.01	4.98	**38.15**
Polymer	**0.97**	**9.59**	5.08	35.26
FUB	0.93	20.03	6.91	29.31
OC-SMART	0.97	10.66	4.91	36.34
C2RCC	0.94	47.41	9.11	26.45

We calculated the overall score (Müller et al., 2015) which considers the accuracies per wavelength and the shape of the spectra (Table 3). The maximum value of the score is 42. There is one group of AC algorithm with values higher than 35 (NASA (38.15), NIRSWIR (37.55), Polymer (35.26) and OC-SMART (36.34)) and one group with low values of S_{tot} less than 20 (UV (18.24) and SWIRE (15.91)).

Finally, the statistical parameters for each OWT were studied. Only classes 3-9 are included here as there are no matchups belonging to classes 1-2. The total Score is provided in Table 5. Only four ACs provide retrievals for OWT9: SS14, Polymer, OC-SMART and C2RCC. OWT9 represents the least turbid optical waters. Only one AC has values greater than 30 for all OWT (NIRSWIR). NASA and OC-SMART AC have values of S_{tot} greater than 30 for OWT 3-7 and values close to 30 for OWT 8 (29.87 and 28.49, respectively). SS14 shows similar values of S_{tot} for all OWT, which is not the case for MUMM, Polymer, FUB and C2RCC.

Table 5: S_{tot} values for all AC as a function of optical water types (OWT). The bold value highlights the best value for a given OWT.

	OWT1	OWT2	OWT3	OWT4	OWT5	OWT6	OWT7	OWT8	OWT9
UV	0	0	21.17	22.87	18.50	20.68	18.84	21.75	0
SS14	0	0	27.30	27.50	28.09	26.50	27.21	28.51	**32.60**
SWIRE	0	0	24.65	10.11	18.34	10.09	10.38	20.80	0
MUMM	0	0	28.76	33.47	34.42	34.83	29.42	24.61	0
NASA	0	0	32.81	**38.86**	**38.45**	**37.79**	**33.46**	29.87	0
NSWIR	0	0	33.73	36.88	37.87	36.20	33.35	**30.00**	0
Polymer	0	0	29.62	36.02	25.29	33.98	21.29	25.57	20.39
FUB	0	0	21.46	28.18	25.53	26.85	24.98	21.60	0
OC-SMART	0	0	**34.63**	37.01	31.76	35.94	30.44	28.49	19.24
C2RCC	0	0	29.27	24.16	22.47	26.90	25.13	27.47	31.72

2) Common match-ups analysis

In the previous section, we looked at the performance of the AC algorithms over their overall match-ups dataset. Here we directly compare the AC algorithms on the common match-ups analysis, i.e. on the dates and locations that are common to all algorithms. As SWIRE provides the least number of match-ups (N=242), the common match-ups dataset is reduced further to N=83 values. But this dataset provides a direct comparison of the statistical parameters between the ten AC algorithms.

Figure 10 provides the scatterplots per wavelength. As for the overall dataset, there is high scattering in the blue bands (412 and 443 nm) and the scattering decreases as 531 and 547 nm. UV, SS14 and SWIRE show very high values of retrieved R_{rs} compared to *in-situ* data at 412 and 443 nm. All algorithms seem to provide similar R_{rs} from 448 to 667 nm, except for FUB and C2RCC which provide high values for *in-situ* R_{rs}>0.2 sr^{-1} for few points at 531, 547 and 667 nm.

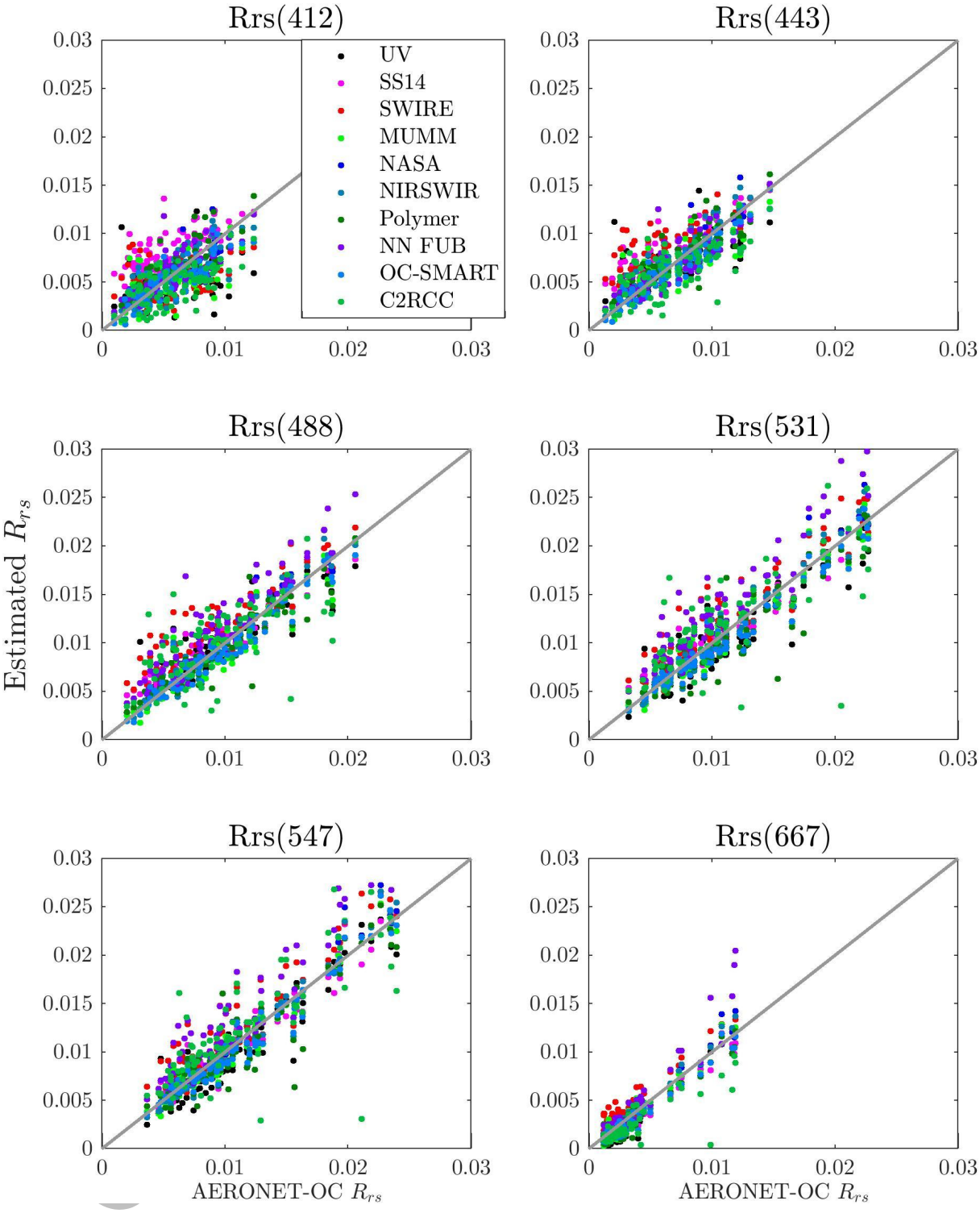

Figure 10: Scatterplots of the AC estimated R_{rs} vs *in-situ* R_{rs} from 412 (top left) to 667 nm (bottom right). The individual scatterplots are provided in Appendix II.

Table 6 provides all statistical parameters per wavelength (similar as Table 3). On the common dataset, no algorithm provides negative values of R_{rs} and all statistics are better which means that all algorithms provide more accurate retrievals of R_{rs} on the common match-ups dataset. Even if the statistical errors decrease on this common dataset, the relative accuracies of the AC algorithms are similar to those for the individual match-ups dataset. Five AC algorithms (NASA, NIRSWIR, MUMM, Polymer, OC-SMART) provide accurate retrievals at 488, 531 and 547 nm (Table 6 and Figure 10), with relative errors lower

than 15% and correlation coefficients higher than 0.86 at those three wavelengths. The other five algorithms (UV, SS, SWIRE, FUB and C2RCC) provide retrievals with relative errors higher than 24% for those wavelengths. At 412 nm, low accuracies are obtained for three algorithms (UV, SWIRE and SS14) with relative errors higher than 40% leading to low slopes (lower than 0.6) and low correlation coefficients (lower than 0.51). Five algorithms (NASA, NIRSWIR, Polymer, FUB and OC-SMART) provide accurate retrievals with low relative errors (lower than 23% at 412 nm and lower than 20% at 443 nm). FUB seems to provide accurate retrievals at 412 and 443 nm but less accurate retrievals between 488 and 547 nm, a behavior in contrast to the other AC algorithms which tend to have higher errors in the blue bands than in the green and red bands. NASA, NIRSWIR and OC-SMART are not very sensitive to the wavelengths providing accurate retrievals at all bands as the RMSE and relative errors vary slightly between bands (Figure 11).

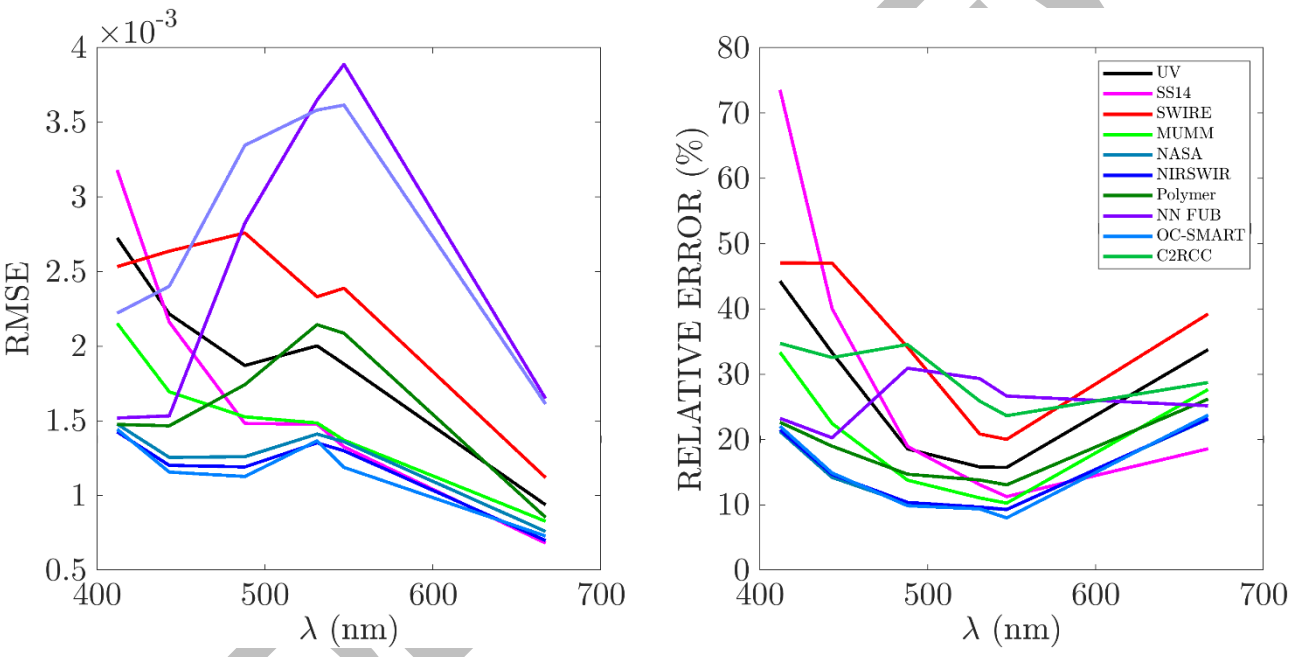

Figure 11: (a) Variation of the relative error as a function of wavelength, (b) Variation of the RMSE as a function of wavelength.

Figure 12 presents all statistical parameters as a spider plot (same as Figure 9). For λ=412, 443 and 488 nm, four algorithms (NASA, NIRSWIR, OC-SMART, FUB) show the best overall performances for the five statistical parameters considered. For λ=667 nm, SWIRE and C2RCC seem to be the least accurate while NIRSWIR, NASA, OC-SMART and FUB seem to be the most accurate (even if their slopes are not the best ones). For λ=531 and 547nm, SWIRE and C2RCC are the least accurate AC algorithms while MUMM NASA, NIRSWIR, OC-SMART are the AC algorithms with the best overall statistical parameters.

Table 6: Same as Table 3 but on the common match-ups dataset.

	RE(%)	*RMSE* (sr^{-1})	Slope (sr^{-1})	Intercept	Bias (sr^{-1})	β (%)	α (%)	R^2	*Nvm*
NASA STD AC Model									
R_{rs} (412)	22	0.00148	0.78	0.0011	-0.00017	-11	41	0.68	83
R_{rs} (443)	14	0.00126	0.94	0.0005	0.00012	-5	26	0.84	83
R_{rs} (488)	10	0.00126	1.00	-0.00008	-0.00011	-6	20	0.92	83
R_{rs} (531)	10	0.00141	1.05	-0.0008	-0.00030	-11	22	0.93	83
R_{rs} (547)	9	0.00136	1.09	-0.0012	-0.00024	-10	19	0.95	83
R_{rs} (667)	23	0.00076	1.15	-0.0007	-0.00028	-54	59	0.96	83
NIRSWIR AC Model									
R_{rs} (412)	22	0.00143	0.80	0.0010	-0.00011	-1	43	0.69	83
R_{rs} (443)	15	0.00120	0.95	0.0005	0.00016	8	26	0.86	83
R_{rs} (488)	11	0.00120	1.00	-0.0001	-0.00009	-6	22	0.93	83
R_{rs} (531)	10	0.00135	1.05	-0.0008	-0.00029	-11	23	0.94	83
R_{rs} (547)	9	0.00130	1.09	-0.0012	-0.00022	-10	20	0.95	83
R_{rs} (667)	23	0.00070	1.14	-0.0007	-0.00028	-53	57	0.96	83
MUMM AC Model									
R_{rs} (412)	33	0.00215	0.49	0.00233	-0.00056	-18	85	0.36	83
R_{rs} (443)	22	0.00169	0.73	0.00170	-0.00018	-8	49	0.70	83
R_{rs} (488)	14	0.00153	0.87	0.00086	-0.00034	-9	27	0.88	83
R_{rs} (531)	11	0.00149	0.96	-0.00004	-0.00048	-13	23	0.92	83
R_{rs} (547)	10	0.00137	1.01	-0.00051	-0.00040	-12	21	0.94	83
R_{rs} (667)	28	0.00083	1.04	-0.00052	-0.00040	-44	82	0.93	83
SS14 AC Model									
R_{rs} (412)	74	0.00318	0.56	0.00514	0.00264	136	136	0.51	83
R_{rs} (443)	40	0.00216	0.71	0.00361	0.00159	45	45	0.78	83
R_{rs} (488)	19	0.00148	0.80	0.00238	0.00047	5	24	0.90	83
R_{rs} (531)	13	0.00148	0.87	0.00159	0.00003	-2	22	0.91	83
R_{rs} (547)	11	0.00132	0.92	0.00089	0.000006	-1	23	0.93	83
R_{rs} (667)	19	0.00068	0.91	-0.00005	-0.00032	-31	47	0.95	83
SWIRE AC model									
R_{rs} (412)	47	0.00253	0.27	0.00359	-0.000542	-37	112	0.14	83
R_{rs} (443)	47	0.00264	0.61	0.00439	0.00171	54	55	0.57	83
R_{rs} (488)	34	0.00276	0.82	0.00368	0.00198	47	47	0.80	83
R_{rs} (531)	21	0.00233	0.93	0.00202	0.00124	23	32	0.85	83
R_{rs} (547)	20	0.00239	1.00	0.00131	0.00136	25	34	0.87	83
R_{rs} (667)	39	0.00112	1.05	0.00057	0.00072	65	69	0.91	83

	RE (%)	*RMSE (sr^{-1})*	Slope *(sr^{-1})*	Intercept	Bias *(sr^{-1})*	*β (%)*	*ε (%)*	*R^2*	*Nvm*
		UV AC Model							
R_{rs} (412)	44	0.00273	0.25	0.0005	-0.0008	-43	137	0.11	83
R_{rs} (443)	33	0.00222	052	0.0018	0.0001	1	57	0.48	83
R_{rs} (488)	19	0.00187	0.78	0.0014	0.0002	2	27	0.81	83
R_{rs} (531)	16	0.00200	0.89	-0.0003	-0.0009	-28	39	0.87	83
R_{rs} (547)	16	0.00188	0.97	-0.0010	-0.0007	-22	34	0.88	83
R_{rs} (667)	34	0.00094	0.99	-0.0007	-0.0006	-120	137	0.93	83
		Polymer AC Model							
R_{rs} (412)	23	0.00148	0.84	0.0013	0.00038	21	54	0.70	83
R_{rs} (443)	19	0.00147	0.80	0.0015	0.00010	8	35	0.77	83
R_{rs} (488)	15	0.00174	0.82	0.0014	-0.00033	-7	30	0.84	83
R_{rs} (531)	14	0.00214	0.86	0.0007	-0.00084	-17	32	0.84	83
R_{rs} (547)	13	0.00209	0.93	0.0003	-0.00057	-8	25	0.84	83
R_{rs} (667)	26	0.00085	0.95	-0.0004	-0.00054	-68	77	0.93	83
		FUB AC model							
R_{rs} (412)	23	0.00152	0.74	0.00139	-0.00007	-5	50	0.65	83
R_{rs} (443)	20	0.00153	0.79	0.00139	-0.00004	-1	43	0.75	83
R_{rs} (488)	31	0.00282	1.00	0.00217	0.00215	60	60	0.84	83
R_{rs} (531)	29	0.00365	1.17	0.00098	0.00286	74	74	0.88	83
R_{rs} (547)	27	0.00389	1.28	-0.00037	0.00273	63	63	0.87	83
R_{rs} (667)	25	0.00165	1.45	-0.00096	0.00041	1	73	0.91	83
		OC-SMART AC model							
R_{rs} (412)	22	0.00144	0.70	0.00120	-0.0005	-21	52	0.71	83
R_{rs} (443)	15	0.00116	0.83	0.00069	-0.0005	-17	33	0.88	83
R_{rs} (488)	10	0.00112	0.91	0.00044	-0.0004	-11	19	0.94	83
R_{rs} (531)	9	0.00137	0.93	0.00008	-0.0007	-14	19	0.94	83
R_{rs} (547)	8	0.00119	1.01	-0.00044	-0.0003	-8	15	0.95	83
R_{rs} (667)	24	0.00073	0.96	-0.00042	-0.0005	-72	72	0.96	83
		C2RCC model							
R_{rs} (412)	35	0.00222	0.50	0.00017	-0.0011	-87	139	0.43	83
R_{rs} (443)	33	0.00240	0.54	0.00251	-0.0007	-28	88	0.45	83
R_{rs} (488)	35	0.00335	0.59	0.00450	0.0007	22	66	0.45	83
R_{rs} (531)	26	0.00358	0.70	0.00417	0.0009	30	46	0.55	83
R_{rs} (547)	24	0.00362	0.77	0.00346	0.0009	29	49	0.57	83
R_{rs} (667)	29	0.00161	0.62	0.00029	-0.0009	-98	103	0.73	83

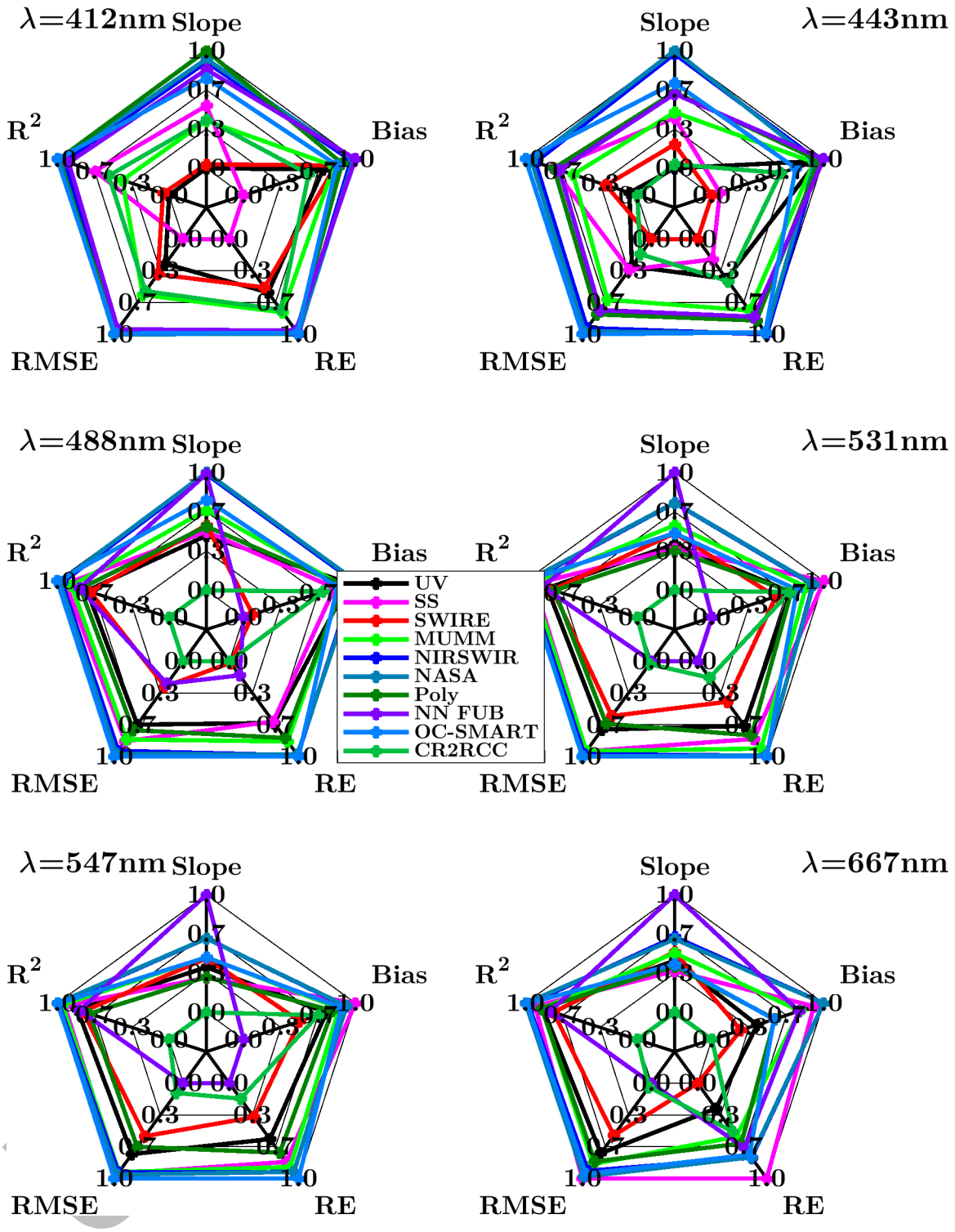

Figure 12: Spider-plot of the normalized statistical parameters as a function of wavelength.

Table 7 provides the statistical parameters on the shape of the retrieved spectra compared to the *in-situ* spectra (same as Table 4). The algorithms can be partitioned into three groups depending of the values of S_{tot}: 1) $S_{tot} \leq 20$ (SWIRE, C2RCC), 2) $20 \leq S_{tot} \leq 35$ (UV, SS14, MUMM, FUB, Polymer) and 3) $S_{tot} > 37$ (NASA, NIRSWIR and OC-SMART). In terms of shape, the vast majority of the algorithms provide accurate spectra compared to reference spectra with values of QAS >0.90, except for UV (QAS=0.89) and SWIRE (QAS=0.81). For χ^2 and SAM, the results are similar as for the individual match-ups dataset. For χ^2, the algorithms can be groups into three parts: 1) $\chi^2 > 20\%$ (UV, SS14 and C2RCC), 2) $10 \leq \chi^2 \leq 20\%$

(SWIRE, MUMM, Polymer and FUB) and 3) 10%>χ^2 (NASA, NIRSWIR and OC-SMART). For SAM, the algorithms can also be grouped into three categories: 1) SAM>8° (SS14 and C2RCC), 2) 5°≤SAM≤8° (UV, SWIRE, MUMM and FUB) and 3) 5°>SAM (NASA, NIRSWIR, Polymer and OC-SMART).

Table 7: Values of the statistical parameters calculated over the entire spectral range. The bold value highlights the best value for a given statistical parameter.

ALGORITHMS	QAS	χ^2 (%)	SAM (°)	S_{tot}
UV	0.89	24.30	7.70	26.83
SS14	0.92	21.94	8.96	29.24
SWIRE	0.81	16.76	7.03	20.95
MUMM	0.96	13.83	5.32	34.28
NIRSWIR	0.96	7.01	3.98	**39.24**
NASA	0.96	**6.91**	**3.95**	38.76
Polymer	**0.97**	11.10	4.97	34.34
FUB	0.95	14.90	6.32	25.06
OC-SMART	0.97	7.56	4.09	38.69
CR2CC	0.95	33.20	8.33	15.58

Finally, as for the individual matchups dataset, the statistical parameters for each OWT were studied. Only classes 3-8 are included here as SWIRE does not provide any matchups for OWT 9. The total Score is provided in Table 8. The majority of matchups is included in OWT 6-7 (table 2), the less turbid waters. There are only a few matchups (2) for OWT 3. In term of total Scores (Table 7), the results are slightly different than for the individual matchups dataset. S_{tot} decreases for all AC for OWT 3. This might be explained by the very low number of matchups for this OWT. For OWT 4-7, NIRSWIR and NASA show values greater than 36. S_{tot} values tend to decrease from OWT 4 to OWT 8. This can be explained by the fact that all AC in this study were designed to deal with moderately to very turbid waters while the turbidity of our OWT decreases from OWT 3 to OWT 8.

Table 8: S_{tot} values for all AC as a function of OWT. The bold value highlights the best value for a given parameter.

	OWT1	OWT2	OWT3	OWT4	OWT5	OWT6	OWT7	OWT8	OWT9
UV	0	0	20.71	31.72	23.68	19.41	22.62	18.65	0
SS14	0	0	16.72	26.75	26.03	25.59	31.17	**37.41**	0
SWIRE	0	0	18.14	21.90	18.05	10.39	25.11	35.39	0
MUMM	0	0	18.39	33.32	33.72	34.69	29.16	22.80	0
NASA	0	0	14.51	39.80	**40.37**	**37.08**	**36.23**	28.21	0
NSWIR	0	0	21.69	39.09	39.58	**37.08**	**36.23**	28.21	0
Polymer	0	0	24.21	37.23	24.78	31.07	29.01	12.87	0
FUB	0	0	12.37	26.79	24.80	23.93	24.41	24.05	0
OC-SMART	0	0	**26.02**	**40.56**	35.42	37.17	28.98	26.76	0
C2RCC	0	0	18.37	15.29	17.40	29.88	11.13	20.19	0

3) Sensitivity studies

In this section, we study the behavior of each algorithm to the content in aerosols (the aerosol optical thickness at 869 nm, τ(869)) and the turbidity of the coastal waters through the total suspended matter

(SPM). τ(869) is directly measured by the AERONET-OC stations and SPM is estimated from *in-situ* R_{rs} using the algorithm of Han et al. (2016). This algorithm uses a switching threshold to better estimate the lower and higher values of SPM using $R_{rs}(667)$.

We also present the ratio of R_{rs} that are commonly used for the estimation of the chlorophyll-a concentration (O'Reilly et al., 1998, 2019): $R_{rs}(443)/R_{rs}(547)$, $R_{rs}(488)/R_{rs}(547)$ and $R_{rs}(531)/R_{rs}(547)$.

Note that in these sensitivities' studies, we used all the match-ups dataset without fixing any parameter. Ideally, the sensitivities study should be done by fixing all parameters except one. In our case, it is not easy to do as the values of the aerosols and bio-optical parameters are not directly available.

a) Individual spectra match-ups

Sensitivity to τ(869)

Figure 13 shows the variation of the relative error on the retrieval of $R_{rs}(\lambda)$ as a function of τ(869) for all ten algorithms. We can observe that there are two groups of algorithms. A first group of algorithms (NASA, NIRSWIR, MUMM, Polymer, OC-SMART, UV) for which the relative errors is slightly dependent on the values of τ(869) and a second group (SWIRE, SS14, FUB) for which the accuracy of the retrievals is highly dependent on the values of τ(869). It is particularly true for bands between 412 and 488 nm.

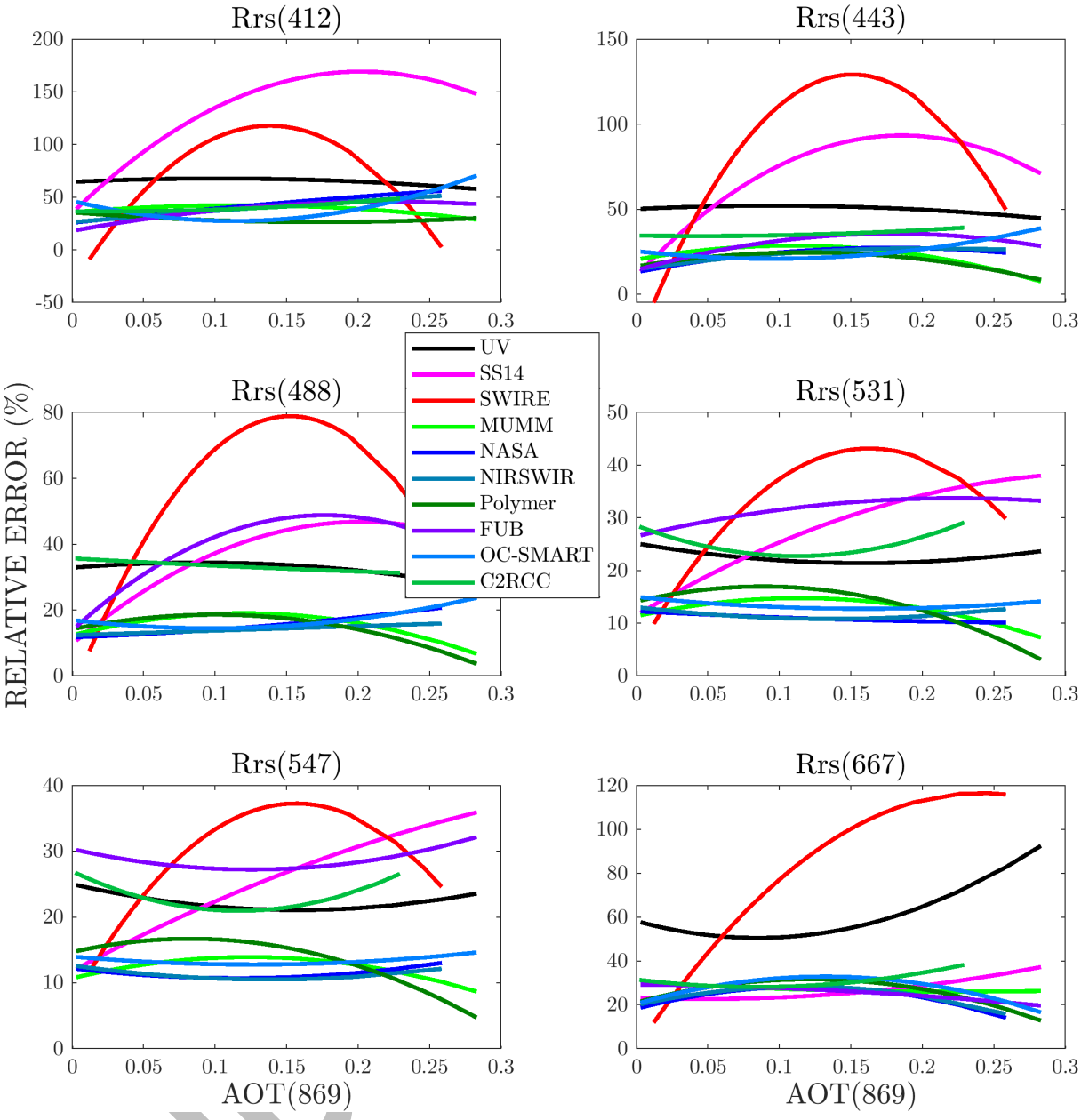

Figure 13: Variation of the relative error as a function of the aerosol optical thickness τ(869) for each wavelength.

Sensitivity to SPM

Figure 14 shows the variation of the relative errors as a function of SPM. We can observe that for all algorithms the shape of the relative errors has a smiley form, which means that they provide better retrievals for a specific range of SPM values. However, as for τ(869), we can observe the same two groups of AC algorithms depending on their sensitivities to SPM values.

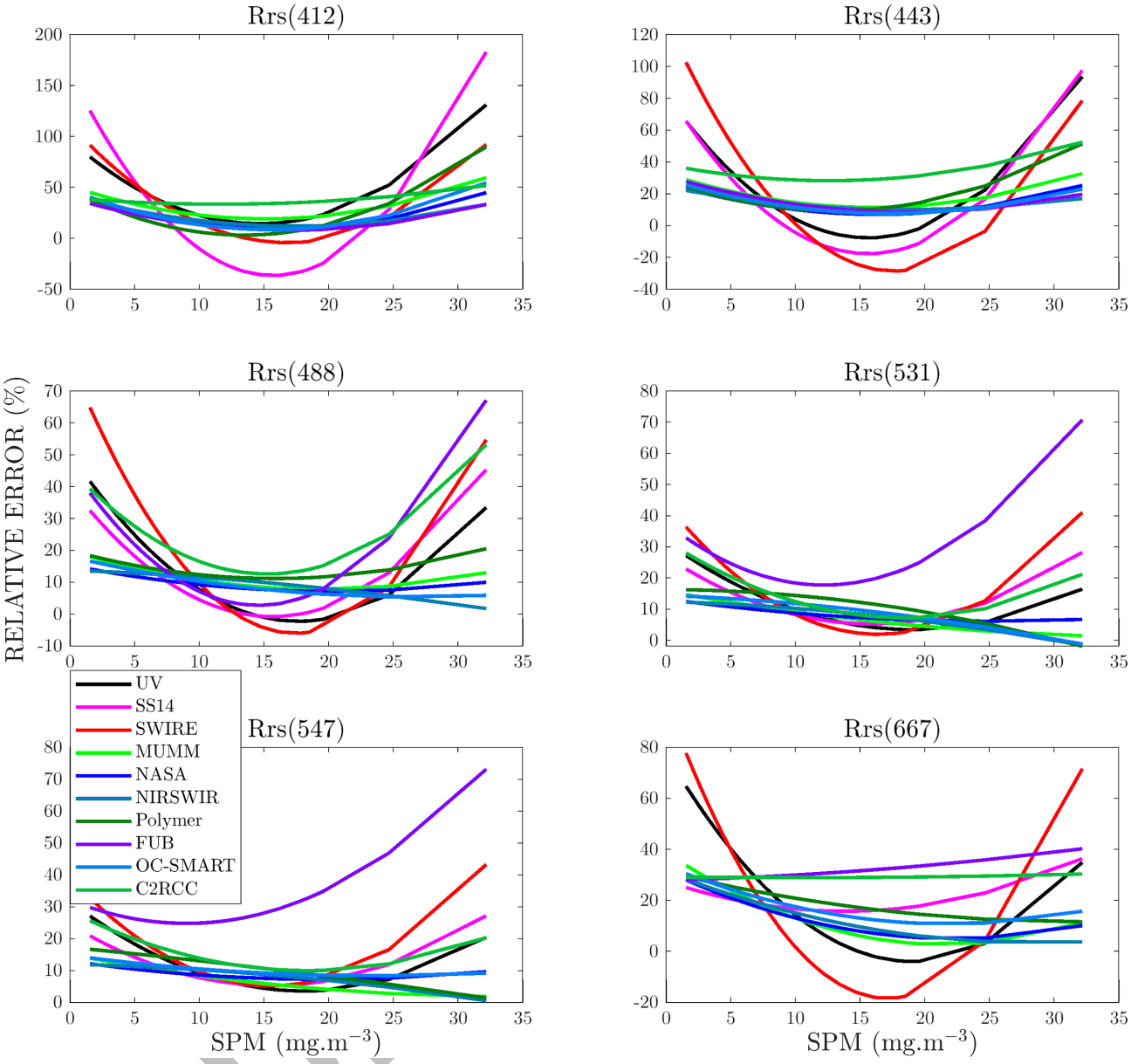

Figure 14: Variation of the relative error as a function of the suspended particulate matter (SPM) for each wavelength.

Estimation of R_{rs} ratios

Figure 15 shows the ratios of $R_{rs}(\lambda)$ commonly used in chlorophyll-a retrieval algorithms estimated by the ten algorithms vs the *in-situ* ratios. Even if the individual retrieval of $R_{rs}(\lambda)$ shows high errors, the $R_{rs}(\lambda)$ ratios can be of high quality. It means it is necessary to investigate the potential impact of the retrieval errors on the estimation of chlorophyll-a concentration. As expected, high scattering around the 1:1 line can be observed for $R_{rs}(443)/R_{rs}(547)$, especially for UV, SS14 and SWIRE. This is related to the large errors observed at 443 nm for these algorithms. In contrast, NASA, NIRSWIR and OC-SMART show less scattering for this ratio. The scattering around the 1:1 line decreases as λ increases. For $R_{rs}(531)/R_{rs}(547)$, most of the AC algorithms provide estimates close to the 1:1 line, except for values higher than 1.3 and less than 0.75. We can also observe that all algorithms tend to overestimate the low values of $R_{rs}(531)/R_{rs}(547)$. This is in accordance with the statistical parameters (Table 9) with a decrease of the slopes between $R_{rs}(488)/R_{rs}(547)$ and $R_{rs}(531)/R_{rs}(547)$ for all algorithms.

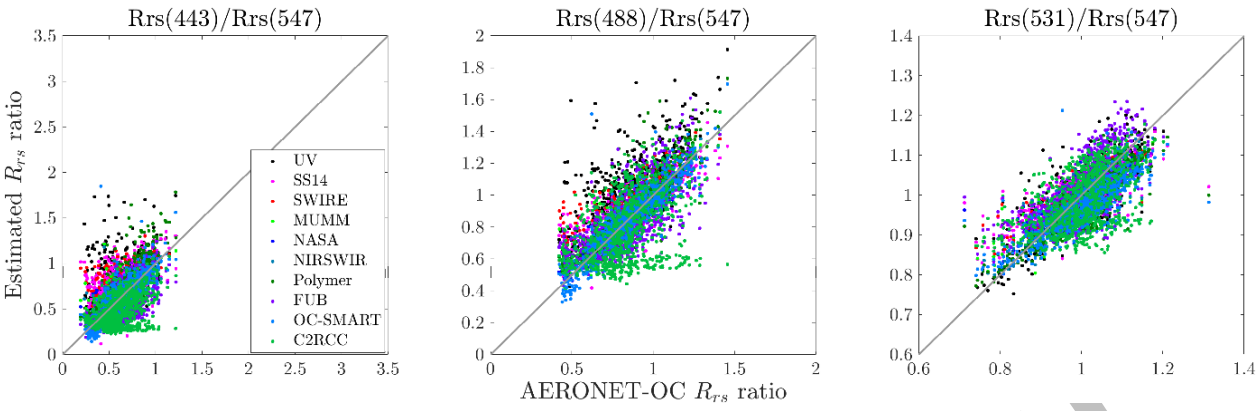

Figure 15: Scatterplot of the retrieved vs in-situ ratios of R_{rs} over the individual match-ups dataset: left panel: $R_{rs}(443)/R_{rs}(547)$; middle panel: $R_{rs}(488)/R_{rs}(547)$; right panel: $R_{rs}(531)/R_{rs}(547)$.

It translates to the RE and RMSE values, both parameters decreasing from $R_{rs}(443)/R_{rs}(547)$ to $R_{rs}(531)/R_{rs}(547)$. RE varies between 14% (NIRSWIR and OC-SMART) and 38% (UV) for $R_{rs}(443)/R_{rs}(547)$ and between 3% (NASA, NIRSWIR, MUMM and SWIRE) and 6% (C2RCC) for $R_{rs}(531)/R_{rs}(547)$.

Table 9: Same as Table 2 but for ratios $R_{rs}(\lambda)/R_{rs}(547)$ with λ =443 or 488 or 531 nm on the individual match-ups dataset.

	RE(%)	*RMSE*	Slope	Intercept	Bias	R^2
NASA STD AC Model						
$R_{rs}(443)/R_{rs}(547)$	15	0.109	0.79	0.147	0.0225	0.61
$R_{rs}(488)/R_{rs}(547)$	7	0.069	0.86	0.120	0.0063	0.86
$R_{rs}(531)/R_{rs}(547)$	3	0.039	0.71	0.290	-0.0022	0.74
NIRSWIR AC Model						
$R_{rs}(443)/R_{rs}(547)$	14	0.108	0.78	0.161	0.0274	0.60
$R_{rs}(488)/R_{rs}(547)$	6	0.068	0.86	0.127	0.0075	0.85
$R_{rs}(531))/R_{rs}(547)$	3	0.037	0.71	0.287	-0.0031	0.72
MUMM AC Model						
$R_{rs}(443)/R_{rs}(547)$	17	0.129	0.73	0.183	0.0159	0.48
$R_{rs}(488)/R_{rs}(547)$	7	0.076	0.83	0.145	0.0023	0.81
$R_{rs}(531)/R_{rs}(547)$	3	0.041	0.65	0.345	-0.0058	0.70
SS14 AC Model						
$R_{rs}(443)/R_{rs}(547)$	33	0.215	0.61	0.379	0.1408	0.34
$R_{rs}(488)/R_{rs}(547)$	11	0.108	0.66	0.321	0.0352	0.71
$R_{rs}(531)/R_{rs}(547)$	4	0.047	0.55	0.454	0.0026	0.65
SWIRE AC model						
$R_{rs}(443)/R_{rs}(547)$	37	0.234	0.48	0.485	0.1574	0.25
$R_{rs}(488)/R_{rs}(547)$	19	0.168	0.66	0.416	0.1254	0.66
$R_{rs}(531)/R_{rs}(547)$	3	0.043	0.63	0.380	0.0108	0.72
UV AC Model						
$R_{rs}(443)/R_{rs}(547)$	38	0.279	0.54	0.41	0.131	0.14
$R_{rs}(488)/R_{rs}(547)$	24	0.233	0.84	0.29	0.163	0.49
$R_{rs}(531)/R_{rs}(547)$	4	0.051	0.78	0.21	-0.003	0.63
Polymer AC Model						
$R_{rs}(443)/R_{rs}(547)$	17	0.141	1.10	0.002	0.0637	0.70
$R_{rs}(488)/R_{rs}(547)$	9	0.096	0.96	0.064	0.0271	0.80
$R_{rs}(531)/R_{rs}(547)$	4	0.048	0.75	0.223	-0.0255	0.72
FUB AC model						
$R_{rs}(443)/R_{rs}(547)$	24	0.178	0.73	0.059	-0.108	0.48
$R_{rs}(488)/R_{rs}(547)$	15	0.154	0.78	0.178	-0.0044	0.50
$R_{rs}(531)/R_{rs}(547)$	5	0.062	0.74	0.276	0.0139	0.50
OC-SMART AC model						
$R_{rs}(443)/R_{rs}(547)$	14	0.112	0.91	0.054	-0.0036	0.67
$R_{rs}(488)/R_{rs}(547)$	7	0.077	0.95	0.041	-0.0016	0.85
$R_{rs}(531)/R_{rs}(547)$	4	0.052	0.65	0.323	-0.0315	0.71
C2RCC AC model						
$R_{rs}(443)/R_{rs}(547)$	28	0.222	0.46	0.196	-0.1334	0.22
$R_{rs}(488)/R_{rs}(547)$	20	0.215	0.55	0.334	-0.0440	0.23
$R_{rs}(531)/R_{rs}(547)$	6	0.075	0.48	0.503	-0.0131	0.26

Estimation of chlorophyll-a concentration CHL

Finally, we studied the accuracy in retrieving the chlorophyll-a concentration using the OC3 algorithm (O'Reilly et al., 2019). Figure 16 shows a comparison between the AC derived chl-a for each AC versus the AERONET-OC derived chl-a. It is intended to go further than just estimating the accuracies of the

R_{rs} ratios as OC3 uses a maximum function to choose the ratio. So the retrievals of the chl-a can be estimated using different band ratios. As shown in Figure 16, most of the AC is able to provide accurate retrievals of chl-a for values between 1 and 10 mg.m^{-3}, as most of the retrievals are close to the 1:1 line. However, for values greater than 10 mg.m^{-3}, there is an underestimation for all AC.

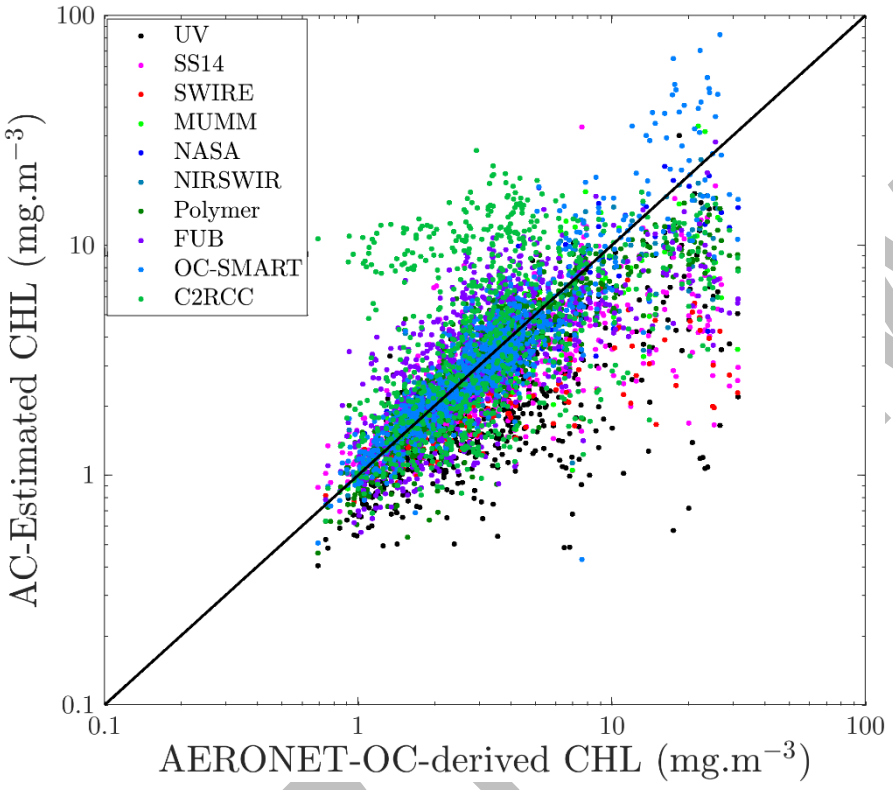

Figure 16: Scatterplot of the retrieved chlorophyll-a concentration chl-a vs in-situ derived chl-a.

Table 10 provides the statistical parameters on the estimation of the chl-a. There is one group of AC with lower values of RMSE and relative errors and higher values of R^2: MUMM, NASA, NIRSWIR, OC-SMART and Polymer with values between 19 and 23% for the relative errors and between 2.41 and 4.84 mg.m^{-3} for RMSE. UV, FUB and C2RCC are the AC providing chl-a with the highest relative errors. This is in accordance with the highest RMSE and relative errors obtained for the band ratios.

Table 10: Statistical parameters of the retrieval of chl-a. The bold value highlights the best value for a given parameter.

	UV	SS	SWIRE	MUMM	NASA	NIRSWIR	Polymer	FUB	OC-SMART	C2RCC
RMSE (mg.m^{-3})	4.74	4.16	5.41	3.01	2.93	**2.41**	3.01	4.00	4.84	5.64
Relative Error (%)	41	27	33	21	20	**19**	23	51	23	111
Bias (mg.m^{-3})	-2.20	-1.31	-2.40	-0.38	-0.54	**-0.49**	-0.80	-0.31	0.58	1.05
R^2	0.33	0.28	0.27	0.48	0.67	**0.72**	0.71	0.31	0.63	0.09

b) Common spectra match-ups

The same type of sensitivity studies was done for the common match-ups dataset.

Sensitivity to τ(869)

Figure 17 shows the variation of the relative errors as a function of the values of τ(869). The values of τ(869) are limited to 0.15 for the common match-ups dataset (compared to values up to 0.28 for the individual match-ups dataset). The results and trends are similar to those for the individual match-ups datasets. Three main groups of algorithms are observed. The first group (UV, SS14, SWIRE) shows a high sensitivity to the values of τ(869) with increased relative errors with increased values of τ(869) for all wavelengths. The second group (NIRSWIR, NASA, MUMM, Polymer, OC-SMART) shows low sensitivity to the values of τ(869). The third group (FUB) shows a high sensitivity to the wavelength, especially at 531 and 547 nm. This corresponds to the bands where this algorithm is less accurate. At the other bands, this algorithm is slightly sensitive to the value of τ(869).

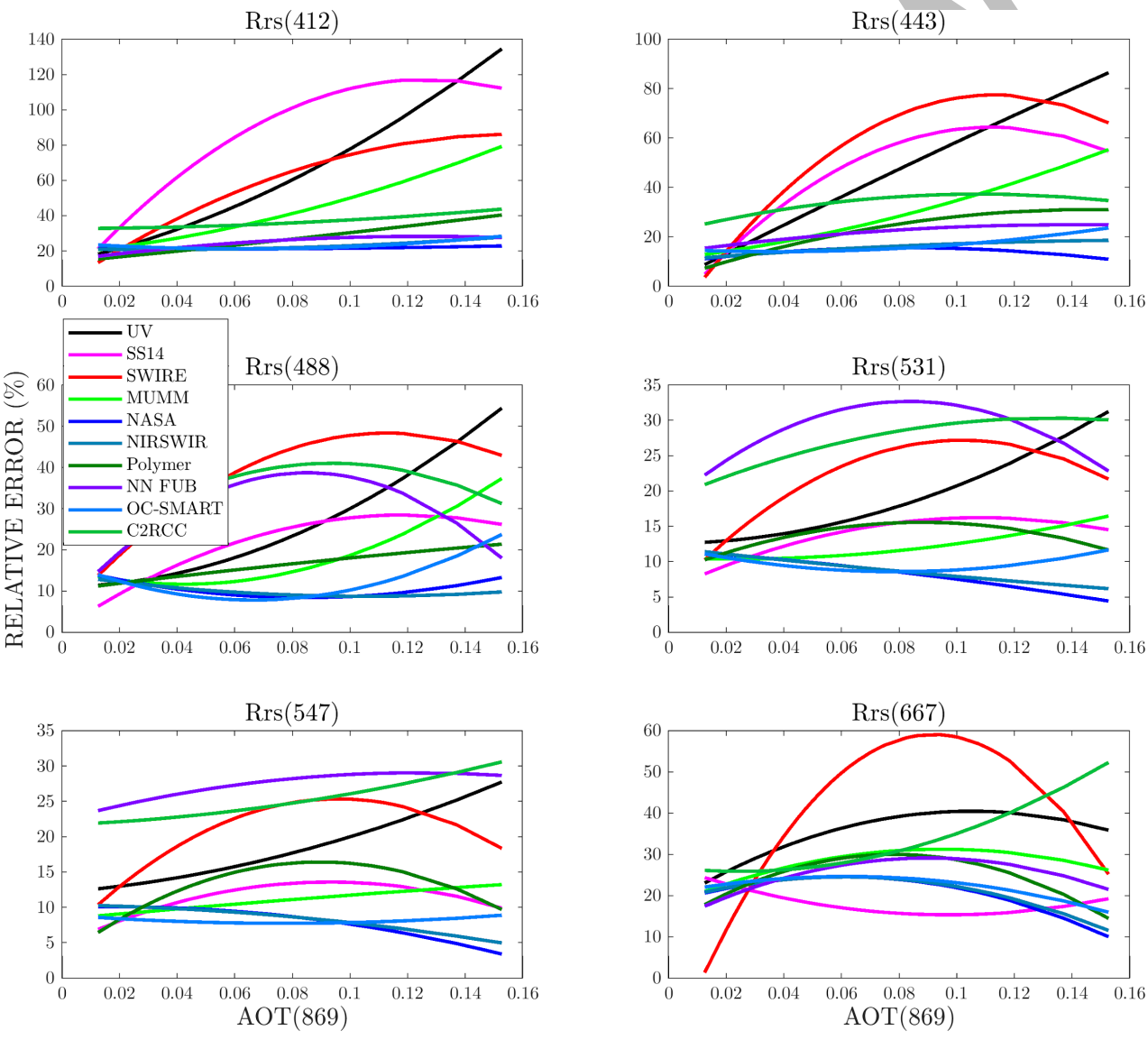

Figure 17: Variation of the relative error as a function of the aerosol optical thickness τ(869) for each wavelength.

Sensitivity to SPM

Figure 18 shows the variation of the relative error as a function of SPM. On the common match-ups dataset, the values of SPM are limited to 17 $mg.m^{-3}$. As for the individual match-ups dataset, two groups of algorithms are observed. The first group (UV, SS14, SWIRE) is very sensitive to SPM values for all wavelengths while the second group (NIRSWIR, NASA, MUMM, Polymer, OC-SMART) is slightly

sensitive to SPM values for all wavelengths (except at 667 nm). As for τ(869), FUB is very sensitive to SPM values at 531 and 547 nm with relative errors varying from 27% to 52% at 531 nm and between 20% and 46% at 547 nm.

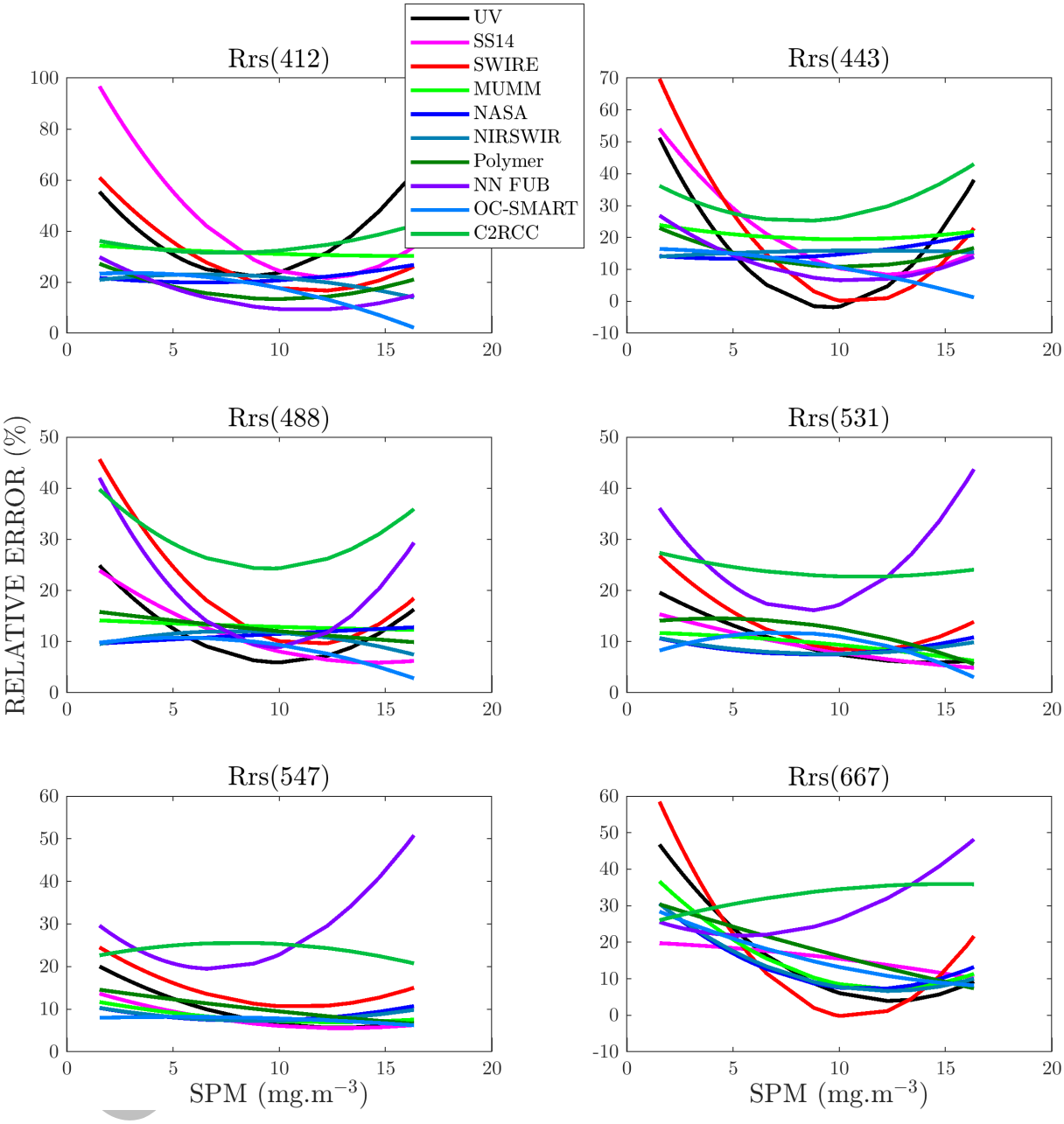

Figure 18: Variation of the relative error as a function of the suspended particulate matter (SPM) for each wavelength.

Estimation of R_{rs} ratios

Figure 19 shows scatterplots of the estimated ratios of $R_{rs}(\lambda)/R_{rs}(547)$ vs *in-situ* $R_{rs}(\lambda)/R_{rs}(547)$ with λ=443, 488 or 531 nm. As for the individual match-ups dataset, the ratio of $R_{rs}(\lambda)/R_{rs}(547)$ is better retrieved at 537 nm than at 443 nm. This is, again, linked to the estimates of the retrievals at those bands. High scattering and over-estimation are observed for $R_{rs}(443)/R_{rs}(547)$, especially for UV, SS14, SWIRE. FUB and C2RCC seem to under-estimate this ratio. For $R_{rs}(488)/R_{rs}(547)$, most of the algorithms seem to over-estimate this ratio. This is especially true for UV, SS14, SWIRE. For $R_{rs}(531)/R_{rs}(547)$, FUB

and C2RCC over-estimate this ratio while all other algorithms seem to provide estimates close to the 1:1 line. This can be observed with the statistical parameters (Table 11).

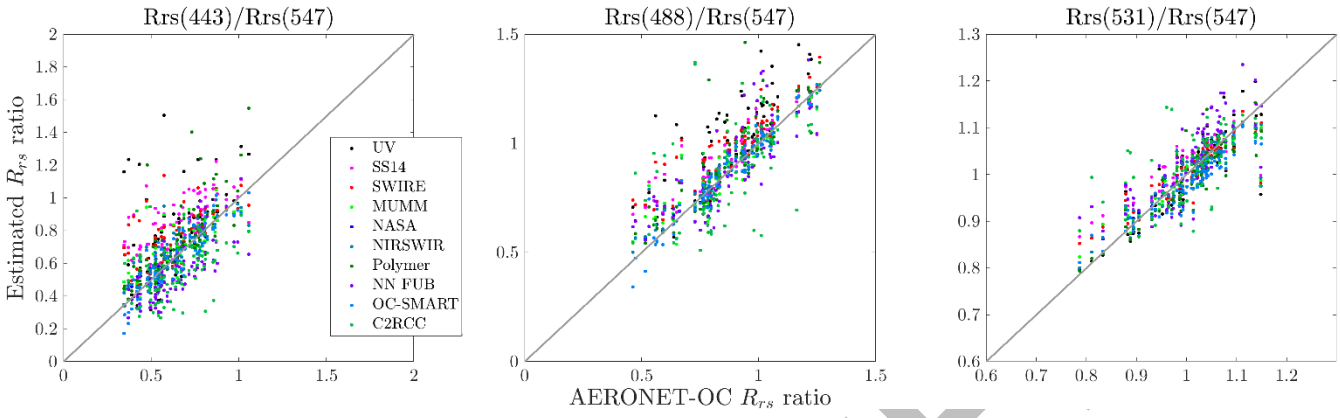

Figure 19: Scatterplot of the retrieved vs *in-situ* ratios of R_{rs} over the common match-ups dataset: left panel: $R_{rs}(443)/R_{rs}(547)$; middle panel: $R_{rs}(488)/R_{rs}(547)$; right panel: $R_{rs}(531)/R_{rs}(547)$.

Table 11: Same as Table 8 but for ratios $R_{rs}(\lambda)/R_{rs}(547)$ with λ =443 or 488 or 531 nm on the common match-ups dataset.

	RE(%)	*RMSE*	Slope	Intercept	Bias	R^2
NASA STD AC Model						
$R_{rs}(443)/R_{rs}(547)$	12	0.093	0.76	0.194	0.0391	0.74
$R_{rs}(488)/R_{rs}(547)$	5	0.056	0.97	0.129	0.021	0.92
$R_{rs}(531)/R_{rs}(547)$	2	0.030	0.77	0.221	-0.0009	0.83
NIRSWIR AC Model						
$R_{rs}(443)/R_{rs}(547)$	12	0.094	0.74	0.207	0.0391	0.74
$R_{rs}(488)/R_{rs}(547)$	5	0.057	0.87	0.138	0.0192	0.92
$R_{rs}(531))/R_{rs}(547)$	2	0.030	0.77	0.227	-0.0009	0.83
MUMM AC Model						
$R_{rs}(443)/R_{rs}(547)$	17	0.124	0.68	0.230	0.027	0.51
$R_{rs}(488)/R_{rs}(547)$	7	0.071	0.84	0.150	0.015	0.86
$R_{rs}(531)/R_{rs}(547)$	2	0.032	0.75	0.247	-0.001	0.81
SS14 AC Model						
$R_{rs}(443)/R_{rs}(547)$	34	0.225	0.64	0.410	0.181	0.44
$R_{rs}(488)/R_{rs}(547)$	11	0.107	0.70	0.323	0.064	0.79
$R_{rs}(531)/R_{rs}(547)$	3	0.038	0.64	0.371	0.010	0.76
SWIRE AC model						
$R_{rs}(443)/R_{rs}(547)$	24	0.176	0.60	0.363	0.104	0.38
$R_{rs}(488)/R_{rs}(547)$	14	0.132	0.79	0.282	0.096	0.76
$R_{rs}(531)/R_{rs}(547)$	3	0.035	0.73	0.268	-0.001	0.77
UV AC Model						
$R_{rs}(443)/R_{rs}(547)$	30	0.252	0.74	0.296	0.127	0.25
$R_{rs}(488)/R_{rs}(547)$	18	0.189	1.04	0.098	0.136	0.68
$R_{rs}(531)/R_{rs}(547)$	3	0.041	0.95	0.053	-0.001	0.74
Polymer AC Model						
$R_{rs}(443)/R_{rs}(547)$	18	0.172	1.13	-0.005	0.083	0.61
$R_{rs}(488)/R_{rs}(547)$	10	0.119	0.99	0.051	0.045	0.73
$R_{rs}(531)/R_{rs}(547)$	3	0.042	0.85	0.137	-0.018	0.75
FUB AC model						
$R_{rs}(443)/R_{rs}(547)$	20	0.156	0.85	-0.008	-0.104	0.60
$R_{rs}(488)/R_{rs}(547)$	12	0.129	0.91	0.097	0.020	0.64
$R_{rs}(531)/R_{rs}(547)$	5	0.056	0.90	0.128	0.024	0.62
OC-SMART AC model						
$R_{rs}(443)/R_{rs}(547)$	11	0.081	0.99	-0.001	-0.007	0.80
$R_{rs}(488)/R_{rs}(547)$	5	0.054	1.00	-0.0002	0.0008	0.92
$R_{rs}(531)/R_{rs}(547)$	3	0.042	0.73	0.247	-0.0268	0.82
C2RCC model						
$R_{rs}(443)/R_{rs}(547)$	26	0.195	0.46	0.250	-0.095	0.2
$R_{rs}(488)/R_{rs}(547)$	17	0.193	0.60	0.366	0.016	0.28
$R_{rs}(531)/R_{rs}(547)$	5	0.066	0.55	0.465	0.008	0.33

Estimation of chlorophyll-a concentration CHL

As for the individual matchups dataset, the retrieval of chl-a was investigated for the common dataset.

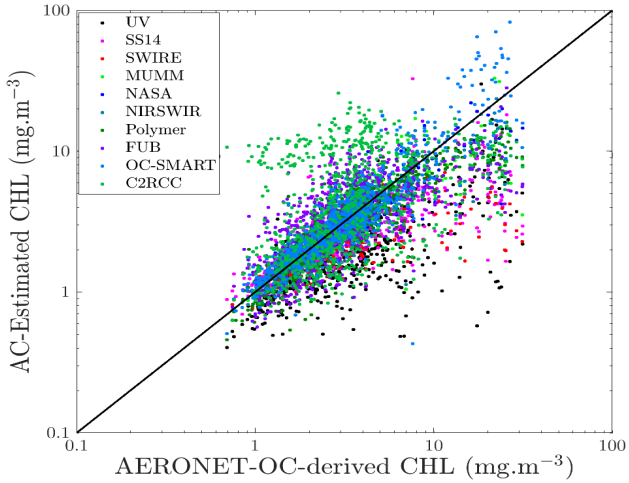

Figure 20: Scatterplot of the retrieved chlorophyll-a concentration chl-a vs *in-situ* derived chl-a

Figure 20 shows the scatterplots of the AC derived chl-a versus the AERONET-OC derived chl-a and Table 12 shows the statistical parameters. The results are very similar to those for the individual matchups dataset. NASA and NIRSWIR show the lowest values of RMSE and relative errors and the highest values of R^2 while UV, FUB and C2RCC show the highest values of relative errors and the lowest values of $R^{2.}$

Table 12: Statistical parameters of the retrieval of chl-a. The bold value highlights the best value for a given parameter.

	UV	SS	SWIRE	MUMM	NASA	NIRSWIR	Polymer	FUB	OC-SMART	C2RCC
RMSE (mg.m^{-3})	3.65	3.55	3.58	2.54	**1.95**	2.02	2.25	3.06	5.86	0.31
Relative Error (%)	35	23	27	18	**14**	14	23	36	17	76
Bias (mg.m^{-3})	-1.51	-1.45	-1.57	-0.63	-0.66	-0.70	-0.68	**-0.49**	0.80	-0.014
R^2	0.28	0.45	0.43	0.64	**0.86**	0.85	0.75	0.41	0.68	0.25

4) Discussion

NIRSWIR is based on a switching algorithm using either the SWIR bands or NASA algorithm to estimate the aerosol reflectance. To study the advantage of using NIRSWIR compared to NASA (i.e., the advantage to use SWIR bands), we investigate how often NIRSWIR switched to using the SWIR bands. On the individual and common match-ups dataset, NIRSWIR used 51 and 13 times (out of 426 and 83, respectively) the SWIR bands, respectively. This means that the switching procedure is seldom chosen because of the threshold on the turbidity index in NIRSWIR. This is in accordance with Zhang et al. (2018). Figure 21 shows the scatterplot of R_{rs} estimated by NASA vs R_{rs} estimated by NIRSWIR on the individual match-ups dataset. NIRSWIR used the SWIR for all levels of R_{rs}. However, the number of match-ups is lower for NSWIR (431 for NSWIR and 510 for NASA) while Zhang et al. (2018) showed that NIRSWIR could provide more R_{rs} retrievals compared to NASA. This means that the MODIS-AQUA SWIR bands are not optimal for our *in-situ* dataset as they are not defined for studying the ocean. This is in

line with findings by Werdell et al. (2010), Wang and Shi (2012), Goyens et al. (2013) and Carswell et al. (2017).

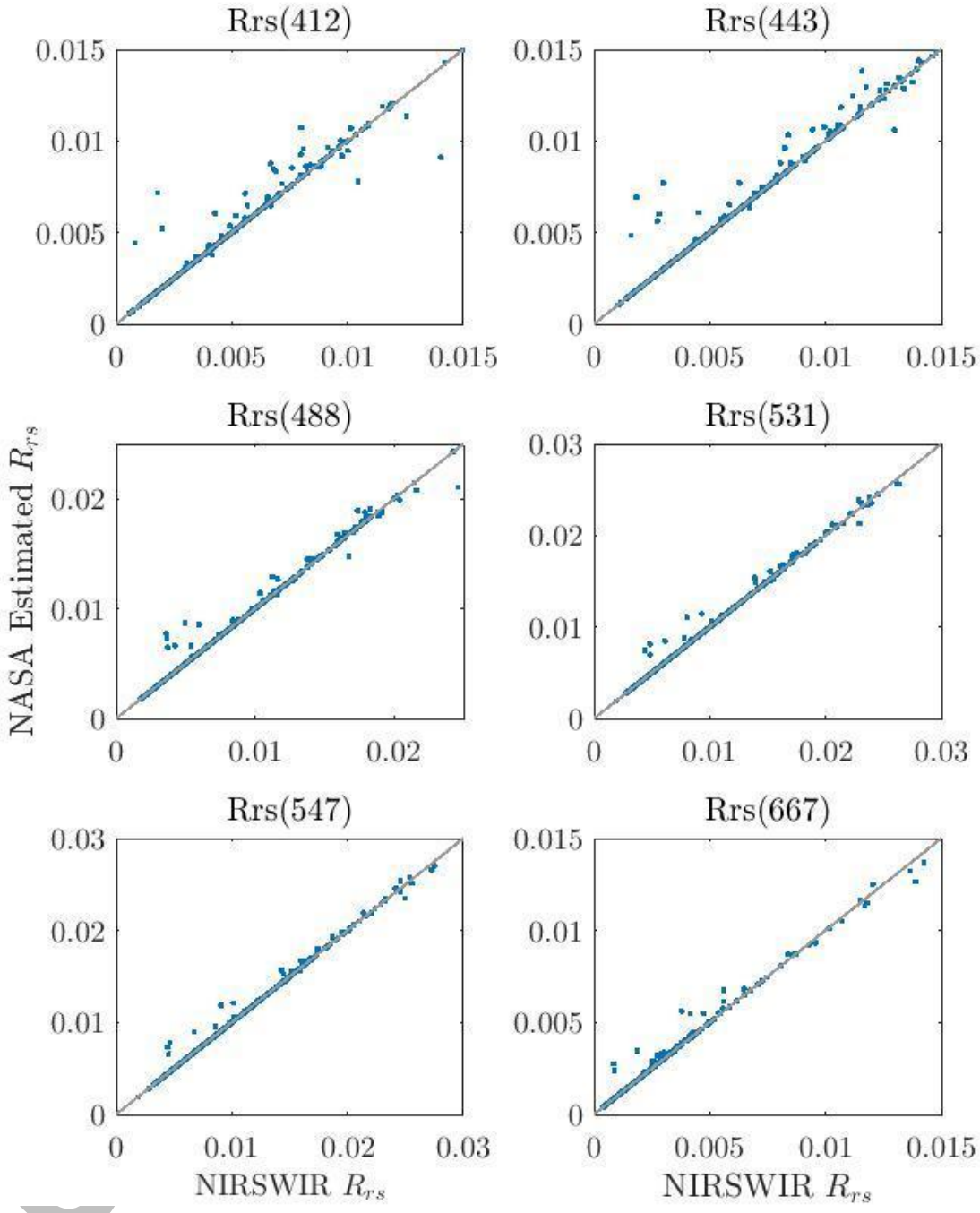

Figure 21: Scatterplot of NASA estimated R_{rs} vs NIRSWIR estimated R_{rs} from 412 (top left) to 667 nm (bottom right) over the individual match-ups dataset.

Statistics were calculated on the 51 valid match-ups where the SWIR bands were used instead of the NIR bands (Table 13). On our *in-situ* dataset (i.e. including only low-to-moderately turbid waters) switching to the SWIR bands does not provide any advantages as the statistics are less favorable when using these bands. This might be explained by the low SNR in these bands and our waters being moderately turbid. Liu et al. (2021) showed that the turbidity index used in the NIR-SWIR AC for the

switching scheme is not always equal to one and varies between 0.7 and 2.2 depending on the aerosol concentrations and observing geometries.

Table 13: Statistics for the 51 match-ups using the SWIR bands. The bold value highlights the best value for a given parameter.

Wavelengths	**412**	**443**	**488**	**531**	**547**	**667**
Relative error (%) NASA	**29**	**18**	**12**	**11**	**11**	**19**
Relative error (%) NIRSWIR	35	23	15	12	12	22
RMSE NASA	**0.0021**	**0.0018**	**0.0018**	0.0020	0.0021	0.0011
RMSE NIRSWIR	0.0022	0.0020	0.0020	0.0020	0.0021	0.0011

For the comparison on the OWT, NIRSWIR provides less matchups on the individual matchups dataset than NASA for all OWTs except OWT 3 (8 vs 8) and OWT 8 (34 vs 33). The biggest difference is observed for OWT 4 and 6: 114 vs 86 and 177 and 151, respectively.

NASA and NIRSWIR are vicariously calibrated which is not the case for the other algorithms. This could explain why these algorithms provide the most accurate and stable retrievals.

OC-SMART was developed based partly on a synthetic dataset generated by using the COASTCOLOUR (Ruddick, 2010) bio-optical model for coastal waters (among others) and validated using AERONET-OC data, which could explain why this algorithm is one of the most suitable for our *in-situ* dataset. Actually, OC-SMART is based on three different bio-optical models and constructed to provide a seamless transition between clear open ocean water and turbid coastal waters (Fan et al. 2021).

UV uses the hypothesis that in the UV spectral range, the ocean is totally absorbing due to sediments or CDOM. MODIS-AQUA does not have UV bands so the version of UV algorithms used the band at 412 nm as the "UV" bands. This can explain why the retrieval at 412 and 443 nm are not accurate with this algorithm. The PACE sensor will have UV bands and the UV algorithm may be more suitable for this ocean color sensor. Moreover, UV uses a spectrally flat aerosol reflectance. This second assumption is valid for coastal and maritime aerosol models, typical of coastal regions. Unfortunately, the aerosol models with the AERONET-OC data are not directly available. He et al. (2012) showed that their algorithm under-estimated the water-leaving reflectance for extremely turbid waters. However, our *in-situ* dataset does not represent extremely turbid waters as the maximum estimated *in-situ* SPM values is 32.2 $mg.m^{-3}$. One advantage of this algorithm is that it does not provide any negative values of R_{rs}.

SS14 is based on three thresholds calculated using ratios of L_{rc} through a κ parameter. SS14 was validated using in-situ measurements along the coasts of India (sediment-laden waters) and in open ocean waters. κ is used to calculate a reference spectrum which is then used to estimate the aerosol reflectance in the visible and NIR infra-reds. When we look at the estimates when κ values are considered as in-water bloom or floating bloom, the accuracy of the retrievals decreases. It means that SS14 took turbid waters for floating bloom or in-water bloom. The definition of κ should be revised to better discriminate the turbid waters. An updated version of this algorithm (UV-NIR) has been published by Singh et al. (2019) for considering extremely turbid waters using the band at 412 nm and

has been applied to HICO images and compared to SS14. The retrievals are compared to AERONET-OC data and the results showed an improvement of the estimation of R_{rs} with UV-NIR.

SWIRE assumes that the ocean is totally absorbing in the SWIR bands even for high sediments concentrations and is based on an extrapolated Rayleigh-corrected reflectance defined as $\rho_{ef} = ae^{b\lambda}$, where a and b are fitting coefficients, the values of which were different for each pixel using the 1.24, 1.64, and 2.13 µm bands. The authors assumed that ρ_{ef} is the aerosol-related reflectance and therefore can be used to estimate the aerosols parameter ε(748,869) and then the contribution of the aerosols in the visible bands. The lower number of match-ups might be explained by the non-adequacy of the extrapolation function and by the fact that the ocean is not totally absorbing for high concentrations of sediments in the SWIR bands (Knaeps et al., 2012).

V. Results on the simulated dataset

In this section, we present the evaluation results over the simulated dataset for only the global match-ups dataset for brevity. Because of the inherent assumptions in MUMM (spatial estimation of the aerosol ratio over a region of 1°-by-1°), this algorithm is not included in this study. C2RCC is also not included because of the inability to process the simulated dataset format.

1) Individual match-ups studies

We present here the results for all individual match-ups obtained by each AC algorithm. Figure 22 shows the scatterplots of the satellite-retrieved R_{rs} vs the simulated values for all eight AC algorithms and Table 14 provides the statistical results. 12,301 simulated cases are considered as turbid waters (with the same threshold as Robinson et al. (2003).

The first result concerns the number of match-ups. As shown in Table 13, the number of match-ups highly varies from 3007 for FUB to 12,198 for SS14. The number of retrievals for FUB is low because of the different flags inherent to this algorithm. The input parameters are checked if their values are inside the range of values of the dataset used to train the NN. In addition, to this min/max 'out of range' test, we also excluded simulated data for FUB that were not within the simulated concentration ranges used to train the network specifically, CHL=[0.05-50] $mg.m^{-3}$, SPM=[0.05-50] $g.m^{-3}$ and CDOM=[0.005-1] m^{-1}

Negative R_{rs} can also be retrieved. It is the case for NASA (between 45 (0.6%) at 547 nm and 574 (7.4%) at 412 nm), NIRSWIR (between 73 (0.9%) at 547 nm and 666 (7.8%) at 412 nm), SS14 (between 13 (0.1%) at 488 nm and 90 (0.7%) at 443 nm), SWIRE (between 9 (0.1%) at 667 nm and 4151 (52%) at 412 nm) and UV (between 842 (8%) at 547 nm and 1781 (17%) at 412 nm) while Polymer, FUB, and OC-SMART do not yield any negative results. It is also worth to note that the number of matchups obtained with NIRSWIR is higher than the number obtained with NASA with a value of 8,499 for NIRSWIR and 7,720 for NASA. It shows the contribution of the scheme developed in NIRSWIR for highly turbid waters.

Figure 22 shows that “scatter” (spread) is observed at all wavelengths. This is especially true at 412 nm for all AC, except OC-SMART. The scatter tends to decrease with increasing wavelength. However, few algorithms still show high scatter for all bands (SWIRE, SS14) while FUB, OC-SMART and Polymer show a decrease of a scattering around the 1:1 line at 488, 531 and 547 nm. OC-SMART shows the least scatter. This can be explained as this NN was partly trained using simulated datasets generated by a forward radiative transfer model for the coupled atmosphere-ocean system (Stamnes et al., 2018) similar to the one used in this study. SWIRE, UV and FUB show over-estimation of R_{rs} at most wavelengths while SS14 shows under-estimation for all wavelengths. Polymer tends to over-estimate R_{rs} at 412 and 443 and to slightly under-estimate R_{rs} at 488, 531 and 547 nm. NASA and NIRSWIR slightly over-estimate R_{rs} at 412 and 443 nm and do not show any bias at the other wavelengths.

This translates into the statistical parameters (Table 14). The relative errors are the highest at 412 (between 3.5% for OC-SMART and 123% for SWIRE) and 443 nm (between 3.2% for OC-SMART and 79% for SWIRE) and the lowest at 531 and 547 nm (between 2.6% for OC-SMART and 45% for SS14 at

531 nm and between 2.7% for OC-SMART and 46% for SWIRE at 547 nm). The high scatter at 412 and 443 nm can also be seen with the slope of the regression lines with the lowest values (between 0.43 for SS14 and 0.99 for OC-SMART at 412 nm and between 0.42 for S14 and 1 for OC-SMART at 443 nm) and the closest values of the slope to 1 are obtained at 531 and 547 nm (between 0.48 for SS14 and 1 for OC-SMART at 531 nm and between 0.48 for SS14 and 1 for OC-SMART at 547 nm). The low values of the slope for SS14 is explained by the high under-estimation of the retrievals obtained with this algorithm. The values of the slope are correlated with the values of the correlation coefficient R^2 with the lowest values at 412 (between 0.0001 for SWIRE and 0.99 for OC-SMART, values being lower than 0.45 for all AC except OC-SMART, FUB and NIRSWIR) and 443 nm (between 0.015 for SWIRE and 0.99 for OC-SMART, values being lower than 0.7 for all AC except for OC-SMART and FUB) and the highest values at 531 (between 0.58 for SWIRE and 0.99 for OC-SMART, values being higher than 0.70 for most of the AC) and 547 nm (between 0.65 for SWIRE and 0.99 for OC-SMART, values being higher than 0.75 for most of the AC).

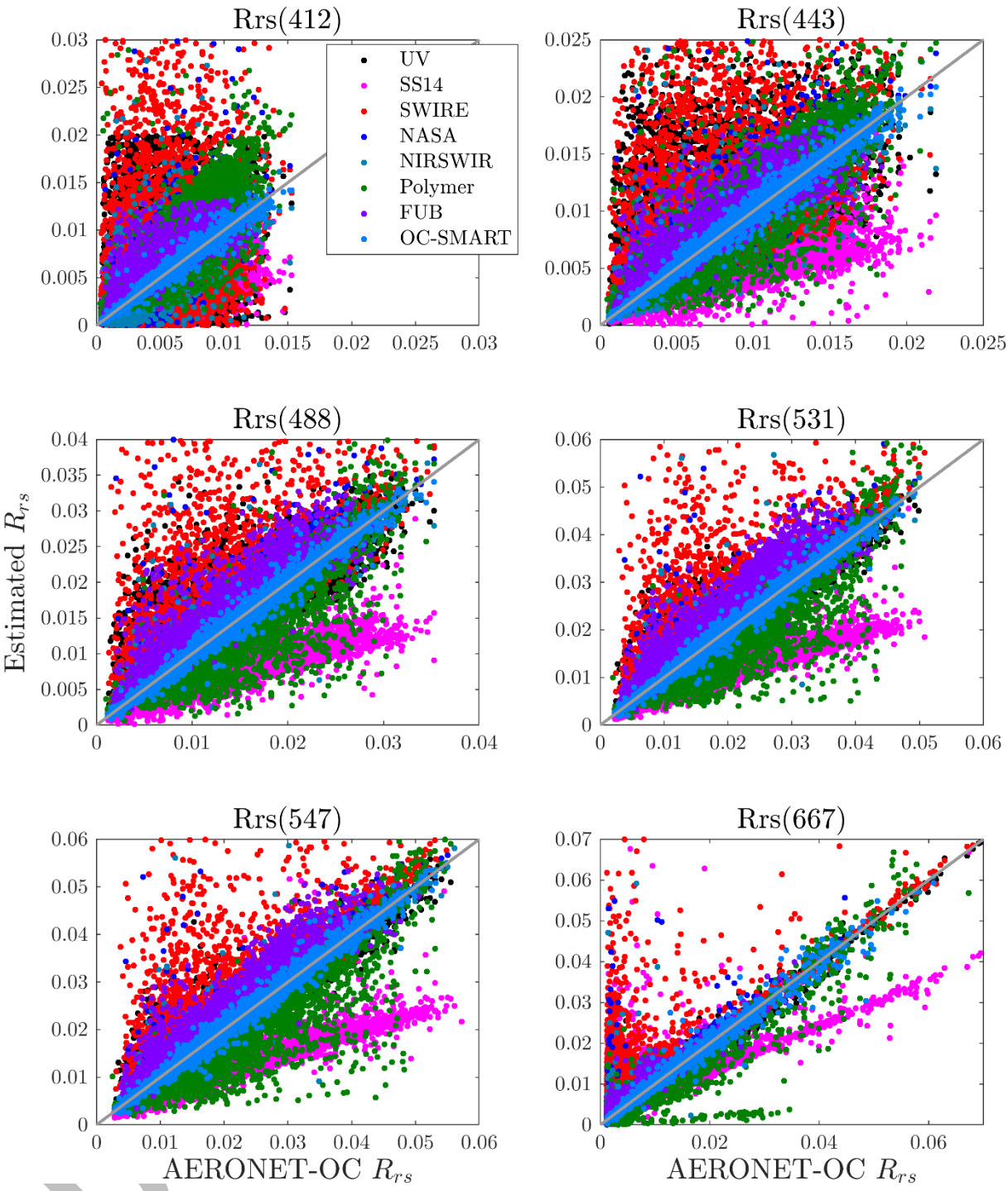

Figure 22: Scatterplots of the AC estimated R_{rs} vs simulated R_{rs} from 412 (top left) to 667 nm (bottom right). The individual scatterplots are provided in Appendix III

Table 14: The statistical results derived from the remote sensing reflectance, R_{rs} derived from various atmospheric correction algorithms and simulated data R_{rs} (*RE* - mean relative error, *RMSE* – root mean square error, R^2- regression, *Nvm*-number of valid data/model/wavelength).

	RE(%)	*RMSE* (sr^{-1})	Slope (sr^{-1})	Intercept	Bias (sr^{-1})	R^2	*Nvm*	*#<0*
NASA STD AC Model								
R_{rs} *(412)*	30	0.0029	1.08	$-2.62.10^{-5}$	0.00032	0.43	7720	574
R_{rs} *(443)*	18	0.0029	1.08	-0.00011	0.00038	0.59	7720	187
R_{rs} *(488)*	8	0.0028	1.05	-0.00020	0.00038	0.78	7720	55
R_{rs} *(531)*	5	0.0028	1.05	-0.00038	0.00034	0.86	7720	46
R_{rs} *(547)*	4	0.0027	1.05	-0.00044	0.00029	0.89	7720	45
R_{rs} *(667)*	14	0.0028	1.12	$-5.50.10^{-5}$	0.00039	0.67	7720	52
NIRSWIR AC Model								
R_{rs} *(412)*	24	0.0020	0.97	0.0026	0.00012	0.61	8499	666
R_{rs} *(443)*	14	0.0019	0.99	0.0024	0.00018	0.78	8499	340
R_{rs} *(488)*	6.2	0.0018	1.00	0.0020	0.00020	0.92	8499	140
R_{rs} *(531)*	3.7	0.0017	1.01	$9.27.10^{-5}$	0.00018	0.96	8499	78
R_{rs} *(547)*	3.2	0.0017	1.01	$4.56.10^{-5}$	0.00014	0.97	8499	73
R_{rs} *(667)*	9.7	0.0017	0.99	0.0003	0.00022	0.93	8499	159
SS14 AC Model								
R_{rs} *(412)*	53	0.00273	0.43	0.0017	-0.0011	0.24	12198	72
R_{rs} *(443)*	43	0.00388	0.42	0.0012	-0.0029	0.53	12198	90
R_{rs} *(488)*	47	0.00695	0.43	0.0009	-0.0059	0.79	12198	13
R_{rs} *(531)*	45	0.00896	0.48	0.0010	-0.0076	0.84	12198	0
R_{rs} *(547)*	46	0.00981	0.48	0.0009	-0.0083	0.86	12198	0
R_{rs} *(667)*	44	0.00409	0.60	0.0014	-0.0008	0.71	12198	0
SWIRE AC model								
R_{rs} *(412)*	123	0.0582	0.59	0.0041	0.0019	0.0001	8021	4151
R_{rs} *(443)*	79	0.0231	0.75	0.0048	0.0028	0.015	8021	1684
R_{rs} *(488)*	38	0.0092	0.88	0.0047	0.0030	0.28	8021	434
R_{rs} *(531)*	29	0.0081	0.96	0.0046	0.0039	0.58	8021	109
R_{rs} *(547)*	28	0.0081	0.99	0.0044	0.0041	0.65	8021	49
R_{rs} *(667)*	86	0.0061	0.97	0.0026	0.0024	0.66	8021	9

	RE (%)	*RMSE (sr^{-1})*	Slope *(sr^{-1})*	Intercept	Bias *(sr^{-1})*	*R^2*	*Nvm*	*#<0*
UV AC Model								
R_{rs} (412)	93	0.00430	0.48	0.0028	0.0002	0.08	10516	1781
R_{rs} (443)	52	0.00371	0.69	0.0026	0.0003	0.34	10516	975
R_{rs} (488)	23	0.00322	0.84	0.0026	0.0006	0.73	10516	864
R_{rs} (531)	13	0.00277	0.90	0.0022	0.0004	0.89	10516	844
R_{rs} (547)	11	0.00262	0.91	0.0020	0.0004	0.92	10516	842
R_{rs} (667)	37	0.00194	0.93	0.0006	0.0002	0.93	10516	844
Polymer AC Model								
R_{rs} (412)	80	0.00633	1.37	0.00129	0.00308	0.31	12116	0
R_{rs} (443)	38	0.00494	1.19	0.00091	0.00173	0.45	12116	0
R_{rs} (488)	16	0.00452	0.96	0.00072	0.00020	0.62	12116	0
R_{rs} (531)	11	0.00481	0.95	0.00030	-0.00059	0.74	12116	0
R_{rs} (547)	11	0.00497	0.94	$2.61.10^{-5}$	-0.00107	0.77	12116	0
R_{rs} (667)	19	0.00363	1.03	-0.00027	-0.00012	0.82	12116	0
FUB AC model								
R_{rs} (412)	36	0.00183	0.93	0.0014	0.00105	0.68	3007	0
R_{rs} (443)	24	0.00191	0.92	0.0014	0.00086	0.77	3007	0
R_{rs} (488)	26	0.00356	1.07	0.0017	0.00247	0.84	3007	0
R_{rs} (531)	30	0.00524	1.15	0.0019	0.00427	0.91	3007	0
R_{rs} (547)	25	0.00490	1.13	0.0017	0.00386	0.92	3007	0
R_{rs} (667)	38	0.00168	1.01	0.0011	0.00112	0.94	3007	0
OC-SMART AC model								
R_{rs} (412)	3.5	0.0003	0.99	$3.98.10^{-5}$	$4.78.10^{-6}$	0.99	12065	0
R_{rs} (443)	3.2	0.0003	1.00	$3.41.10^{-5}$	$4.92.10^{-6}$	0.99	12065	0
R_{rs} (488)	2.8	0.0005	1.00	$3.14.10^{-5}$	$5.53.10^{-7}$	0.99	12065	0
R_{rs} (531)	2.6	0.0007	1.00	$3.07.10^{-5}$	$-2.49.10^{-6}$	0.99	12065	0
R_{rs} (547)	2.7	0.0007	1.00	$2.24.10^{-5}$	$-4.28.10^{-6}$	0.99	12065	0
R_{rs} (667)	3.7	0.0006	0.99	$3.94.10^{-5}$	$-8.03.10^{-6}$	0.99	12065	0

Figure 23 shows the variation of the relative error and the root-mean-square error as a function of wavelength. For the relative error, we can observe the “smiley” shape, already mentioned in the match-ups sections. However, we can observe that some algorithms are less sensitive to wavelength in terms of RMSE (NASA, NIRSWIR, OC-SMART and Polymer) while others are more sensitive to wavelength (SS14, FUB, SWIRE). For the relative error, most of the algorithms show the lowest errors at 531 and 547 nm (Table 14). SS14, FUB and OC-SMART are not very sensitive to wavelength while SWIRE, UV and Polymer are very sensitive, especially at 412, 443, and 667 nm.

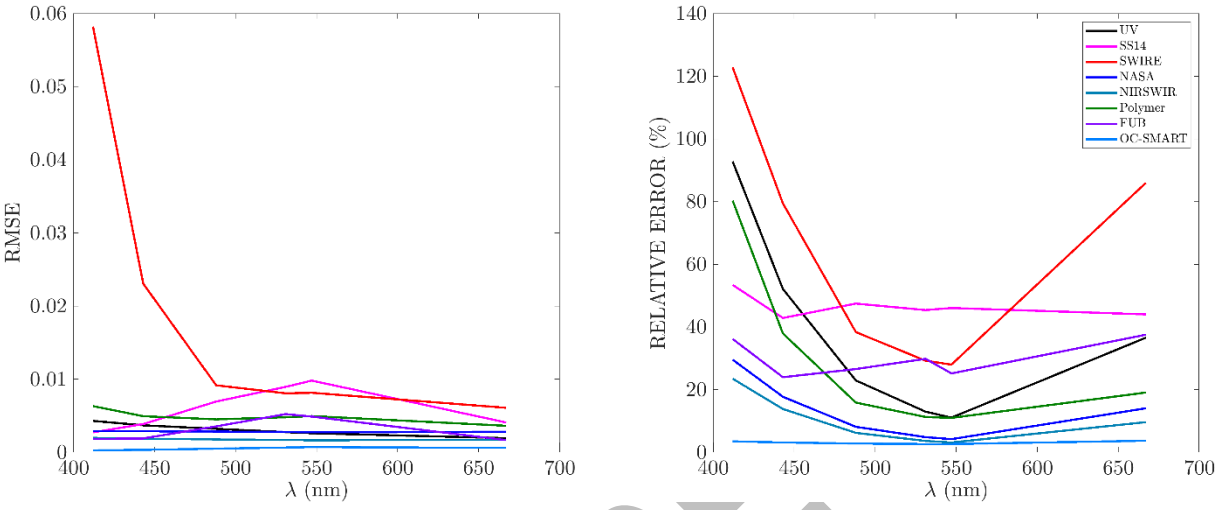

Figure 23: (a) Variation of the relative error as a function of wavelength, (b) Variation of the RMSE as a function of wavelength.

Figure 24 shows a spider plot of all statistical parameters (except the intercept of the regression line). The accuracies of the AC algorithms depend on wavelength, as mentioned earlier. In the blue bands (412 and 443 nm), OC-SMART, NASA, NIRSWIR are the most accurate. At 667 nm, most of the algorithms do not provide accurate retrievals of R_{rs} as the statistical parameters are not overall consistent. At 531 and 547 nm, NASA, NIRSWIR, OC-SMART, UV and Polymer provide accurate retrievals. Overall, NASA, NIRSWIR and OC-SMART are the most accurate AC algorithms and SS14 and SWIRE are the least accurate AC algorithms on our simulated dataset.

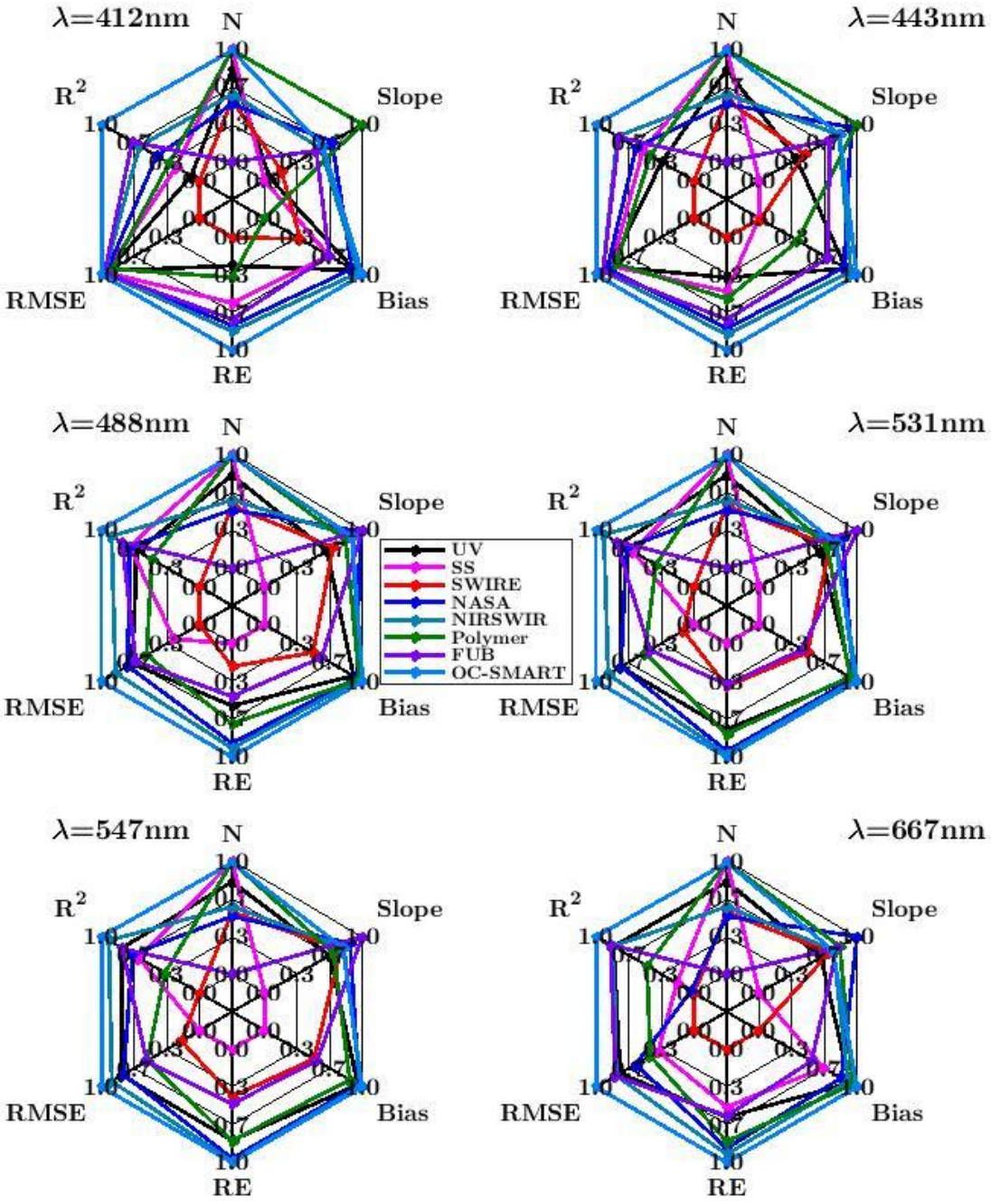

Figure 24: Spider-plot of the normalized statistical parameters as a function of wavelength.

We now study the capability of the algorithms to retrieve the shape of the spectra. The previous analysis only considered the retrieval by wavelength. Here we use different statistical parameters (QAS, χ^2, SAM) to analyze the shape of the retrieved spectra. The results are presented in Table 15. We first compared the retrieved spectra to reference spectra through the QAS parameter. A majority of the algorithms retrieve realistic spectra with values of QAS higher than 0.93 for NIRSWIR, NASA, Polymer, and OC-SMART. Four algorithms show less realistic spectra with QAS values lower than 0.90 (0.81 for UV, 0.85 for SWIRE and 0.87 for SS14 and FUB). χ^2 and SAM compare the retrieved spectra to our simulated spectra. NIRSWIR, NASA, FUB and OC-SMART present the lowest values of those parameters (5.77%, 7.73%, 3.88% and 0.17% for χ^2; 2.03°, 2.26°, 3.32° and 0.47° for SAM). As UV and

SWIRE yield high inaccuracies at 412 and 443 nm, they show the highest values of χ^2 (150.65% and 130.29%, respectively). SS14 shows the highest value of SAM (9.33°).

Table 15: Values of the statistical parameters calculated over the entire spectra. The bold value highlights the best value for a given parameter.

ALGORITHMS	QAS	χ^2 (%)	SAM (°)	S_{tot}
UV	0.81	150.65	7.41	29.05
SS14	0.87	27.40	9.33	18.40
SWIRE	0.85	130.29	7.01	11.61
NIRSWIR	0.93	5.77	2.03	37.41
NASA	0.93	7.73	2.26	33.32
Polymer	**0.95**	23.21	7.81	30.30
FUB	0.87	3.88	3.32	26.25
OC-SMART	0.93	**0.17**	**0.47**	**41.93**

We calculated the overall score which considers the accuracies per wavelength and the shape of the spectra (Table 15). The maximum value of the score is 42. There is one group of AC algorithms with values higher than 33 (NASA (33.32), NIRSWIR (37.41) and OC-SMART (41.93)) and one group with values lower than 20: SWIRE (11.61) and SS14 (18.40). A third group show values between 20 and 33 (FUB, UV, Polymer).

The simulated dataset is mainly representative of OWT 4 and then of OWT 3, 5 and 6. The most oligotrophic waters are not included in the simulated dataset as there are no retrievals for OWT 9. The total Score values per OWT is provided in Table 16. OC-SMART shows the highest values of the score for OWT 2 to OWT 8. For OWT 1, UV has the highest score (38.04) followed by NIRSWIR (36.20) and SWIRE (31.41) and Polymer has the lowest value (7.69), as expected. For this OWT, NASA and FUB do not provide any retrievals. NIRSWIR shows highest values of the score compared to NASA for OWT 2 to OWT 6. It shows the benefit to use the SWIR bands when the turbidity of the waters increases. NIRSWIR, NASA and Polymer are relevant for OWT 4 to OWT 6. UV and FUB show similar score values for OWT3 to OWT6.

Table 16: Total score values for all AC as a function of OWT.

	OWT1	OWT2	OWT3	OWT4	OWT5	OWT6	OWT7	OWT8	OWT9
UV	**38.04**	31.97	26.93	25.41	27.30	25.18	32.65	28.97	0
SS14	27.00	17.09	14.24	19.31	17.39	18.72	29.30	15.65	0
SWIRE	31.41	25.66	16.96	9.13	13.44	9.24	5.00	14.83	0
NASA	0	26.50	22.28	33.22	35.91	32.30	38.29	36.38	0
NIRSWIR	36.20	37.42	30.70	37.41	36.39	34.39	38.23	35.87	0
Polymer	7.69	22.14	27.79	31.44	30.38	31.52	33.83	26.71	0
FUB	0	23.84	23.73	25.01	26.18	22.82	27.32	21.49	0
OC-SMART	30.52	**40.00**	**41.88**	**42.00**	**41.97**	**41.98**	**41.50**	**40.84**	0

2) Sensitivity studies

Note that in these sensitivities' studies, we used all the simulated dataset without fixing any parameter. As mentioned previously, ideally, the sensitivities study should be done by fixing all parameters except one.

Sensitivity to τ(869)

Figure 25 shows the variation of the relative error on the retrieval of $R_{rs}(\lambda)$ as a function of τ(869) for all eight algorithms. For most of the AC, the relative error increases with the increase of τ(869). The relative errors are higher at 412 and 667 nm and lower at 531 and 547 nm. For SS14, the relative error shows a U-shape with the lowest values for τ(869) around 0.20-0.25. Two groups of algorithms can be observed depending on their values of the relative errors. A first group of algorithms (NASA, NIRSWIR, Polymer, OC-SMART, UV) for which the relative error is slightly dependent of the values of τ(869) and a second group (SWIRE, SS14, UV, FUB) for which the accuracy of the retrievals is highly dependent of the values of τ(869).

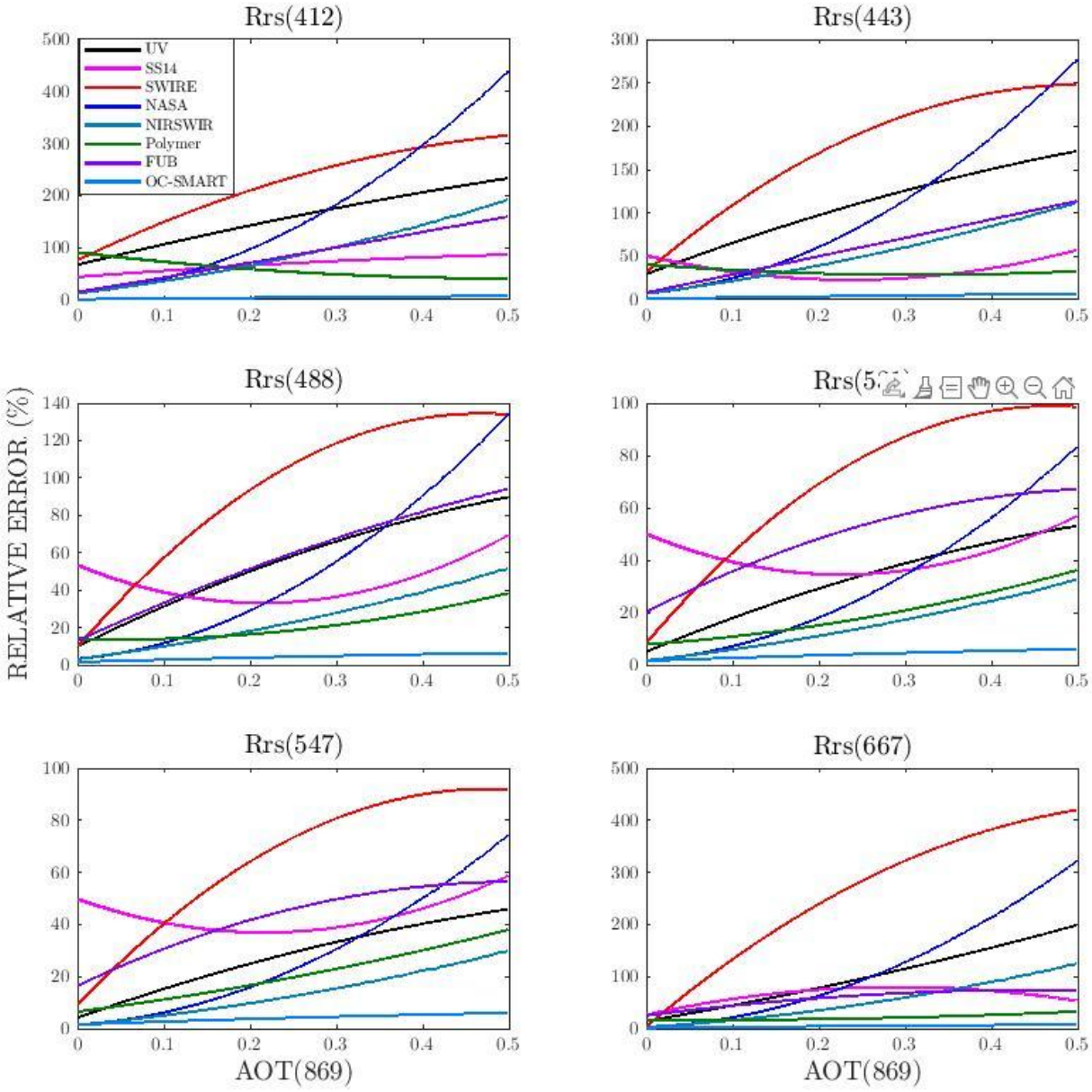

Figure 25: Variation of the relative error as a function of the aerosol optical thickness τ(869) for each wavelength.

Sensitivity to Angström coefficient

Figure 26 shows the variation of the relative error as a function of the Ångström coefficient α(443,869) for each wavelength. Compared to τ(869), the relative error is slightly dependent on the value of α(443,869) for all AC, except for SWIRE, UV and FUB. For SWIRE, the relative error sharply increases with the increase of α(443,869). For instance at 412 nm, the relative error increases from 20% (α(443,869)=-0.5) to 150% (α(443,869)=2.2). This behavior can be observed at all wavelengths. The values of the relative error vary slightly with wavelength with the lowest values at 488, 531 and 547 nm.

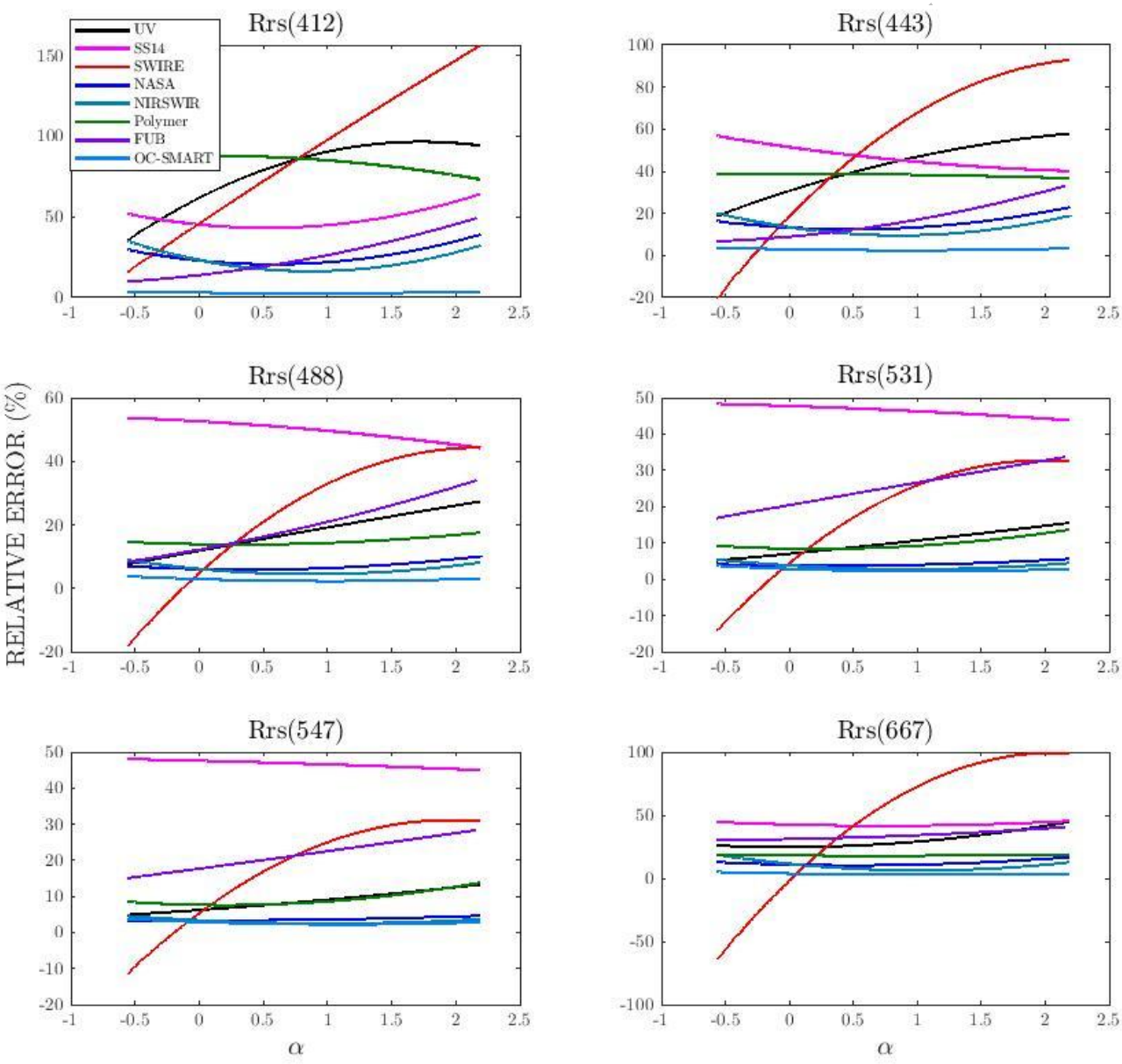

Figure 26: Variation of the relative error as a function of the Ångström coefficient α(531,869) for each wavelength.

Sensitivity to SPM

Figure 26 shows the variation of the relative errors as a function of SPM. The values of SPM vary from 0.09 to 493 mg.m^{-3}. However, some AC are not able to retrieve R_{rs} for values greater than 300 mg.m^{-3}. It is the case for SS14, NASA, NIRSWIR and FUB and OC-SMART. FUB algorithm shows the lowest range of values of SPM (up to 42 mg.m^{-3}), because of its flags. The behavior of the AC is very different. Some

algorithms show a U-shape of the relative error. It is the case for SWIRE and SS14, meaning that these algorithms perform better for a specific range of values of SPM. For instance, this range is [150-200] mg.m^{-3} for SWIRE. SS14 shows its highest relative errors from SPM around 130-140 mg.m^{-3} at 443, 488, 531 and 547 nm. At those bands, the relative errors are lower for the lowest and highest values of SPM for SWIRE. FUB shows a constant increase of the relative errors with the increase of SPM. This is also the case for Polymer and NASA. NIRSWIR is less sensitive to the values of SPM than NASA with relative errors of the same order as the ones from OC-SMART which is the AC providing the smallest relative errors at all wavelengths.

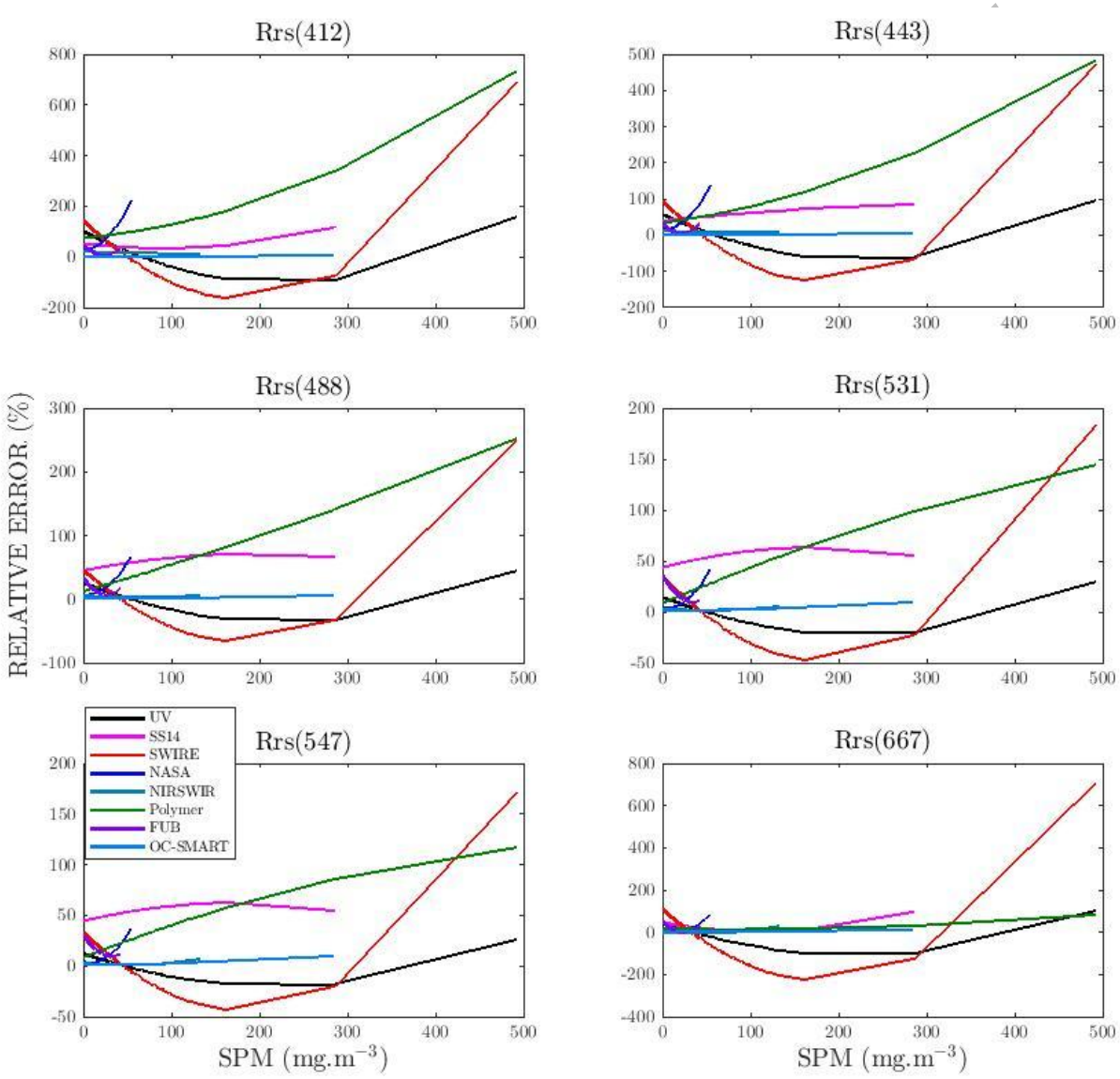

Figure 26: Variation of the relative error as a function of the suspended particulate matter (SPM) for each wavelength.

Sensitivity to CDOM

Figure 27 shows the variation of the relative errors as a function of CDOM. As for SPM, not all AC provide retrievals for the entire range of CDOM values. It is the case for NASA (max values=4.06 m^{-1}) and FUB (max values=0.99 m^{-1}). Most of the algorithms show a variation of the relative error as an inverted U-shape with lowest values of the relative error for the lowest and highest values of CDOM. This is not the case for SS14, NIRSWIR and OC-SMART for which the relative error does not seem to be

sensitive to the values of CDOM. At 667 nm, the relative error shows a different behavior, with a U-shape, with the lowest relative errors for a given range of CDOM.

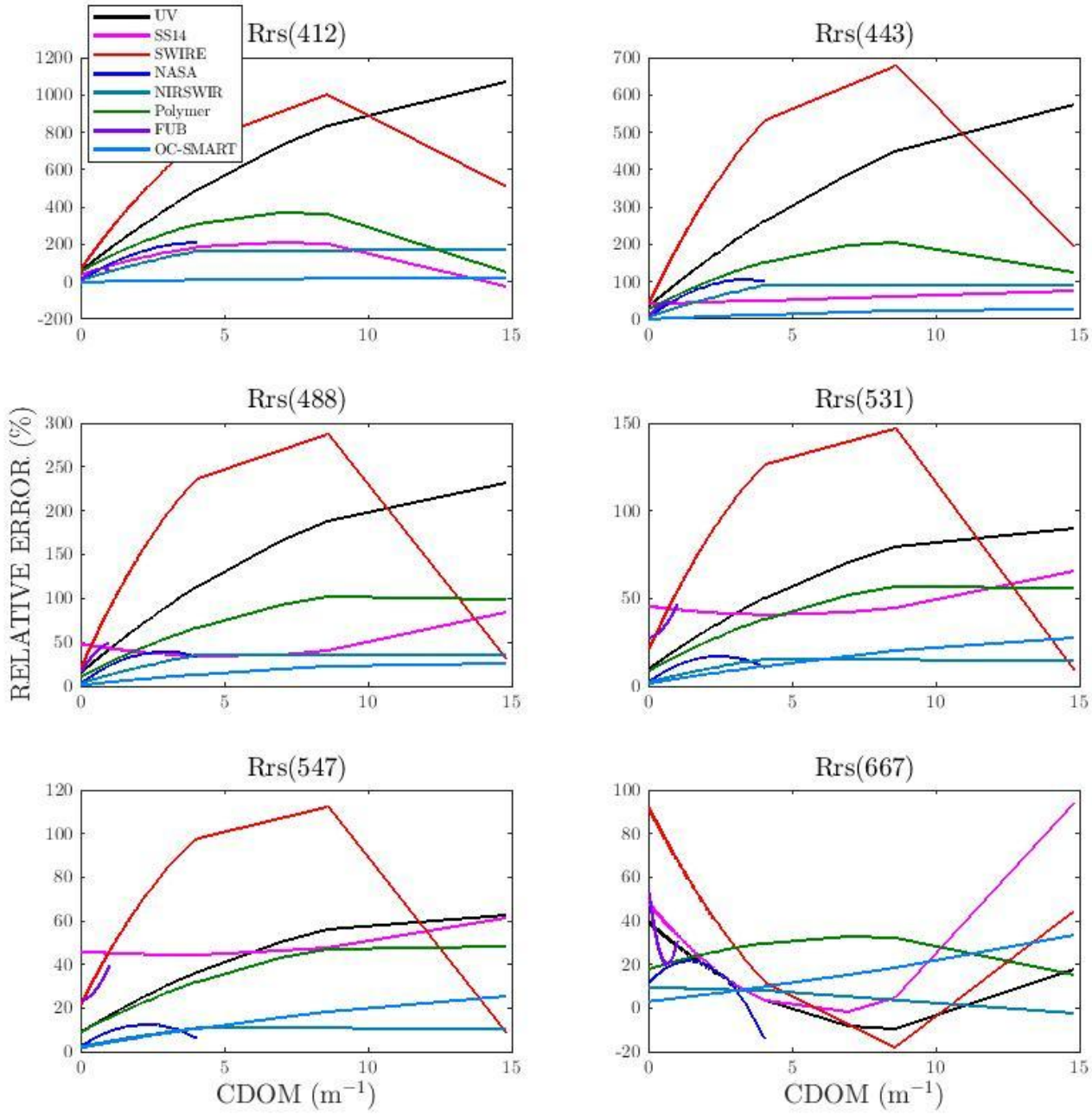

Figure 27: Variation of the relative error as a function of the CDOM value for each wavelength.

Sensitivity to CHL

Figure 28 shows the variation of the relative error as a function of the CHL value for each wavelength. The first thing to notice is the range of CHL values for each AC. As for SPM and CDOM, NASA is not able to estimate R_{rs} for the entire range of CHL ([0.83-214 mg.m^{-3}]) as well as FUB ([0.96-42 mg.m^{-3}]). Most of the algorithm shows an inverted U-shape of the relative error with CHL for wavelengths between 412 and 547. At 667 nm, the variation of the relative error shows a U-shape with the lowest relative errors for a specific range of CHL. Most of the algorithms are sensitive to CHL. OC-SMART, SS14, UV and NIRSWIR are the AC with the less sensitivity dependence to the increase of CHL. Polymer shows a strict increase of the relative error with the increase of CHL at 488, 531, 547 and 667 nm.

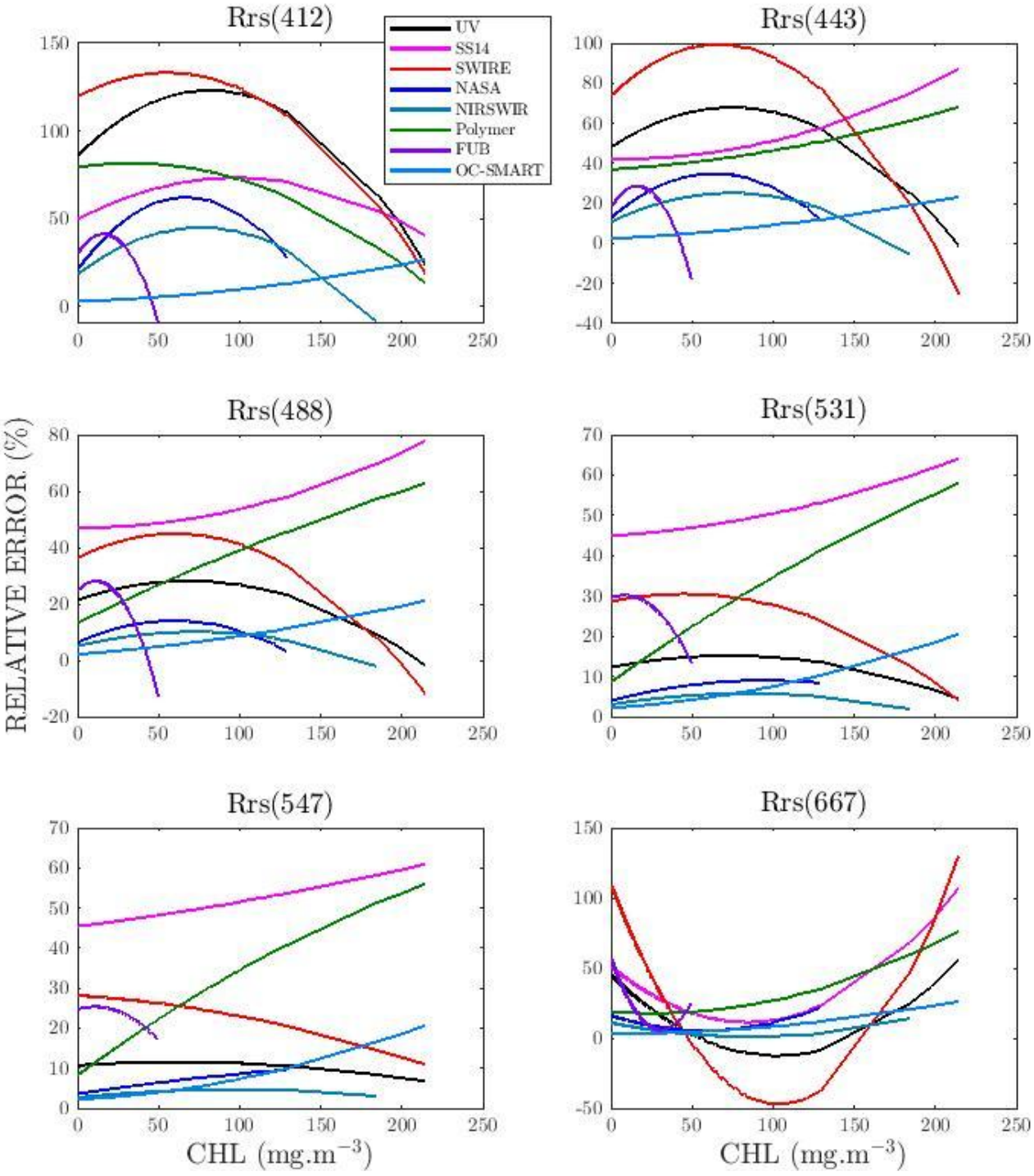

Figure 28: Variation of the relative error as a function of the CHL value for each wavelength.

Estimation of R_{rs} ratios

Figure 29 shows the ratios of $R_{rs}(\lambda)$ commonly used in chlorophyll-a retrieval algorithms estimated by the eight algorithms vs the simulated ratios. As expected, high scatter around the 1:1 line can be observed for $R_{rs}(443)/R_{rs}(547)$ and Rrs(488)/Rrs(547), especially for UV, SS14, SWIRE and Polymer. This is related to the large errors observed at 443 and 488 for these algorithms. In contrast, NASA, NIRSWIR

and OC-SMART show less scatter for this ratio. OC-SMART is the AC showing very good retrievals of all ratios, with almost no scatter around the 1:1 line. The scatter around the 1:1 line decreases as the wavelength increases. It translates to the RE and RMSE (Table 17), both parameters decreasing from $R_{rs}(443)/R_{rs}(547)$ to $R_{rs}(531)/R_{rs}(547)$. RE varies between 1.7% (OC-SMART) and 42% (Polymer) for $R_{rs}(443)/R_{rs}(547)$ and between 0.3% (OC-SMART) and 4% (FUB) for $R_{rs}(531)/R_{rs}(547)$.

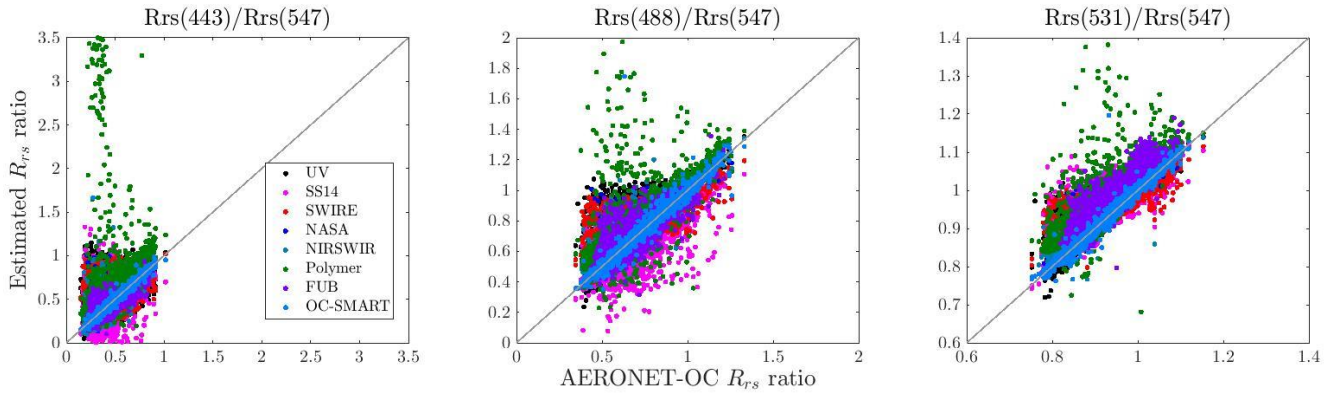

Figure 29: Scatterplot of the retrieved vs *in-situ* ratios of R_{rs} over the individual match-ups dataset: left panel: $R_{rs}(443)/R_{rs}(547)$; middle panel: $R_{rs}(488)/R_{rs}(547)$; right panel: $R_{rs}(531)/R_{rs}(547)$.

Table 17: Same as Table 2 but for ratios $R_{rs}(\lambda)/R_{rs}(547)$ with λ =443 or 488 or 531 nm on the individual match-ups dataset.

	RE(%)	*RMSE*	Slope	Intercept	Bias	R^2
NASA STD AC Model						
$R_{rs}(443)/R_{rs}(547)$	11	0.0.68	0.82	0.080	0.0072	0.66
$R_{rs}(488)/R_{rs}(547)$	3.3	0.038	0.91	0.077	0.0079	0.91
$R_{rs}(531)/R_{rs}(547)$	0.65	0.012	0.93	0.069	0.0042	0.96
NIRSWIR AC Model						
$R_{rs}(443)/R_{rs}(547)$	10	0.061	0.86	0.061	0.0056	0.72
$R_{rs}(488)/R_{rs}(547)$	3	0.033	0.93	0.055	0.0064	0.93
$R_{rs}(531))/R_{rs}(547)$	5.8	0.010	0.96	0.043	0.0035	0.97
SS14 AC Model						
$R_{rs}(443)/R_{rs}(547)$	29	0.147	0.62	0.198	0.0507	0.21
$R_{rs}(488)/R_{rs}(547)$	9.4	0.081	0.71	0.170	-0.0270	0.64
$R_{rs}(531)/R_{rs}(547)$	2	0.030	0.82	0.180	0.0108	0.73
SWIRE AC model						
$R_{rs}(443)/R_{rs}(547)$	33	0.248	0.59	0.200	0.0373	0.07
$R_{rs}(488)/R_{rs}(547)$	9.5	0.095	0.72	0.193	0.0020	0.51
$R_{rs}(531)/R_{rs}(547)$	1.7	0.025	0.79	0.194	0.0012	0.77
UV AC Model						
$R_{rs}(443)/R_{rs}(547)$	35	0.166	0.67	0.14	0.013	0.17
$R_{rs}(488)/R_{rs}(547)$	9.7	0.0.91	0.85	0.12	0.019	0.60
$R_{rs}(531)/R_{rs}(547)$	1.6	0.023	0.90	0.10	0.005	0.81
Polymer AC Model						
$R_{rs}(443)/R_{rs}(547)$	42	0.297	0.90	0.182	0.145	0.13
$R_{rs}(488)/R_{rs}(547)$	11	0.106	0.88	0.146	0.064	0.64
$R_{rs}(531)/R_{rs}(547)$	3.2	0.048	0.92	0.106	0.029	0.67
FUB AC model						
$R_{rs}(443)/R_{rs}(547)$	14	0.070	0.69	0.095	-0.027	0.62
$R_{rs}(488)/R_{rs}(547)$	8	0.071	0.79	0.143	-0.003	0.66
$R_{rs}(531)/R_{rs}(547)$	4	0.043	1.04	-0.0002	0.0351	0.80
OC-SMART AC model						
$R_{rs}(443)/R_{rs}(547)$	1.7	0.017	1.00	0.0005	0.00065	0.98
$R_{rs}(488)/R_{rs}(547)$	1.1	0.017	1.00	-0.0021	0.00033	0.98
$R_{rs}(531)/R_{rs}(547)$	0.3	0.005	1.00	-0.0027	0.00016	0.99

Estimation of chlorophyll-a concentration CHL

Figure 30 shows scatterplots of the MODIS-AQUA derived chl-a versus the chl-a used as input to develop the simulated dataset and Table 18 shows the statistical parameters. High scatter can be observed in Figure 30. This is especially true for UV and SS14. Most of the AC show an over-estimation of CHL. OC-SMART, NASA, NIRSWIR and FUB show the lowest scatter. Polymer, NASA and NIRSWIR show the lowest values of the relative errors (63%, 78% and 79%, respectively) while UV, SS14, SWIRE and Polymer show the highest values of RMSE (14.34, 25.93 14.03 and 14.11, respectively).

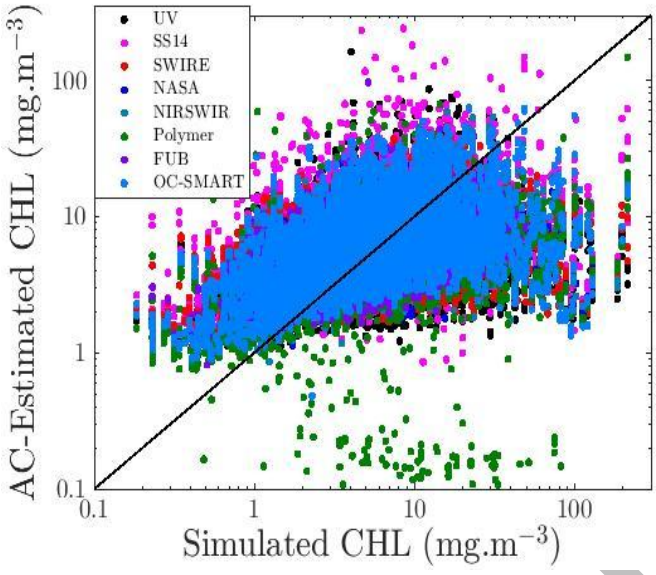

Figure 30: Scatterplot of the retrieved chlorophyll-a concentration chl-a vs exact simulated chl-a.

Table 18: Statistical parameters of the retrieval of chl-a

	UV	SS14	SWIRE	NASA	NIRSWIR	Polymer	FUB	OC-SMART
RMSE (mg.m^{-3})	14.34	25.93	14.03	9.95	12.15	14.11	**6.81**	12.31
Relative Error (%)	90	125	95	79	78	**63**	85	88
Bias (mg.m^{-3})	-2.08	-0.14	-2.29	-1.94	-2.38	-4.00	**-0.31**	-1.44
R^2	0.009	0.004	0.02	0.05	0.04	0.05	**0.10**	0.04

VI. Unconsidered corrections – additional complexity

In this chapter, we briefly describe other issues when observing coastal and inland waters which lead to additional uncertainties in the estimates of R_{rs}. The main issues are the contamination by the land to the TOA reflectance, the so-called adjacency effect and the presence of absorbing aerosols, such as smoke and dust. None of the AC algorithms used in this inter-comparison correct for those issues. There are difficult tasks to solve. Continuous efforts exist to tackle those issues. We present here a brief summary of the latest solutions.

1) Adjacency effects

Satellite measurements of coastal waters suffer from land adjacency effects. In coastal areas, a fraction of the light reflected by the land reaches the sensor. Adjacency effect occurs when light reflected by nearby land is scattered into the field of view of the sensor. The adjacency effect, thus, modifies the at-sensor radiance recorded of the water pixel. The magnitude of the adjacency effect depends on various factors, such as the aerosol optical properties and vertical distribution/scale height, the contrast between land and water albedo (wavelength dependent), viewing and illumination geometry, distance to land (Santer and Schmechtig, 2000; Bulgarelli and Zibordi, 2018a; Bulgarelli et al., 2018).

Adjacency effects are not confined to the first km offshore, particularly for highly reflecting land covers, in the NIR and for highly sensitive sensors. Extensive theoretical simulations of land adjacency effects in typical OC observation conditions (Bulgarelli and Zibordi, 2018b) (and summarized in IOCCG report #18, IOCCG (2019)) showed that the average adjacency effect in data from MODIS-A, MERIS, S3-OLCI, are still detectable (i.e. above the sensor noise level) up to 36 km offshore, except for adjacency effects caused by green vegetation at the red wavelengths.

When neglected, the adjacency effect can introduce significant errors in retrieving the water-leaving signal leading in complex ways to uncertainties in derived products. The impact of the adjacency effect however depends on the characteristics of the AC algorithm. For atmospheric correction schemes not deriving the atmospheric properties from satellite data and/or from the water pixel, simulations (Bulgarelli and Zibordi, 2017, 2018a) showed that adjacency effect induced artifacts in the water reflectance are positive for all wavelengths, with biases monotonically decreasing with distance from land. For atmospheric correction schemes inferring the aerosol properties from NIR data, biases are mainly negative apart from cloud-induced adjacency effects and perturbations induced by adjacency effects at NIR and visible wavelengths might compensate each other. Consequently, biases induced by adjacency effects on the water reflectance are not strictly correlated to the intensity of the reflectance of the nearby land.

Some studies exclude pixels within a fixed distance from the shoreline. The horizontal range of the adjacency effect is however not fixed and impacted by various factors such as the vertical distribution of aerosol in the atmosphere. A conservative threshold might remove water pixels which are not affected by land. Several approaches have been developed to identify and flag the pixels influenced by adjacency effects. Sterckx et al. (2011) proposed a method to flag pixels based on the deviations from the NIR similarity spectrum. Jiang et al. (2023) developed new optical water types (OWT) containing the land-affected signal to flag and mask land affected observations in inland water scenes. Feng and Hu (2017) explored the elevated radiance in the MODIS SWIR bands at 1240 and 2130 nm to develop a statistical method to quantify land adjacency effects. Burazerovic et al. (2013) proposed spectral unmixing techniques to quantify adjacency effects.

While full 3D Monte-Carlo simulations allow accurate simulation of adjacency effects, simplified formulations are needed for implementation of an operationally fast correction scheme. Physical correction approaches often involve the use of the atmospheric Point Spread Function (PSF), which allows calculation of contributions from neighboring pixels to the at-sensor radiance from a target pixel. To calculate the atmospheric PSF in a time-efficient manner, they mostly rely on the single scattering approximation (Santer and Schmecting, 2000). This primary scattering assumption is used in the sensor-independent adjacency correction algorithm developed by Kiselev et al. (2015). The adjacency correction module is integrated within the Modular Inversion and Processing (MIP) system (Heege et al., 2014). Also, the Improved Contrast between Ocean and Land (ICOL) processor (Santer et al., 2007; Santer and Zagolski, 2009) developed specifically for MERIS relies on the primary scattering assumption. RADCOR (Castagna and Vanhellemont, 2022) is a new physically based adjacency correction algorithm using dark Spectrum Fitting (DSF)-integrated adjacency correction algorithm working in the frequency domain. Some approaches incorporate empirical assumptions into the physical methods to determine the adjacency range or background contribution. Sterckx et al. (2015), for instance, proposed the SIMilarity Environment Correction (SIMEC) which estimates the contribution of the background iteratively by checking the correspondence of the retrieved water reflectance with the NIR similarity spectrum defined by Ruddick et al. (2006).

2) Absorbing aerosols

Most of the atmospheric correction algorithms do not consider absorbing aerosols (dust, smoke). It is especially true for the standard AC from the space agencies. The reason is that it is complicated to handle and all the already published methods are time-consuming. Absorbing aerosols, especially dust, are not detectable using only NIR bands as they have a spectral dependency and they have spectral absorbing signatures similar to optically active components of the ocean. Finally, they absorb in the shorter UV which makes them difficult to be detected by the NIR/SWIR algorithms.

Song et al. (2022) calculated the percentages of days dominated by maritime and dust, smoke, and mixed aerosols and found that absorbing aerosols occurred frequently over the coasts of the Sahara and Arabian desert, China, south-central Africa, and the Indian Peninsula, as shown in Figs. 31 (a) and (b). Moreover, Song et al. (2022) found that the impact of vertical distribution of absorbing aerosols was up to ±8% for dust and ±10% for smoke based on radiative transfer simulations, as shown in Fig. 31 (c). Two-layer atmosphere model may lead to errors of water-leaving radiance up to ~30%–40% in the cases of dust in traditional NASA standard AC algorithm (Song et al., 2022). Based on multiple years satellite lidar observations from CALIPSO, a prediction model of vertical distribution of absorbing aerosol was constructed, which can quantitatively estimate the vertical distribution of absorbing aerosol from the meteorological reanalysis products (Song et al., 2020).

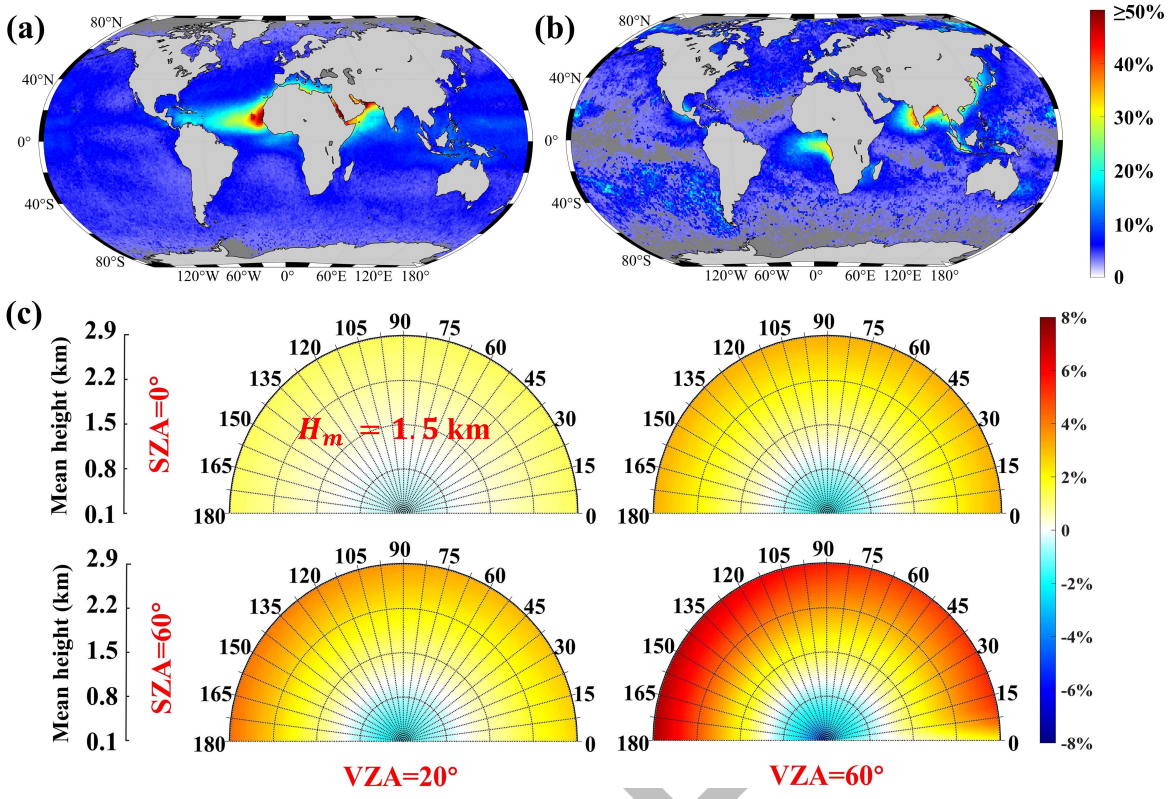

Figure 31: (a, b) Spatial distributions of the annual occurrence frequencies of (a) dust and (b) smoke aerosols over the ocean averaged from 2013 to 2020. Dark gray areas indicate no data. (c) Polar diagrams of the relative differences of simulated TOA reflectance (Δ_h) at 412 nm along the mean height (H_m) of dust aerosols (AOD = 0.3) and RAA with SZA (= 0° and 60°) and VZA (=20° and 60°) used for the radiative transfer simulations. Note that the radius of the polar diagram represents a change in H_m from 0.1 to 2.9 km in steps of 0.1 km, and the polar angle denotes a change in RAA from 0° to 180° in steps of 5°; RAA = 180° indicates that the sensor and the sun are in the same direction, corresponding to the solar plane. This figure was modified from Song et al. (2022).

Frouin et al. (2019) provides a review of the algorithms dealing with absorbing aerosols and the limitations of the current approaches. The AC incorporating absorbing aerosols have been mostly developed for open ocean waters (Moulin et al., 2001a, 2001b; Chomko and Gordon, 1998, Chomko et al., 2001; Nobileau and Antoine, 2005; Banzon et al., 2009; Mao et al., 2020) and were specifically designed to only detect absorbing aerosols. Few tackle at the same time non-zero R_{rs}(NIR) and absorbing aerosols. Those algorithms are based either on spectral optimization algorithms to estimate R_{rs} (Brajard et al., 2006, 2012; Kuchinke et al., 2009) or spectral relationships of the aerosol reflectance (Al Shehhi et al., 2017) or a modification of current algorithm such as Polymer (Zhang et al., 2019). Bai et al. (2020, 2023) developed a practical interpolation-based algorithm (UV-SWIR-AC algorithm) to remove absorbing aerosol effect in turbid waters.

Recently, Song et al. (2023) proposed an atmospheric correction algorithm (OC-XGBRT) to retrieve R_{rs} at short wavelength bands of visible light in the presence of absorbing aerosols, which considers the vertical distributions of absorbing aerosol. Based on the extensive simulation dataset, the OC-XGBRT algorithm was established using a machine learning method. The reflectance at the top of atmosphere and R_{rs} were simulated considering multiple types of absorbing aerosols (dust, smoke, and urban aerosols) and their vertical distribution under the comprehensive aquatic environment. Application results revealed that the OC-XGBRT algorithm substantially improved the quality of the retrieved R_{rs} at blue light bands compared with the original R_{rs} products in the presence of absorbing aerosols.

VI. Conclusions

Atmospheric correction over turbid waters is still a complex task and numerous atmospheric correction algorithms have been developed for the past twenty years. For end-users interested in using remote-sensing reflectance for estimating inherent optical properties of seawater or biogeochemical parameters, it can be difficult to know which algorithm to apply. In this IOCCG report, we compared ten atmospheric correction algorithms for MODIS-AQUA based on different assumptions and widely used for some of them. We performed a standard match-ups exercise using in-situ measurements from the AERONET-OC network and a simulated dataset to evaluate the accuracy of the different algorithms AC. As the AERONET-OC stations only represent low to moderate turbid waters, a simulated dataset has been developed for considering very turbid waters. We did not consider absorbing aerosols in the study as the aerosol models used in the simulated dataset are the ones included in the NASA processing.

Based on our analysis, we propose the following ranking for MODIS-AQUA depending on the optical water types. This ranking is based on the results of the general match-up and the simulated datasets, provided in Tables 19-21. It must be noted that the remarkable performance of OC-SMART on the simulated data is because the training of the algorithm included a very similar simulated subset generated with the same bio-optical used in this study except for the absorption of chlorophyll. The full training data of OC-SMART, however, includes a much larger set of simulations accounting for other bio-optical models and a significantly wider range of concentrations compared to the simulations tested in this study.

In summary:

- For MODIS-Aqua we recommend using OC-SMART, NIRSWIR and NASA standard for OWTs 3-8 and NIRSWIR for extremely turbid water with OWTs 1 and 2.
- UV shows best performance for extremely turbid waters classified as OWT 1.
- NIRSWIR shows consistently good performance across all OWTs.

Table 19: Algorithm ranking based on total score values of table 15 (simulated data set) excluding OWT 9. Note: No results available for MUMM and C2RCC. No outputs from NASA and FUB algorithms for OWT 1.

Rank	OWT								
	1	**2**	**3**	**4**	**5**	**6**	**7**	**8**	**9**
1	UV (38.04)	OC-SMART (40.00)	OC-SMART (41.88)	OC-SMART (42.00)	OC-SMART (41.97)	OC-SMART (41.97)	OC-SMART (41.50)	OC-SMART (40.84)	n/a
2	NIRSWIR (36.20)	NIRSWIR (37.42)	NIRSWIR (30.70)	NIRSWIR (37.41)	NIRSWIR (36.39)	NIRSWIR (34.39)	NASA (38.29)	NASA (36.38)	n/a
3	SWIRE (31.41)	UV (31.97)	Polymer (27.79)	NASA (33.22)	NASA (35.91)	NASA (32.30)	NIRSWIR (38.23)	NIRSWIR (35.87)	n/a
4	OC-SMART (30.52)	NASA (26.50)	UV (26.93)	Polymer (31.44)	Polymer (30.38)	Polymer (31.52)	Polymer (33.83)	UV (28.97)	n/a
5	SS14 (27.00)	SWIRE (25.66)	FUB (23.73)	UV (25.41)	UV (27.30)	UV (25.18)	UV (32.65)	Polymer (26.71)	n/a
6	Polymer (7.69)	FUB (23.84)	NASA (22.28)	FUB (25.01)	FUB (26.18)	FUB (22.82)	SS14 (29.30)	FUB (21.49)	n/a
7		Polymer (22.14)	SWIRE (16.96)	SS14 (19.31)	SS14 (17.39)	SS14 (18.72)	FUB (27.32)	SS14 (15.65)	n/a
8		SS14 (17.09)	SS14 (14.24)	SWIRE (9.13)	SWIRE (13.44)	SWIRE (9.24)	SWIRE (5.00)	SWIRE (14.83)	n/a

Table 20: Algorithm ranking based on total score values of table 7 (combined AERONET-OC match-ups) excluding OWTs 1, 2 and 9.

Rank	OWT								
	1	**2**	**3**	**4**	**5**	**6**	**7**	**8**	**9**
1	n/a	n/a	OC-SMART (26.02)	OC-SMART (40.56)	NASA (40.37)	OC-SMART (37.17)	NASA (36.23)	SS14 (37.41)	n/a
2	n/a	n/a	Polymer (24.21)	NASA (39.80)	NIRSWIR (39.58)	NASA (37.08)	NIRSWIR (36.23)	SWIRE (35.39)	n/a
3	n/a	n/a	NIRSWIR (21.96)	NIRSWIR (39.09)	OC-SMART (35.42)	NIRSWIR (37.08)	SS14 (31.17)	NASA (28.21)	n/a
4	n/a	n/a	UV (20.71)	Polymer (37.23)	MUMM (33.72)	MUMM (34.69)	MUMM (29.16)	NIRSWIR (28.21)	n/a
5	n/a	n/a	MUMM (18.39)	MUMM (33.32)	SS14 (26.03)	Polymer (31.07)	Polymer (29.01)	OC-SMART (26.76)	n/a
6	n/a	n/a	C2RCC (18.37)	UV (31.72)	FUB (24.80)	C2RCC (29.88)	OC-SMART (28.98)	FUB (24.05)	n/a
7	n/a	n/a	SWIRE (18.14)	FUB (26.79)	Polymer (24.78)	SS14 (25.59)	SWIRE (25.11)	MUMM (22.80)	n/a
8	n/a	n/a	SS14 (16.72)	SS14 (26.75)	SS14 (26.03)	FUB (23.93)	FUB (24.41)	C2RCC (20.19)	n/a
9	n/a	n/a	NASA (14.51)	SWIRE (21.90)	SWIRE (18.05)	UV (19.41)	UV (22.62)	UV (18.65)	n/a
10	n/a	n/a	FUB (12.37)	C2RCC (15.29)	C2RCC (17.40)	SWIRE (10.39)	C2RCC (11.13)	Polymer (12.87)	n/a

Table 21: Combined algorithm ranking based on the mean total score values of Tab 7 + 15 excluding MUMM and C2RCC in addition to OWTs 1, 2 and 9.

Rank	OWT								
	1	**2**	**3**	**4**	**5**	**6**	**7**	**8**	**9**
1	n/a	n/a	OC-SMART (54.89)	OC-SMART (62.28)	OC-SMART (59.68)	OC-SMART (60.57)	NASA (56.41)	OC-SMART (54.22)	n/a
2	n/a	n/a	NIRSWIR (41.55)	NIRSWIR (56.96)	NIRSWIR (56.18)	NIRSWIR (52.93)	NIRSWIR (56.35)	NASA (50.49)	n/a
3	n/a	n/a	Polymer (39.90)	NASA (53.12)	NASA (56.10)	NASA (50.84)	OC-SMART (55.99)	NIRSWIR (49.98)	n/a
4	n/a	n/a	UV (37.29)	Polymer (50.06)	Polymer (42.77)	Polymer (47.06)	Polymer (48.34)	UV (38.30)	n/a
5	n/a	n/a	FUB (29.92)	UV (41.27)	UV (39.14)	UV (34.89)	SS14 (44.89)	SS14 (34.36)	n/a
6	n/a	n/a	NASA (29.54)	FUB (38.41)	FUB (38.58)	FUB (34.79)	UV (43.96)	SWIRE (32.53)	n/a
7	n/a	n/a	SWIRE (26.03)	SS14 (32.69)	SS14 (30.14)	SS14 (31.52)	FUB (39.53)	FUB (33.52)	n/a
8	n/a	n/a	SS14 (22.60)	SWIRE (20.08)	SWIRE (22.47)	SWIRE (14.44)	SWIRE (17.56)	Polymer (33.15)	n/a

The following table provides a brief overview of some of the advantages and limitations of the algorithms:

	Advantages	**Limitations**
UV	• Good applicability for high turbid or eutrophic waters • No aerosol models • No bio-optical models	• Need the assumption of negligible water-leaving radiance at UV or short blue bands which is not suitable for low turbidity waters • Applicable only to weakly absorbing aerosols
SS14	• Atmospheric correction per optical water types • Calculation of a single parameter κ • Empirical relationships to correct the aerosol radiance	• Applicable only to weakly absorbing aerosols • Empirical relationships

	• No aerosol models • Easy to implement	• Extrapolation to estimate the aerosol radiance • Results deteriorated in dense bloom waters
SWIRE	• Based on Gordon and Wang (1994) for the first step • Developed for suspended sediments • Use of SWIR bands • Empirical function to extrapolate the Rayleigh-corrected reflectance from SWIR to NIR used as a reference	• Applicable only to weakly absorbing aerosols • Extrapolation depend of the dataset used to define the function
MUMM	• No need aerosol models • No bio-optical models • Available for SeaWiFS, MODIS-AQUA, MERIS and OLCI • Based on Gordon and Wang (1994) for the first step	• Three steps • Need to estimate the epsilon parameter for each pixel of a given image • The ocean parameter, α, is not constant when the turbid is high • Applicable only to weakly absorbing aerosols
NASA	• Diverse optical domains • 80 aerosol models • iteration processing • Based on Gordon and Wang (1994) for the first step	• Need aerosol models • Use of empirical optical models (e.g. spectral backscattering, particulate and dissolved absorption) limits the applicability • Practical implementation of the iteration scheme can result in conditions of non-convergence • Applicable only to weakly absorbing aerosols • Need a first step
NSWIR	• No bio-optical model • Assumption of black pixel	• Need aerosol models •Extrapolation of model aerosol from SWIR to VIS • Applicable only to weakly absorbing aerosols
Polymer	• Spectral matching inversion • No aerosol models • Spectral approximation of the atmospheric component • Analytical formulation does not rely on aerosol models • Correction of Sun glint • Applicable to moderately absorbing aerosols • Available for MODIS-AQUA, MERIS and OLCI	• Limited to moderate turbid waters due to the bio-optical model •Need bio-optical model

FUB	• Direction inversion of full spectral TOA radiance signal • Fast to process data once the networks are trained • Bio-optical model used on forward radiative transfer simulations based on European coastal waters • No negative reflectance retrieval due to logarithmic transformation of the training data • Robust to input errors as training included noise • Available for MODIS-AQUA, MERIS and OLCI. The MERIS and OLCI plugins for SNAP also provide estimates of Chl-a, TSS and CDOM with per-pixel uncertainties included for OLCI	• Applicable only to weakly absorbing aerosols • Limited to moderately turbid waters with maximum concentrations of 50 g.m-3 for TSS and 50 mg.m-3 for Chl-a with CDOM at 443 nm not exceeding 1 m^{-1} • Dependent of the training dataset
OC-SMART	• Global application: OC-SMART is applicable in both open ocean and coastal/inland waters, as well as in extreme conditions such as heavy aerosol loadings, extremely turbid water, etc. • Reliability: OC-SMART provides a complete resolution of the negative water-leaving radiance issue which plagues heritage AC algorithms. • Flexibility: The framework of OC-SMART is, in principle, applicable to any suitable combination of spectral bands but requires some effort in forward/inverse modeling and validation to fully integrate a new sensor. • Noise handling: OC-SMART appears to be weakly affected by noise in the satellite measurements and therefore applicable to sensors with low signal to noise ratio (SNR). • Accuracy: OC-SMART provides improved retrievals of water-leaving radiances and ocean IOPs compared to the heritage algorithms, especially in complex coastal and inland water areas. • Robustness: OC-SMART appears to be robust and resilient to contamination due to sunglint and adjacency effects of land or cloud edges based on extensive testing (not documented in this report). • Efficiency: OC-SMART is fast (about 10 times faster than NASA's SeaDAS package) and suitable for operational use. • Multi-sensor support: OC-SMART currently supports 11 sensors: SeaWiFS, Aqua/MODIS, SNPP/VIIRS, ISS/HICO, Landsat8/OLI, DSCOVR/EPIC, Sentinel-2/MSI, Sentinel-3/OLCI, COMS/GOCI, GCOM-C/SGLI and FengYun-3D/MERSI2. • Earth curvature effects are considered in the radiative transfer model (RTM) for the coupled atmosphere-ocean system employed to generate the synthetic dataset used for MLNN training.	• Applicable only to weakly absorbing aerosols • Based on a scalar RTM (polarization effects not considered) • Coupled RTM based on a flat air-water interface (surface roughness effects not included) – sky glint and "weak" sun glint included, but not "strong" sun glint • Inelastic scattering processes (Raman, fluorescence scattering) not included in RTM • Dependent of the training dataset

	• Implementation of OC-SMART for application to PACE/OCI data is in progress.	
C2RCC	• Direct inversion • Fast to process the images • Available for OLCI, MERIS and MODIS-AQUA	• Dependent of the training dataset

Applicability to other sensors:

As mentioned, this round-robin comparison of AC was applied to MODIS-AQUA. But the results of this report should be applicable to other sensors. NASA has been tuned to process all major ocean color satellite images including OLCI. Algorithms based on the direct inversion of the full TOA spectral signal such as FUB, CR2CC and OC-SMART are expected to perform differently when applied to other Ocean Colour missions. We expect the accuracy will increase with an increased number of spectral bands such as for OLCI, and slightly decrease for sensors with less bands compared to Aqua such as VIIRS. The overall performance of these NN-based methods however, will strongly depend on the applicability of the training data set and underlying bio-optical model assumptions. Hieronymi et al. (2023) compared five atmospheric correction algorithms for the OLCI-A and -B on-board Sentinel-3 using mainly the AERONET-OC in-situ dataset. Polymer and C2RCC are included in this exercise. The authors also provided comparison over different optical water types. They showed that C2RCC and Polymer provided good estimates of the spectral shape and magnitude of R_{rs}.

Limitations of the study:

- The match-ups exercise does not include very turbid waters with SPM exceeding 32.2 $mg.m^{-3}$

- Absorbing aerosols and adjacency effects were not considered

- NASA and NIRSWIR are vicariously calibrated which is not the case for the other AC

- The design of the sensitivity study remains too complex as the dependent variables were not fully isolated resulting in inconclusive interpretation and ambiguous results.

- Sensitivity studies (in-situ and simulations) remain ambiguous

- Detailed transfer of AC performance results to other sensors remains problematic.

Perspectives/recommendations

- Continuous effort to collect more in-situ measurements over a wide range of atmospheric and oceanic conditions. AERONET-OC network is very useful but the diversity of the optical water types should be improved (OWT1-3). Systematic concomitant measurements of R_{rs}, the inherent optical properties and the aerosol parameters should be encouraged.

- Future inter-comparisons experiments should consider including adjacency effects and very absorbing aerosols.

- With the launch of the PACE mission on February 8th, 2024, efforts should be dedicated to use the polarization to better derive R_{rs}. Polarization observations can obtain more optical properties of aerosol scattering which is greatly helpful for improving AC accuracy not only in open oceans but also in turbid waters (He et al., 2024).

- Using lidar technique could help to quantify the highly absorbing aerosols

- Continuous effort to inter-compare AC for a wider range of OC sensors and for new AC

Acknowledgments

The group would like to acknowledge Menghua Wang's input during the initial phase of the WG. We would like to thank François Steinmetz and Chuqun Chen for providing their algorithms. We acknowledge the University of Littoral-Côte d'Opale (ULCO, France) for the funding of the one-year postdoc of Sundarabalan V. Balasubramaniana. The authors would like to thank the PIs of the AERONET-OC stations. This work has been done in the frame of two projects funded by the TOSCA program of CNES. Data were sourced from Australia's Integrated Marine Observing System (IMOS) – IMOS is enabled by the National Collaborative Research Infrastructure Strategy (NCRIS). NCRIS/IMOS and CSIRO are acknowledged for funding the Lucinda Jetty Coastal Observatory. We acknowledge the MODIS mission scientists and associated NASA personnel for the production of the Aqua data used in this report.

References

Ahmad, Z., B. A., Franz, C.R., McClain, E.J., Kwiatkowska, J., Werdell, E.P., Shettle and B. N., Holben (2010). New aerosol models for the retrieval of aerosol optical thickness and normalized water-leaving radiances from the SeaWiFS and MODIS sensors over coastal regions and open oceans, Applied Optics, 49, 5545-5560.

Ahn, J.-H., and Y.-J., Park (2020). Estimating Water Reflectance at Near-Infrared Wavelengths for Turbid Water Atmospheric Correction: A Preliminary Study for GOCI-II, Remote Sensing, 12, https://doi.org/10.3390/rs12223791.

Al Shehhi, M.R., I., Gherboudj, J., Zhao and H., Ghedira (2017). Improved atmospheric correction and chlorophyll-a remote sensing models for turbid waters in a dusty environment, Remote Sensing of Environment, 133, 46-60.

Bai, R., X., He, Y., Bai, T., Li, Q., Zhu and F., Gong (2020), Characteristics of water leaving reflectance at ultraviolet wavelengths: radiative transfer simulations. Optics Express, 28, 29714-29729.

Bai R., He X., Bai Y., Gong F., Zhu Q., Wang D., and Li T. (2023), Atmospheric correction algorithm based on the interpolation of ultraviolet and shortwave infrared bands. Optics Express, 31, 6805-6826.

Bailey, S.W., and P.J., Werdell (2006). A multi-sensor approach for the on-orbit validation of ocean color satellite data products. Remote Sensing of Environment, 102, 12–23.

Bailey, S.W., B.A., Franz and P.J., Werdell (2010). Estimating of near-infrated water-leaving reflectance for satellite ocean color data processing, Optics Express, 18, 7521-7527.

Banerjee, S., and P., Shanmugam (2021). Novel method for reconstruction of hyperspectral resolution images from multispectral data for complex coastal and inland waters., Advances in Space Research, 67, 266–289. https://doi.org/10.1016/j.asr.2020.09.045

Banzon, V.F., H.R., Gordon, C.P., Kuchinke, D., Antoine, K.J., Voss and R.H., Evans (2009). Validation of a SeaWiFS dust-correction methodology in the Mediterranean Sea: Identification of an algorithm-switching criterion, Remote Sensing of Environment, 113, 2689-2700.

Brajard, J., C., Jamet, C., Moulin and S., Thiria (2006). Use of a neurovariational inversion for retrieving oceanic and atmospheric constituents from ocean color imagery: Application to absorbing aerosols, Neural Networks, 19, 178-185.

Brajard, J., R., Santer, M., Crépon and S., Thiria (2012). Atmospheric correction of MERIS data for case-2 waters using a neuro-variational inversion, Remote Sensing of Environment, 126, 51-61.

Bulgarelli, B. and G., Zibordi, G. (2018a). Seasonal Impact of Adjacency Effects on Ocean Color Radiometry at the AAOT Validation Site. IEEE Geoscience and Remote Sensing Letters, 15, 488.

Bulgarelli, B., and G., Zibordi (2018b). On the detectability of adjacency effects in ocean color remote sensing of mid-latitude coastal environments by SeaWiFS, MODIS-A, MERIS, OLCI, OLI and MSI. Remote Sensing of Environment, 209, 423–438.

Bulgarelli, B., G., Zibordi, and F., Mélin (2018). On the minimization of adjacency effects in SeaWiFS primary data products from coastal areas. Optics Express, 26, A709–A728.

Burazerovic, D., R., Heylen, B., Geens, S., Sterckx, P., Scheunders (2013). Detecting the Adjacency Effect in Hyperspectral Imagery With Spectral Unmixing Techniques. IEEE J. Sel. Top. Appl. Earth Obs. Remote. Sens. 6(3), 1070-1078.

Castagna, A., and Q., Vanhellemont (2022). Sensor-agnostic adjacency correction in the frequency domain: application to retrieve water-leaving radiance from small lakes. ESA Living Planet Symposium 2022, abstract.

Carswell, T., M., Costa, R., Young, N., Komick, J., Gower and R., Sweeting (2017). Evaluation of MODIS-Aqua atmospheric correction and chlorophyll products of Western North American coastal waters based on 13 years of data, Remote Sensing, 9, 1063, doi: 10.3390/rs9101063.

Chomko, R.M., and H.R., Gordon (1998). Atmospheric correction of ocean color imagery: use of the Junge power-law aerosol size distribution with variable refractive index to handle aerosol absorption, Applied Optics, 37, 5560-5572.

Chomko, R.M., and H.R., Gordon (2001). Atmospheric correction of ocean color imagery: test of the spectral optimization algorithm with the Sea-viewing Wide Field-of-view Sensor, Applied Optics, 40, 2973-2984.

Chomko, R.M., H.R., Gordon, S., Maritorena and D.A., Siegel (2003). Simultaneous retrieval of oceanic and atmospheric parameters for ocean color imagery by spectral optimization: a validation, Remote Sensing of Environment, 84, 208-220.

Cohen, D., S. Stamnes, T. Tanikawa, E. R. Sommersten, J. J. Stamnes, J. K. Lotsberg, and K. Stamnes, Comparison of discrete ordinate and Monte Carlo simulations of polarized radiative transfer in two coupled slabs with different refractive indices, Opt. Expr., 21, 9592-9614, 2013. DOI:10.1364/OE.21.009592.

Concha, J.A., M., Bracaglia and V.E., Brando (2021). Assessing the influence of different validation protocols on Ocean Colour match-up analyses, Remote Sensing of Environment, 259, https://doi.org/10.1016/j.rse.2021.112415.

Dierssen, H.M., R.A., Vandermeulen, B.B., Branes, A., Castagna, E., Knaeps and Q., Vanhellemont (2022). QWIP: A Quantitative Metric for Quality Control of Aquatic Reflectance Spectral Shape Using the Apparent Visible Wavelength, Frontiers in Remote Sensing, 3, doi: 10.3389/frsen.2022.869611

Doerffer, R., and H., Schiller (2007) The MERIS case 2 water algorithm, International Journal of Remote Sensing, 28, 517-535.

Doerrfer, R. (2015). Algorithm Theoretical Bases Document (ATBD) for L2 processing of MERIS data of case 2 waters, reprocessing. MERIS Case 2 water ATBD 4th reproc, 55 pages.

Dogliotti, A. I., K.G., Ruddick, B., Nechad, D., Doxaran, and E., Knaeps (2015). A single algorithm to retrieve turbidity from remotely- sensed data in all coastal and estuarine waters, Remote Sensing of Environment, 156, 157-168.

Fan, Y., W. Li, C. K. Gatebe, C. Jamet, G. Zibordi, T. Schroeder, and K. Stamnes, Atmospheric correction and aerosol retrieval over coastal waters using multilayer neural networks, Remote Sensing of the Environment, 199, 218-240, 2017.

Fan, Y., S., Li, X., Han and L., Stamnes (2020). Machine learning algorithms for retrievals of aerosol and ocean color products from FY-3D MERSI-II instrument, Journal of Quantitative Spectroscopy & Radiative Transfer, 250, https://doi.org/10.1016/j.jqsrt.2020.10704.

Fan, Y., W., Li, N., Chen, J.-H., Ahn, Y.-J., Park, S., Kratzer, T., Schroeder, J., Ishizaka, R., Chang and K., Stamnes (2021). OC-SMART: A machine learning based data analysis platform for satellite ocean color sensors, Remote Sensing of Environment, 253, https://doi.org/10.1016/j.rse.2020.112236.

Feng, H., D., Vandemark, J.W., Campbell, and B.N., Holben (2008). Evaluation of MODIS ocean color products at a northeast United States coast site near the Martha's Vineyard Coastal Observatory. International of Remote Sensing, 29, 4479–4497.

Feng, L., and C. Hu (2017), Land adjacency effects on MODIS Aqua top-of-atmosphere radiance in the shortwave infrared: Statistical assessment and correction. J. Geophys. Res. Oceans, 122, 4802–4818, doi:10.1002/2017JC012874

Fischer and H. Grassl, “Radiative transfer in an atmosphere–ocean system: An azimuthally dependent matrixoperator approach.” Appl. Opt. **23**, 1035–1039 (1984).

Frouin, R., B., Franz, A., Ibrahim, K., Knobelpiesse, Z., Ahmad, B., Cairns, J., Chowdhary, H.M., Dierssen, J., Tan, O., Dubovik, X., Huang, A.B., Davis, O., Kalashnikova, D.R., Thompson, L.A., Remer, E., Boss, O., Coddington, P.-Y., Deschamps, B.-C., Gao, L., Gross, O., Hasekamp, A., Omar, B., Pelletier, D., Ramon, F., Steinmetz and P.-W., Zhai (2019). Atmospheric correction of satellite ocean-color imagery during the PACE era, Frontiers in Earth Sciences, 7, doi: 10.3380/feart.2019.00145.

Gilerson, A., E., Herrera-Estrella, R., Foster, J., Agagliate, C., Hu, A., Ibrahim and B.A., Franz B (2022). Determining the Primary Sources of Uncertainty in Retrieval of Marine Remote Sensing Reflectance From Satellite Ocean Color Sensors, Frontiers in Remote Sensing, 3, doi: 10.3389/frsen.2022.857530.

Gordon, H.R. (1997). Atmospheric correction of ocean color imagery in the Earth Observing System era, Journal of Geophysical Research, 102, 17081-17106.

Gordon, H.R., and M., Wang (1994). Retrieval of water-leaving radiance and aerosol optical thickness over the ocean with SeaWiFS: a preliminary algorithm, Applied Optics, 443-452.

Gossn, J.I.; K.G., Ruddick, and A.I., Dogliotti (2019) Atmospheric Correction of OLCI Imagery over Extremely Turbid Waters Based on the Red, NIR and 1016 nm Bands and a New Baseline Residual Technique. Remote Sensing, 11, https://doi.org/10.3390/rs11030220.

Gossn, J.I., R., Frouin, A.I., Dogliotti (2019). Atmospheric Correction of Satellite Optical Imagery over the Río de la Plata Highly TurbidWaters Using a SWIR-Based Principal Component Decomposition Technique. Remote Sensing, 13, https://doi.org/10.3390/rs13061050.

Goyens, C., C., Jamet and T., Schroeder (2013). Evaluation of four atmospheric correction algorithms for MODIS-Aqua images over contrasted coastal waters, Remote Sensing of Environment, 131, 63-75.

Hamre, B., S. Stamnes, K. Stamnes, and J.J. Stamnes, A versatile tool for radiative transfer simulations in the coupled atmosphere-ocean system: Introducing AccuRT, Ocean Optics XXII, Portland, ME, 2014.

Han, B., H., Loisel, V., Vantrepotte, X., Mériaux, P., Bryère, S., Ouillon, D., Dessailly, Q., Xing and J., Zhu (2016). Development of a semi-analytical algorithm for the retrieval of suspended particulate matter from remote sensing over clear to very turbid waters, Remote Sensing, 8, doi: 10.3390/rs8030211.

He, Q., and C., Chen (2014). A new approach for atmospheric correction of MODIS imagery in turbid coastal waters: a case study for the Pearl River Estuary. Remote Sens. Lett., 5, 249-257, DOI: 10.1080/2150704X.2014.898192

He, X., D. Pan, and Z. Mao (2004). Atmospheric correction of SeaWiFS imagery for turbid coastal and inland waters. Acta Oceanologica Sinica,23(4), 609-615.

He, X., Y. Bai, D. Pan, J. Tang, and D. Wang (2012). Atmospheric correction of satellite ocean color imagery using the ultraviolet wavelength for highly turbid waters, Opt. Express, 20, 20754–20770.

He, X., T., Pan, Y., Bai, P., Shanmugam, D., Wang, T., Li, and F., Gong (2024). Intelligent atmospheric correction algorithm for polarization ocean color satellite measurements over the open ocean. IEEE Transactions on Geoscience and Remote Sensing, DOI: 10.1109/TGRS.2023.3348159

Heege, T., V., Kiselev, M., Wettle and N., Hung (2014). Operational multi-sensor monitoring of turbidity for the entire Mekong Delta. International Journal of Remote Sensing, 35, 2910. https://doi.org/10.1080/01431161.2014.890300

Hieronymi, M., S., Bi, D., Müller, E.M., Schütt, D., Behr, C., Brockmann, C., Lebreton, F., Steinmetz, K., Stelze and Q., Vanhellemont (2023). Ocean color atmospheric correction methods in view of usability for different optical water types, Frontiers in Marine Science, doi: 10.3389/fmars.2023.1129876

Holben, B., T.F., Eck, I., Slutsker, D., Tanré, J.P., Buis, A., Setzer, E., Vermote, J.A., Reagan, Y.J., Kaufman, T., Nakajima, F., Lavenu, I., Jankowiak and A., Smirnov (1998). AERONET - A federated instrument networks and data archive for aerosol characterization, Remote Sensing of Environment, 66, 1-16.

Hu, C., K.L., Carder and F.E., Muller-Karger (2000). Atmospheric correction of SeaWiFS imagery over turbid coastal waters: a practical method, Remote Sensing of Environment, 74, 195-206.

Ibrahim, A., B.A., Franz, Z., Ahmad and S.W., Bailey (2019). Multiband atmospheric correction algorithm for ocean color retrievals, Frontiers in Earth Science, 7, doi: 10.3389/feart.2019.00116.

Ibrahim, A., B.A., Franz, A.M., Sayer, K., Knobelspiesse, M., Zhang, S.W., Bailey, L.I.W., McKinna, M., Gao and P.J., Werdell (2022). Optail estimation framework for ocean color atmospheric correction and pixel-level uncertainty quantification, Applied Optics, 61, 6453-6475.

IOCCG (2010). Atmospheric Correction for Remotely-Sensed Ocean-Colour Products. Wang, M. (ed.), Reports of the International Ocean-Colour Coordinating Group, No. 10, IOCCG, Dartmouth, Canada.

IOCCG (2019). Uncertainties in Ocean Colour Remote Sensing. (ed. Mélin F.) Dartmouth, NS, Canada, International Ocean-Colour Coordinating Group (IOCCG), 164pp. (Reports of the International Ocean-Colour Coordinating Group, No. 18). http://dx.doi.org/10.25607/OBP-696

Jamet., C., S., Thiria, C., Moulin and M., Crepon (2004). Use of a neurovariational inversion for retrieving oceanic and atmospheric constituents from ocean color imagery: a feasibility study, Journal of Atmospheric and Oceanic Technology, 22, 460-475.

Jamet., C., H., Loisel, C.P., Kuchinke, K., Ruddick, G., Zibordi and H., Feng (2011). Comparison of three SeaWiFS atmospheric correction algorithms for turbid waters using AERONET-OC measurements, Remote Sensing of Environment, 115, 1955-1965.

Jiang, D., J., Scholze, X., Liu, S., Simis, K. , Stelzer, D., Müller, P., Hunter, A., Tyler, and E., Spyrakos (2023). A data-driven approach to flag land-affected signals in satellite derived water quality from small lakes. Int. J. Appl. Earth Obs. Geoinformation, 117, 103188.

Keshava, N. (2004). Distance metrics and band selection in hyperspectral processing with applications to material identification and spectral libraries, IEEE Transactions on Geoscience and Remote Sensing, 42, 1552-1565.

Kiselev, V., B., Bulgarelli, and T., Heege (2015). Sensor independent adjacency correction algorithm for coastal and inland water systems. Remote Sensing of Environment, 157, 85-95.

Knaeps, E., A.I., Dogliotti, D., Raymaekers, K., Ruddick and S., Sterckx (2012). *In situ* evidence of non-zero reflectance in the OLCI 1020 nm band for a turbid estuary, Remote Sensing of Environment, 120, 133-144.

Kohonen, T. (2013). Essentials of the self-organizing map, Neural Networks, 37, 52-65.

Kruse, F., A., Lefkoff, J., Boardman, J., Heidebrecht, A., Shapiro, P., Barloon and A., Goetz (1994). The spectral image processing system -interactive visualization and analysis of imaging spectrometer data, Remote Sensing of Environment, 44, 145-163.

Kuchinke, C.P., H.R., Gordon, L.W., Harding, and K.J., Voss (2009). Spectral optimization for constituent retrieval in case 2 waters: II Implementation and performance, Remote Sensing of Environment, 13, 571-587.

Lavender, S.J., M.H., Penkerton, G.F., Moore, J., Aiken and D., Blondeau-Patissier (2005). Modification to the atmospheric correction of SeaWiFS ocean color images over turbid waters, Continental Shelf Research, 25, 539-555.

Liu, H., S., Hu, Q., Zhou, Q., Li and G., Wu (2019). Revisiting effectiveness of turbidity index for the switching scheme of NIR-SWIR combined ocean color atmospheric correction algorithm, International Journal of Applied Earth Observation and Geoinformation, 76, https://doi.org/10.1016/j.jag.2018.10.010.

Liu, H., X., He, Q., Li, S., Kratzer, J., Wang, T., Shi, Z., Hu, C., Yang, S., Hu, Q., Zhou and G., Wu (2021). Estimating ultraviolet reflectance from visible bands in ocean colour remote sensing, Remote Sensing of Environment, 258, https://doi.org/10.1016/j.rse.2021.112404.

Mao, Z., B., Tao, P., Chen, J., Chen, Z., Hao, Q., Zhu and H., Huang (2020). Atmospheric correction of satellite ocean color remote rensing in the presence of high aerosol loads, 12, https://doi.org/10.3390/rs12010031.

Melin, F. (2022). Validation of ocean color remote sensing reflectance data: Analysis of results at European coastal sites, Remote Sensing of Environment, 280, 113153.

Melin, F., P., Colandrea, P., de Vis and S.E., Hunt (2022). Sensitivity of ocean color atmospheric correction to uncertainties in ancillary data: a global analysis with SeaWiFS data, IEEE Transactions on Geosciences and Remote Sensing, 60, 1-18, doi: 10.1109/TGRS.2022.315040.

Mobley, C.D., J., Werdell, B., Franz, Z., Ahmad and S., Bailey (2016). Atmospheric correction for satellite ocean color radiometry - A tutorial and documentation of the algorithms used by the NASA Ocean Biology Processing Group, NASA report, 80 pages.

Moore, G.F., J., Aiken, and S.J., Lavender (1999). The atmospheric correction of water color and the quantitative retrieval of suspend particulate matter in case II waters: Application to MERIS, International Journal of Remote Sensing, 20, 1713-1733.

Moore, T.S., J.W., Campbell ad H., Feng (2015). Characterizing the uncertainties in spectral remote sensing reflectance for SeaWiFS and MODIS-Aqua based on global in situ matchup data sets, Remote Sensing of Environment, 159, 14-27.

Moulin, C., H.R., Gordon, V.F., Banzon and R.H., Evans (2001a). Assessment of Saharan dust absorption in the visible from SeaWiFS imagery, Journal of Geophysical Research, 106, 18239-18249.

Moulin, C., H.R., Moulin, R.M., Chomko, V.F., Banzon and R.H., Evans (2001b). Atmospheric correction of ocean color imagery through thick layers of Saharan dust, Geophysical Research Letters, 28, 5-8.

Müller, D., J., Krasemann, R.J., Brewin, C., Brockmann, P.-Y., Deschamps, R., Doerffer, N., Fomferra, B.A., Franz, M.G., Grant, S.B., Groom, F. Mélin, T., Platt, P., Regner, S., Sathyendranath, F., Steinmetz and J., Swinton (2015). The Ocean Colour Climate Initiative: I. A methodology for assessing atmospheric correction processors based on in-situ measurements, Remote Sensing of Environnment, 162, 242-256.

Nobileau, D., and D., Antoine (2005). Detection a blue-absorbing aerosols using near infrared and visible (ocean color) remote sensing observations, Remote Sensing of Environment, 95, 368-387.

Oo, M., M., Vargas, A., Gilerson, B., Gross, F., Moshary and S., Ahmed (2008). Improving atmospheric correction for highly productive coastal waters using the shortwave infrared retrieval algorithm with water-leaving reflectance constraints at 412 nm, Applied Optics, 2008, 47, 3846-3859.

O'Reilly, J.E., S., Maritonera, B.G., Mitchell, D.A., Siegel, K.L., Carder, S.A., Garver, M., Kahru and C., McClain (1998). Ocean color chlorophyll algorithms for SeaWiFS, Journal of Geophysical Research, 103, 24,937-24,953.

O'Reilly, J.E., and P.J., Werdell (2019). Chlorophyll algorithms for ocean color sensors -OC4, OC5 & OC6, Remote Sensing of Environment, 229, 32-47.

Park, Y.-J. and K., Ruddick (2005). Model of remote-sensing reflectance including bidirectional effects for case 1 and case 2 waters. Applied Optics, 44 , 1236-1249

Pahlevan, N., A., Mangin, S.V., Balasubramian, B., Smith, K., Alikas, K., Arai, C., Barbosa, S., Bélanger et al. (2021). ACIX-Aqua: A global assessment of atmospheric correction methods for Landsat-8 and Sentinel-2 over lakes, rivers, and coastal waters. Remote Sensing of Environment, 258, https://doi.org/10.1016/j.rse.2021.112366Qiao, F., J., Chen, Z., Mao, B., Han, Q., Song, Y., Xu, Q., Zhu (2021). Novel Framework of Integrating UV and NIR Atmospheric Correction Algorithms for Coastal Ocean Color Remote Sensing. Remote Sensing, 13, https://doi.org/10.3390/rs13214206

Qiao, F., J., Chen, Z., Mao, B., Han, Q., Song, Y., Xu, and Q.A., Zhu (2021). Novel Framework of Integrating UV and NIR Atmospheric Correction Algorithms for Coastal Ocean Color Remote Sensing. Remote Sensing, 13, https://doi.org/10.3390/rs13214206

Robinson, W.D., B.A., Franz, F.S., Patt, S.W., Bailey, and P.J., Werdell (2003). Masks and flags updates. In S. B. Hooker, & E. R. Firestone (Eds.), SeaWiFS Postlaunch Technical Report Series, Chap.6, NASA/TM-2003-206892. Greenbelt, Maryland, NASA Goddard Space Flight Center volume 22, 34–40.

Ruddick, K., F., Ovidio, and M., Rijkeboer (2000). Atmospheric correction of SeaWiFS imagery for turbid coastal and inland waters. Applied Optics, 39, 897–912.

Ruddick, K.G., V., De Cauwer, Y.-J., Park, and G., Moore (2006). Seaborne measurements of near infrared water-leaving reflectance: The similarity spectrum for turbid waters. Limnology and Oceanography, 51, 1167. https://doi.org/10.4319/lo.2006.51.2.1167

Ruddick, K.G. and the COASTCOLOUR team (2010). DUE CoastColour Round Robin Protocol v1.2, 27 pages.

Santer, R., and C., Schmechtig (2000). Adjacency effects of water surfaces: primary scattering approximation and sensitivity study. Applied Optics, 39(3), 361-375.

Santer, R., and F., Zagolski (2009). Improved Contrast between Ocean and Land (ICOL) algorithm theoretical basis document. Tech. Rep. Université du Littoral Côte d'Opale, Wimereux, France, 15 p.

Sanwlani, N., P., Chauhan and R.R., Navalgung (2014). Atmospheric correction based on inherent optical properties of sea water at NIR wavelengths combined with an automated aerosol spectra determination (ASD) technique, International Journal of Remote Sensing, 35, 3631-3650.

Schroeder, T., Fischer, J., Schaale, M., & Fell, F. (2003). Artificial-neural-network-based atmospheric correction algorithm: application to MERIS data. Proc.SPIE 4892, Ocean Remote Sensing and Applications. https://doi.org/10.1117/12.467293

Schroeder, T. (2005). Fernerkundung von Wasserinhaltsstoffen in Küstengewässern mit MERIS unter Anwendung expliziter und impliziter Atmosphärenkorrekturverfahren (Remote sensing of coastal waters with MERIS on basis of explicit and implicit atmospheric correction algorithms), Doctoral Dissertation, Freie Universität Berlin]. https://doi.org/10.17169/refubium-11210

Schroeder, T., I. Behnert, M. Schaale, J. Fischer, and R. Doerffer (2007). Atmospheric correction algorithm for MERIS above case-2 water, International Journal of Remote Sensing, 28, 1469-1486.

Schroeder, T., M., Schaale, J., Lovell and D., Blondeau-Patissier (2022). An ensemble neural network atmospheric correction for Sentinel-3 OLCI over coastal waters providing inherent model uncertainty estimation and sensor noise propagation, Remote Sensing of Environment, 270, https://doi.org/10.1016/j.rse.2021.112848.

Shi, W., and M., Wang (2007). Detection of turbid waters and absorbing aerosols for the MODIS ocean color data processing, Remote Sensing of Environment, 110, 149-161.

Shi, C., and T., Nakajima (2018). Simultaneous determination of aerosol optical thickness and water-leaving radiance from multispectral measurements in coastal waters, Atmospheric Chemistry and Physics, 18, 3865-3884.

Siegel, D.A., M., Wang, S., Maritorena and W., Robinson (2000). Atmospheric correction of satellite ocean color imagery: the black pixel assumption, Applied Optics, 39, 3582-3591.

Singh, R.K., Shanmugam, P., 2014. A novel method for estimation of aerosol radiance and its extrapolation in the atmospheric correction of satellite data over optically complex oceanic waters. Remote Sens. Environ. 142, 188–206. https://doi.org/10.1016/j.rse.2013.12.001.

Sing; R.K., P., Shanmugam, X., He and T., Schroeder (2019). UV-NIR approach with non-zero water-leaving radiance approximation for atmospheric correction of satellite imagery in inland and coastal zones, Optics Express, 27, A1118-A1145, https://doi.org/10.1364/OE.27.0A1118.

Song, Z., He, X., Bai, Y., Wang, D., Hao, Z., Gong, F., Zhu, Q. (2020). Changes and predictions of vertical distributions of global light-absorbing aerosols based on CALIPSO observation. Remote Sens. 12 (18), 3014.

Song, Z., He, X., Bai, Y., Wang, D., Gong, F., Zhu, Q., Li, T., Li, H. (2022). Effect of the vertical distribution of absorbing aerosols on the atmospheric correction for satellite ocean color remote sensing. IEEE Transactions on Geosciences and Remote Sensing. 60, 1–12.

Song, Z., X. He, Y. Bai, X. Dong, D. Wang, T. Li, Q. Zhu, and F. Gong (2023). Atmospheric correction of absorbing aerosols for satellite ocean color remote sensing over coastal waters. Remote Sensing of Environment, 290, 113552.

Ssenyonga, T., Ø, Frette, B., Hamre, K., Stamnes, D., Muyimbwa, N., Ssebiyonga, and J.J, Stamnes (2021). A New Algorithm for Simultaneous Retrieval of Aerosols and Marine Parameters. Algorithms, 15, https://doi.org/10.3390/a15010004

Stamnes, K., W., Li, B., Yan, H., Eide, A., Barnard, W.S., Pegau and J.J., Stamnes (2003). Accurate and self-consistent ocean color algorithm: simultaneous retrieval of aerosol optical properties and chlorophyll concentrations, Applied Optics, 42, 939-951.

Stamnes, K., G.E., Thomas, and J.J., Stamnes (2017). Radiative Transfer in the Atmosphere and Ocean, Cambridge University Press, second edition.

Stamnes, K., B., Hamre, S., Stamnes, N., Chen, Y., Fan, W., Li, Z., Lin, and J. J., Stamnes (2018). Progress in forward-inverse modeling based on radiative transfer tools for coupled atmosphere-snow/ice-ocean systems: A review and description of the AccuRT model, Applied Sciences, 8, 2682, 2018.

Steinmetz, F.; Deschamps, P.-Y. & Ramon, D. Atmospheric correction in presence of sun glint: application to MERIS. Optics Express, Optical Society of America, 2011, 19, 9783-9800.

Stumpf, R.P., R.A., Arnone, R.W., Gould, P., Martinolich and V., Ransibrahmanakul (2003). Algorithm updates for the fourth SeaWiFS data reprocessing, Eds. S.B., Hooker, in SeaWiFS Postlaunch Technical Report Series, NASA Technical Memorandum 2003-206892, 51-59.

Sterckx, S., R., Knaeps, K., Ruddick (2011). Detection and correction of adjacency effects in hyperspectral airborne data of coastal and inland waters: the use of the near infrared similarity spectrum. International Journal of Remote Sensing, 32(21), 6479-6505.

Sterckx, S., E., Knaeps, S., Kratzer, and K., Ruddick (2015). SIMilarity Environment Correction (SIMEC) applied to MERIS data over inland and coastal waters. Remote Sensing of Environment, 157, 96-110.

Van der Zande, D., Q., Vanhellemont, and K., Ruddick (2016). Validation of Landsat-8/OLI for ocean colour applications with AERONET-OC sites in Belgian coastal waters, Proceedings of the 2016 Ocean Optics Conference, Victoria, BC, Canada, 23-28 October 2016.

Vanhellemont, Q., K., Ruddick (2021). Atmospheric correction of Sentinel-3/OLCI data for mapping of suspended particulate matter and chlorophyll-a concentration in Belgian turbid coastal waters, Remote Sensing of Environment, 256, 112284.

Wang, M. (2007). Remote sensing of the ocean contributions from ultraviolet to near-infrared using the shortwave infrared bands: simulations, Applied Optics, 46, 1535-1547.

Wang, M., and W., Shi (2005). Estimation of the ocean contribution at the MODIS near-infrared wavelengths along the east coast of the U.S.: Two case studies, Geophysical Research Letters, 32, doi: 13160.11029/12005GL022917.

Wang, M., and W., Shi (2007). The NIR-SWIR combined atmospheric correction approach for MODIS ocean color data processing, Optics Express, 15, 15722-15733.

Wang, M., and W., Shi 2012). Sensor noise effects of the SWIR bands on MODIS-derived ocean color products, IEEE Transactions on Geoscience and Remote Sensing, 50, 3280-3292.

Wang, M., and L. Jiang (2018). Atmospheric correction using the information from the short blue band, IEEE Transactions on Geoscience and Remote Sensing, 56, 6224-6237.

Wang, M., J., Tang, and W., Shi (2007). MODIS-derived ocean color products along the Chine east coastal region, Geophysical Research Letters, 34, doi: 06610.01029/02006GL028599.

Wang, Y., Z.-P., Lee, L., Wei, S., Shang, M., Wang and W., Lai (2021). Extending satellite ocean color remote sensing to the near-bleu ultraviolet bands, Remote Sensing of Environment, 253, https://doi.org/10.1016/j.rse.2020.112228.

Wang, J., Y., Wang, Z.-P., Lee, D., Wang, S., Chen and W., Lai (2022). A revision of NASA SeaDAS atmospheric correction algorithm over turbid waters with artificial Neural Networks estimated remote-sensing reflectance in the near-infrared, Remote Sensing of Environment, 194, 235-249.

Wei, J., Z.P., Lee and S., Shang (2016). A system to measure the data quality of spectral remote-sensing reflectance of aquatic environments, Journal of Geophysical Research, 121, 8189-8207, doi: 10.1002/2016JC012126.

Werdell, P.J., B.A., Franz and S.W. Bailey (2010). Evaluation of shortwave infrared atmospheric correction for ocean color remote sensing of Chesapeake Bay, Remote Sensing of Environment, 114, 2238-2247.

Xue, C., S., Chen, Z.-P., Lee, L., Hu, X., Shi, M., Lin, J., Liu, C., Ma, Q., Song and T., Zhang (2021). Iterative near-infrared atmospheric correction scheme for global coastal waters, ISPRS Journal of Photogrammetry and Remote Sensing, 179, 92-107, https://doi.org/10.1016/j.isprsjprs.2021.07.005.

Zhang, M., C., Hu, J., Cannizzaro, D., English, B.B., Barnes, P., Carlson and L., Yarbro (2018). Comparison of two atmospheric correction approaches applied to MODIS measurements over North American waters, Remote Sensing of Environment, 216, 442-455.

Zibordi, G., B., Holben, F., Mélin, J.-F., Berthon, I., Slutsker, D., Giles, D., Vandemark, G., Feng, K., Rutledge, G., Schuster, A., Al Mandoos (2006). A network for standardized ocean color validation measurements, EOS Transaction AGU, 87, 293-304.

Zibordi, G., Berthon, J. -F., Mélin, F., D'Alimonte, D., & Kaitala, S. (2009a). Validation of satellite ocean color primary producs at optically complex coastal sites: Northern Adriatic Sea, Northern Baltic Proper and Gulf of Finland. Remote Sensing of Environment, 113, 2574–2591.

Zibordi, G., B., Holben, I., Slutsker, D., Giles, D., D'Alimonte, F., Mélin, J.-F., Berthon, D., Vandemark, H., Feng, G., Schuster, B.E., Fabbri, S., Kaitala and J., Sepala (2009b). Aeronet-oc: A network for the validation of ocean color primary products. Journal of the Atmospheric and Oceanic Technology, 26, 1634–1651.

Zibordi, G., F., Mélin, J.-F., Berthon and M., Talone (2015). In situ autonomous optical radiometry measurements for satellite ocean color validation in the Western Black Sea, Ocean Science, 11, 275-286.

Zibordi, G., B. N., Holben, M., Talone, D., D'Alimonte, I., Slutsker, D.M., Giles, and M.G., Sorokin (2021). Advances in the Ocean Color Component of the Aerosol Robotic Network (AERONET-OC), Journal of Atmospheric and Oceanic Technology, 38(4), 725-746.

Zhang, M., C., Hu and B.B., Barnes (2019). Performance of POLYMER Atmospheric Correction of Ocean Color Imagery in the Presence of Absorbing Aerosols, IEEE Transactions on Geoscience and Remote Sensing, 57, 6666-6674, doi: 10.1109/TGRS.2019.2907884.

Appendix I: Individual scatterplot on the individual match-ups dataset

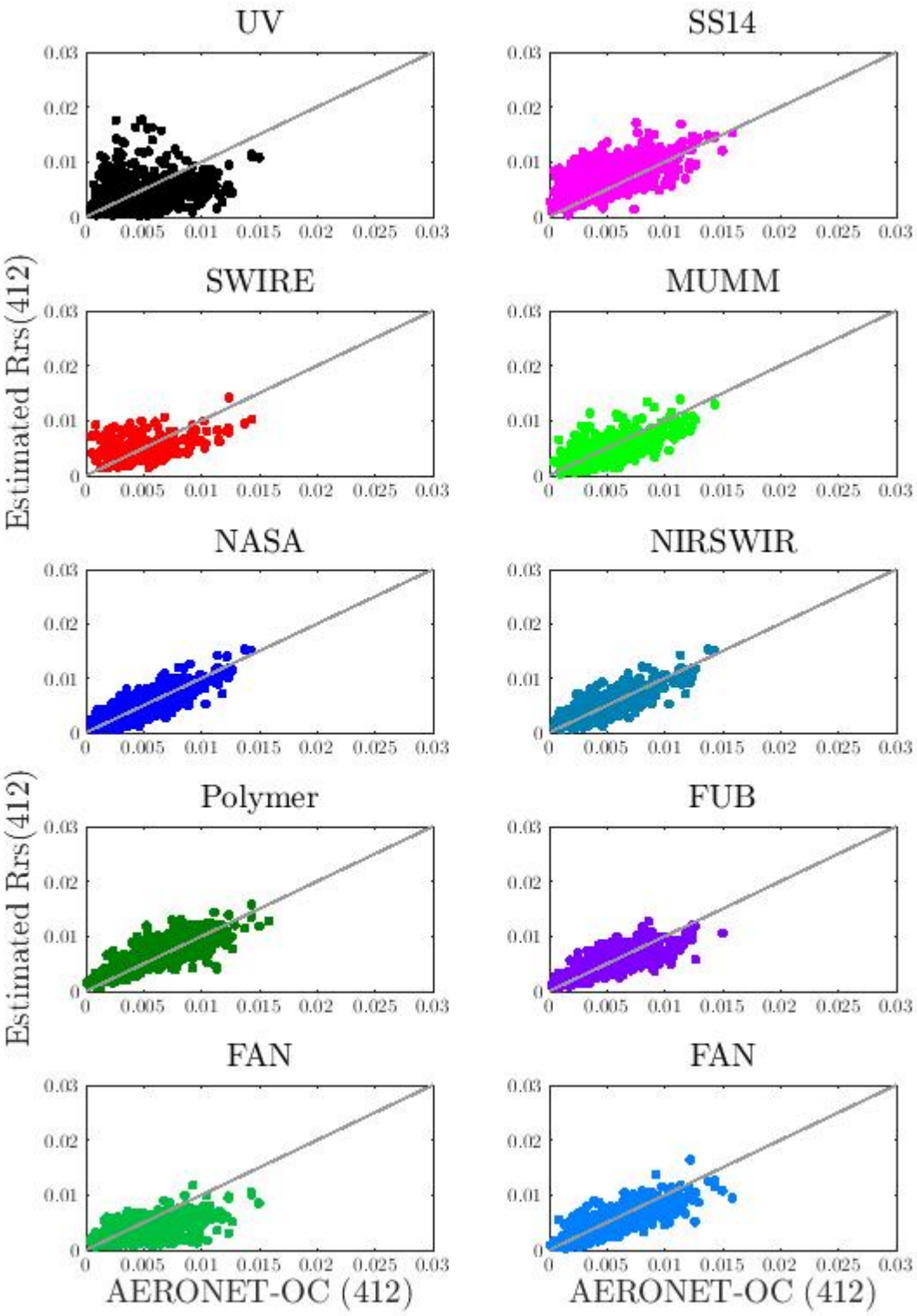
UV
SS14
SWIRE
MUMM
NASA
NIRSWIR
Polymer
FUB
FAN
FAN
Estimated Rrs(412)
Estimated Rrs(412)
AERONET-OC (412)
AERONET-OC (412)
0
0.005
0.01
0.015
0.02
0.025
0.03

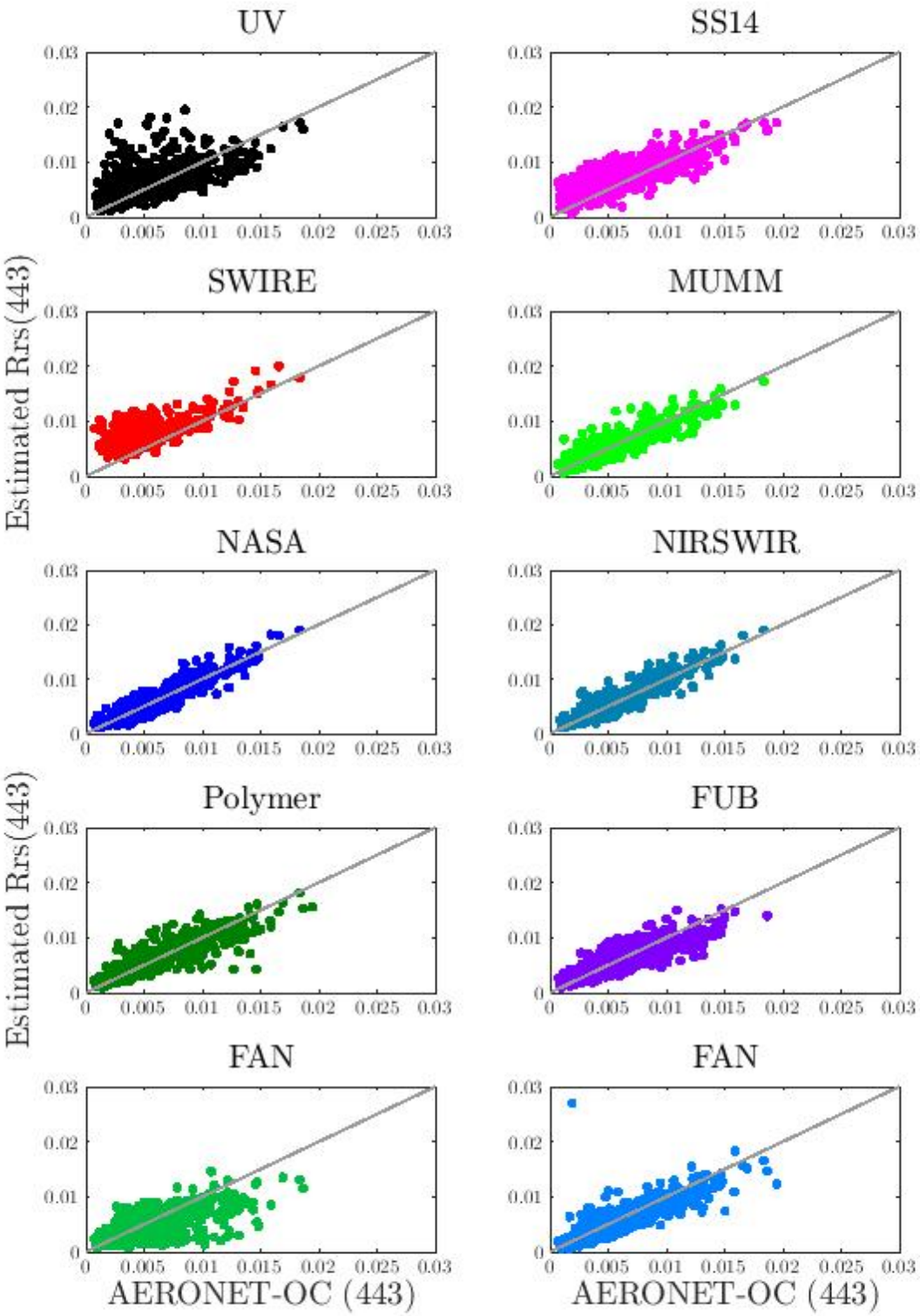
UV
SS14
SWIRE
MUMM
NASA
NIRSWIR
Polymer
FUB
FAN
FAN
Estimated Rrs(443)
Estimated Rrs(443)
AERONET-OC (443)
AERONET-OC (443)
0
0.005
0.01
0.015
0.02
0.025
0.03

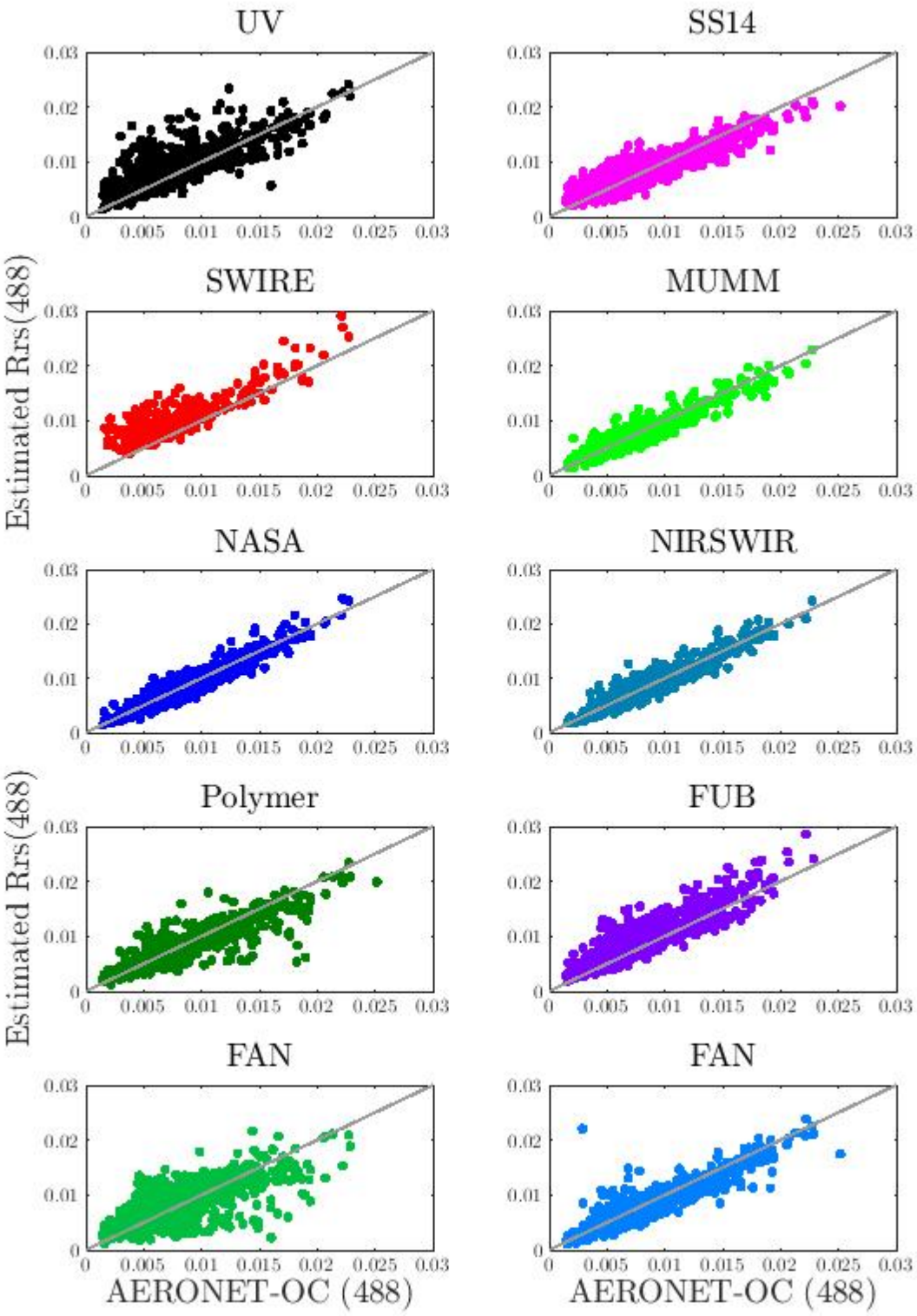
UV
SS14
SWIRE
MUMM
NASA
NIRSWIR
Polymer
FUB
FAN
FAN
Estimated Rrs(488)
Estimated Rrs(488)
AERONET-OC (488)
AERONET-OC (488)
0
0.005
0.01
0.015
0.02
0.025
0.03

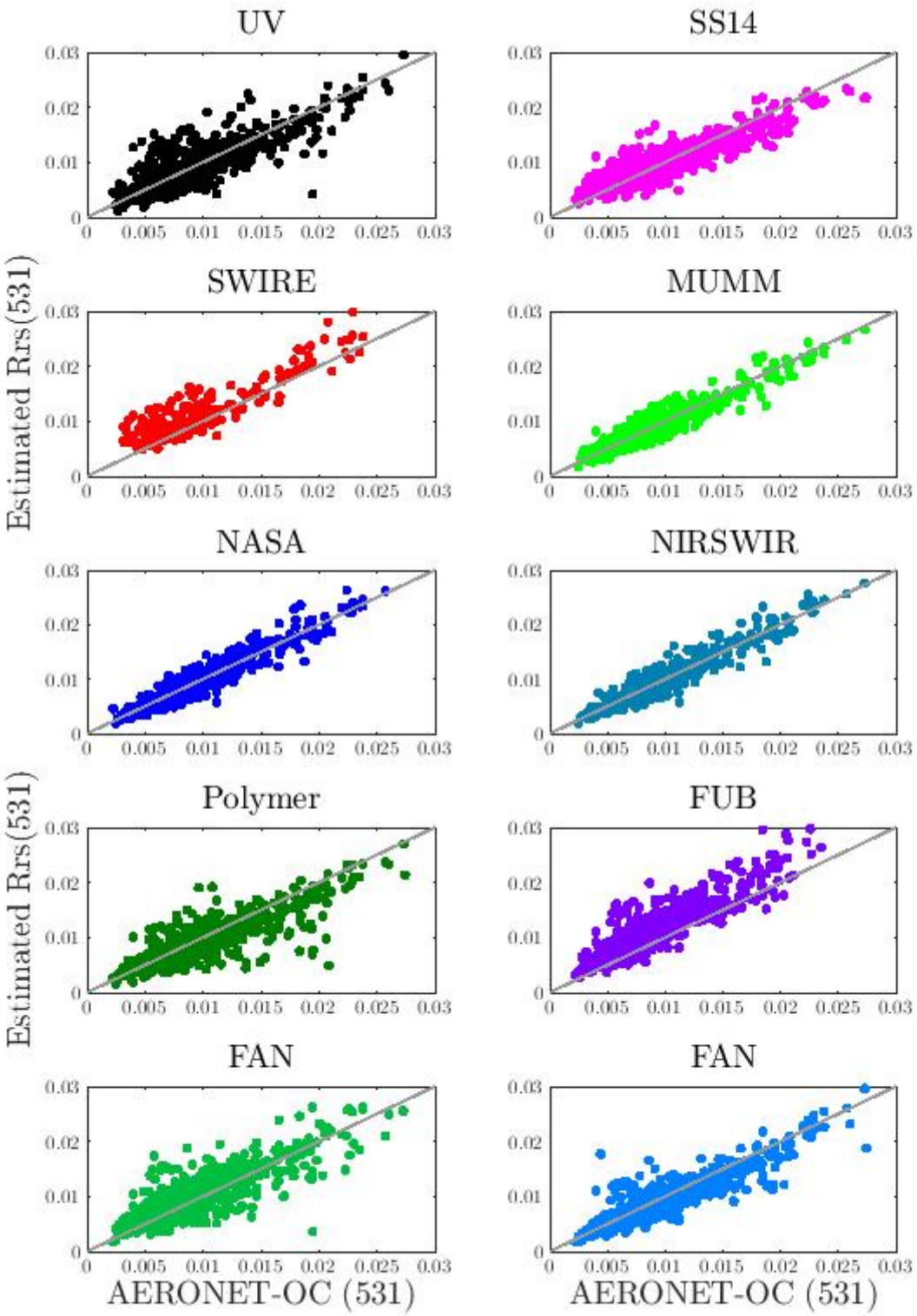
UV
SS14
SWIRE
MUMM
NASA
NIRSWIR
Polymer
FUB
FAN
FAN
Estimated Rrs(531)
Estimated Rrs(531)
AERONET-OC (531)
AERONET-OC (531)
0
0.005
0.01
0.015
0.02
0.025
0.03

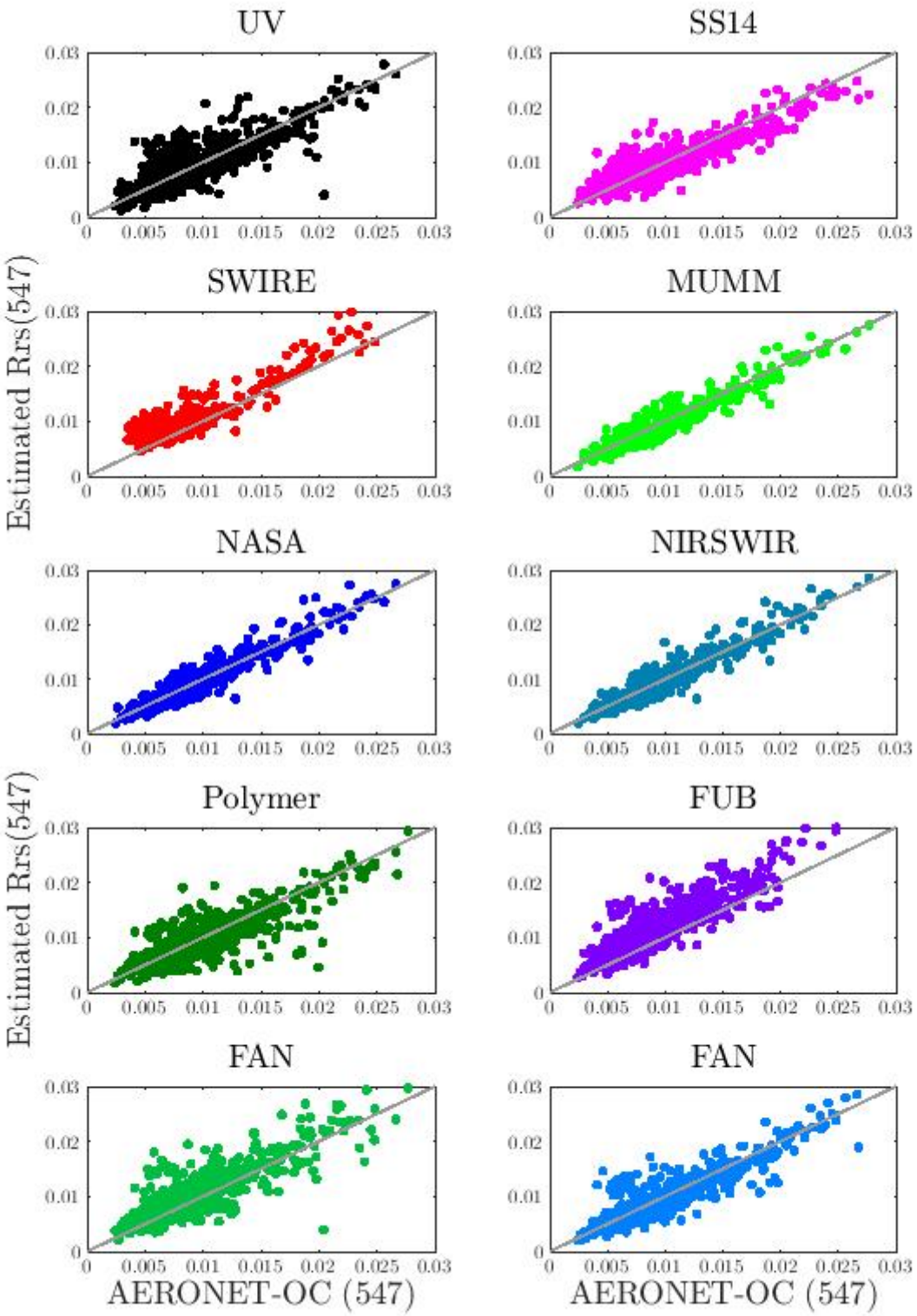
UV
SS14
SWIRE
MUMM
NASA
NIRSWIR
Polymer
FUB
FAN
FAN
Estimated Rrs(547)
Estimated Rrs(547)
AERONET-OC (547)
AERONET-OC (547)
0
0.005
0.01
0.015
0.02
0.025
0.03

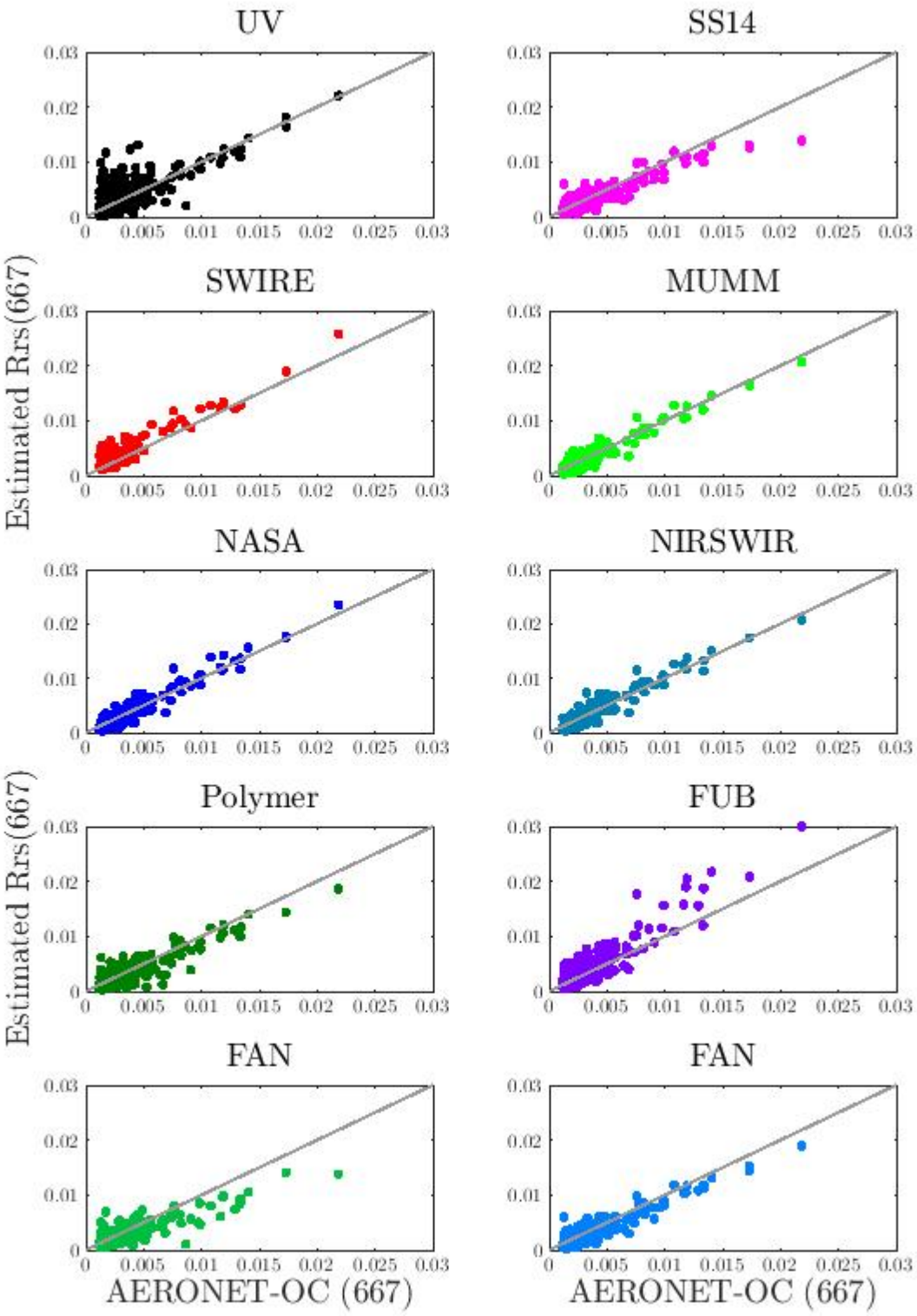
UV
SS14
SWIRE
MUMM
NASA
NIRSWIR
Polymer
FUB
FAN
FAN
Estimated Rrs(667)
Estimated Rrs(667)
AERONET-OC (667)
AERONET-OC (667)
0
0.005
0.01
0.015
0.02
0.025
0.03

Appendix II: Individual scatterplot on the common match-ups dataset

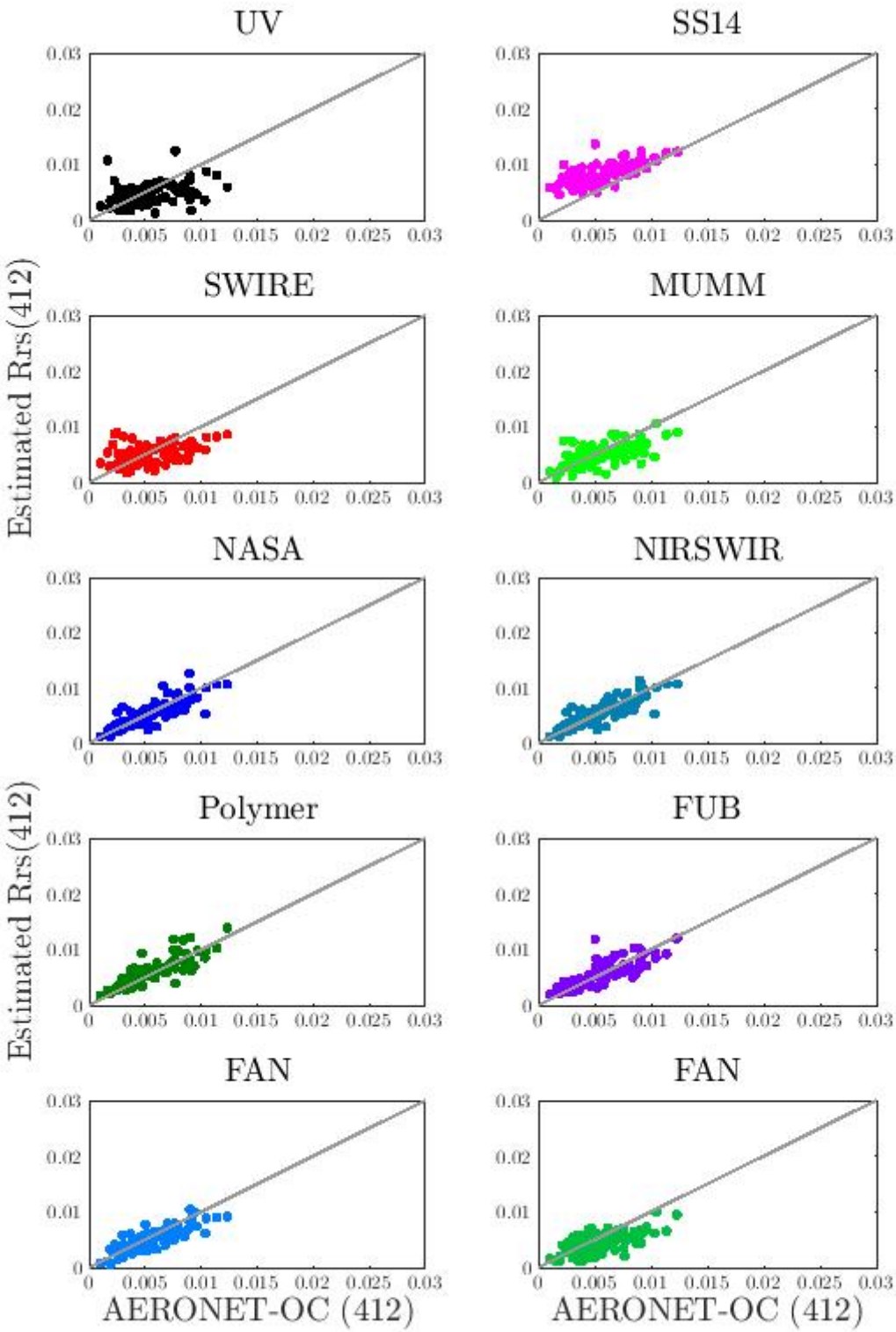
UV
SS14
SWIRE
MUMM
NASA
NIRSWIR
Polymer
FUB
FAN
FAN
Estimated Rrs(412)
Estimated Rrs(412)
AERONET-OC (412)
AERONET-OC (412)
0
0.005
0.01
0.015
0.02
0.025
0.03

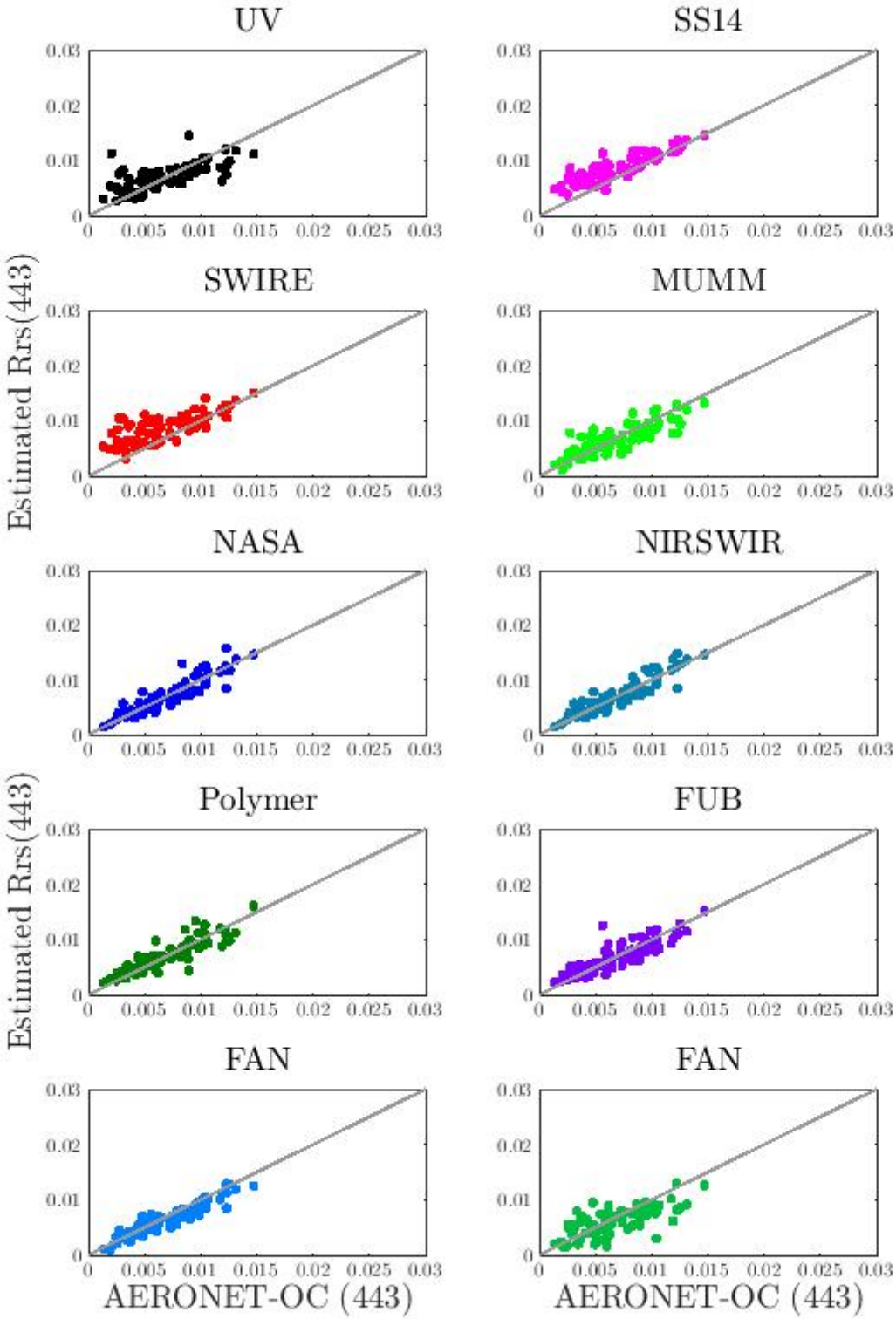
UV
SS14
SWIRE
MUMM
NASA
NIRSWIR
Polymer
FUB
FAN
FAN
Estimated Rrs(443)
Estimated Rrs(443)
AERONET-OC (443)
AERONET-OC (443)
0
0.005
0.01
0.015
0.02
0.025
0.03

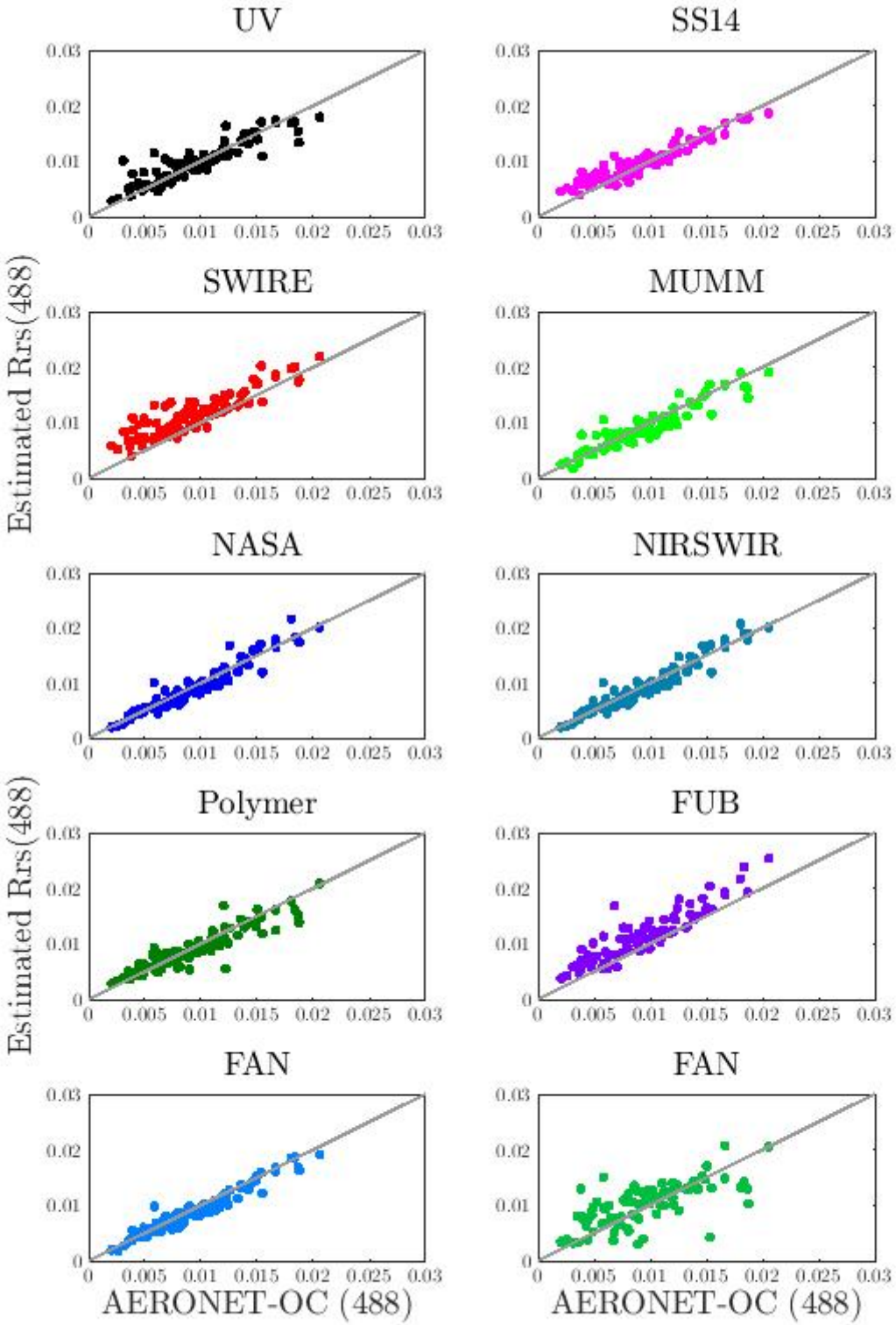
UV
SS14
SWIRE
MUMM
NASA
NIRSWIR
Polymer
FUB
FAN
FAN
Estimated Rrs(488)
Estimated Rrs(488)
AERONET-OC (488)
AERONET-OC (488)
0
0.005
0.01
0.015
0.02
0.025
0.03

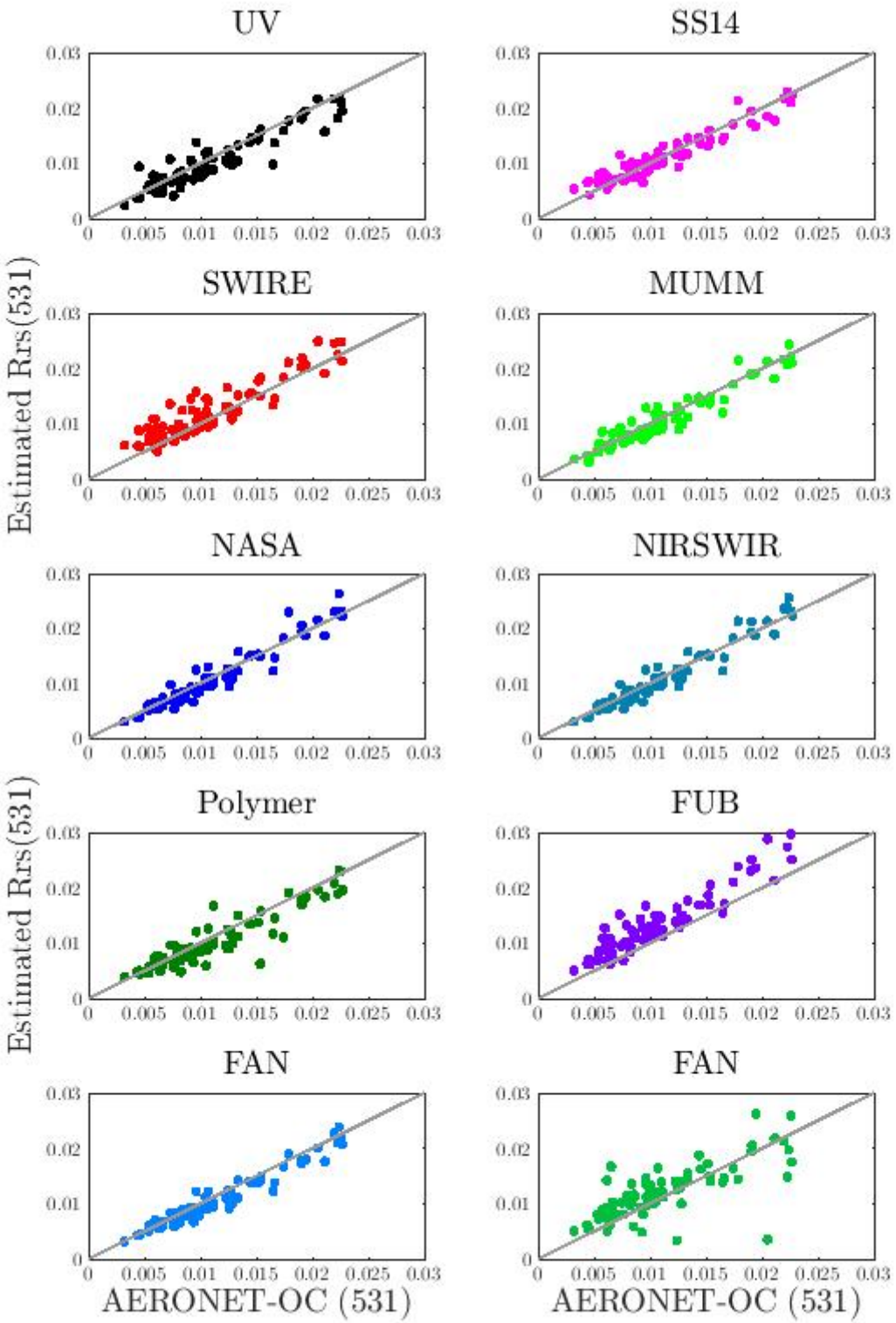
UV
SS14
SWIRE
MUMM
NASA
NIRSWIR
Polymer
FUB
FAN
FAN
Estimated Rrs(531)
Estimated Rrs(531)
AERONET-OC (531)
AERONET-OC (531)
0
0.005
0.01
0.015
0.02
0.025
0.03

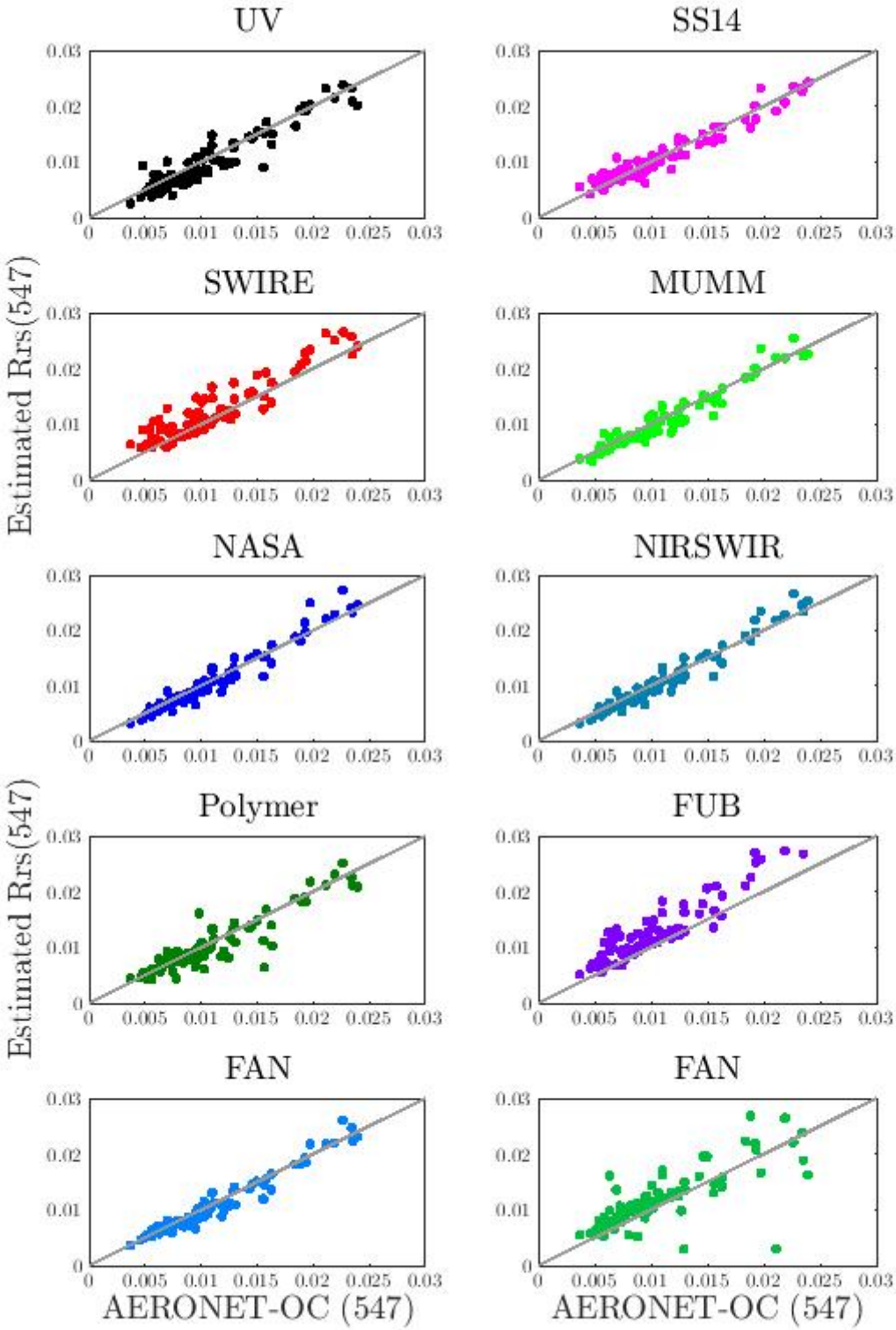
UV
SS14
SWIRE
MUMM
NASA
NIRSWIR
Polymer
FUB
FAN
FAN
Estimated Rrs(547)
Estimated Rrs(547)
AERONET-OC (547)
AERONET-OC (547)
0
0.005
0.01
0.015
0.02
0.025
0.03

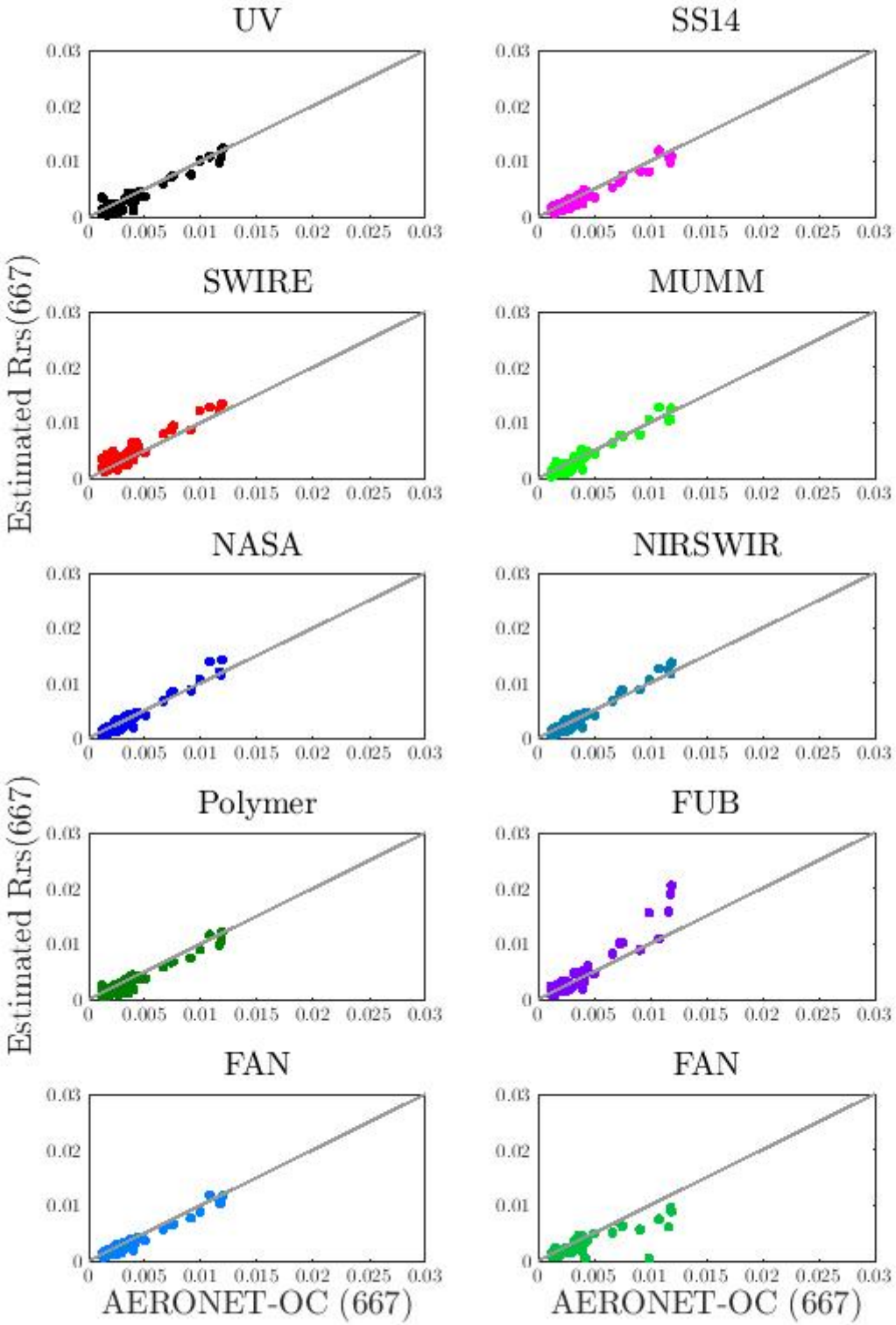
UV
SS14
SWIRE
MUMM
NASA
NIRSWIR
Polymer
FUB
FAN
FAN
Estimated Rrs(667)
Estimated Rrs(667)
AERONET-OC (667)
AERONET-OC (667)
0
0.005
0.01
0.015
0.02
0.025
0.03

Appendix III: Individual scatterplot on the simulated dataset

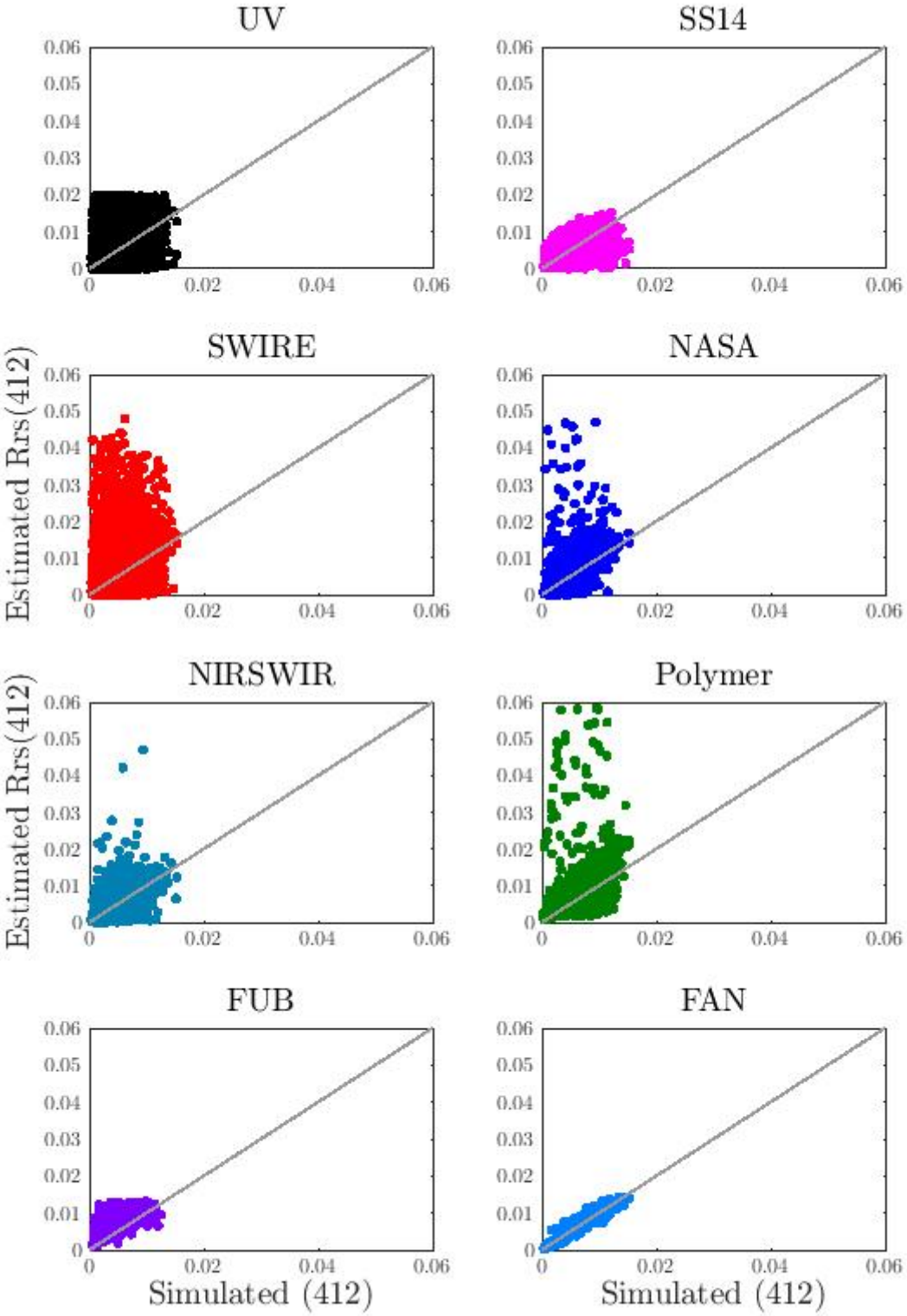
UV
SS14
SWIRE
NASA
NIRSWIR
Polymer
FUB
FAN
Estimated Rrs(412)
Estimated Rrs(412)
Simulated (412)
Simulated (412)
0
0.01
0.02
0.03
0.04
0.05
0.06

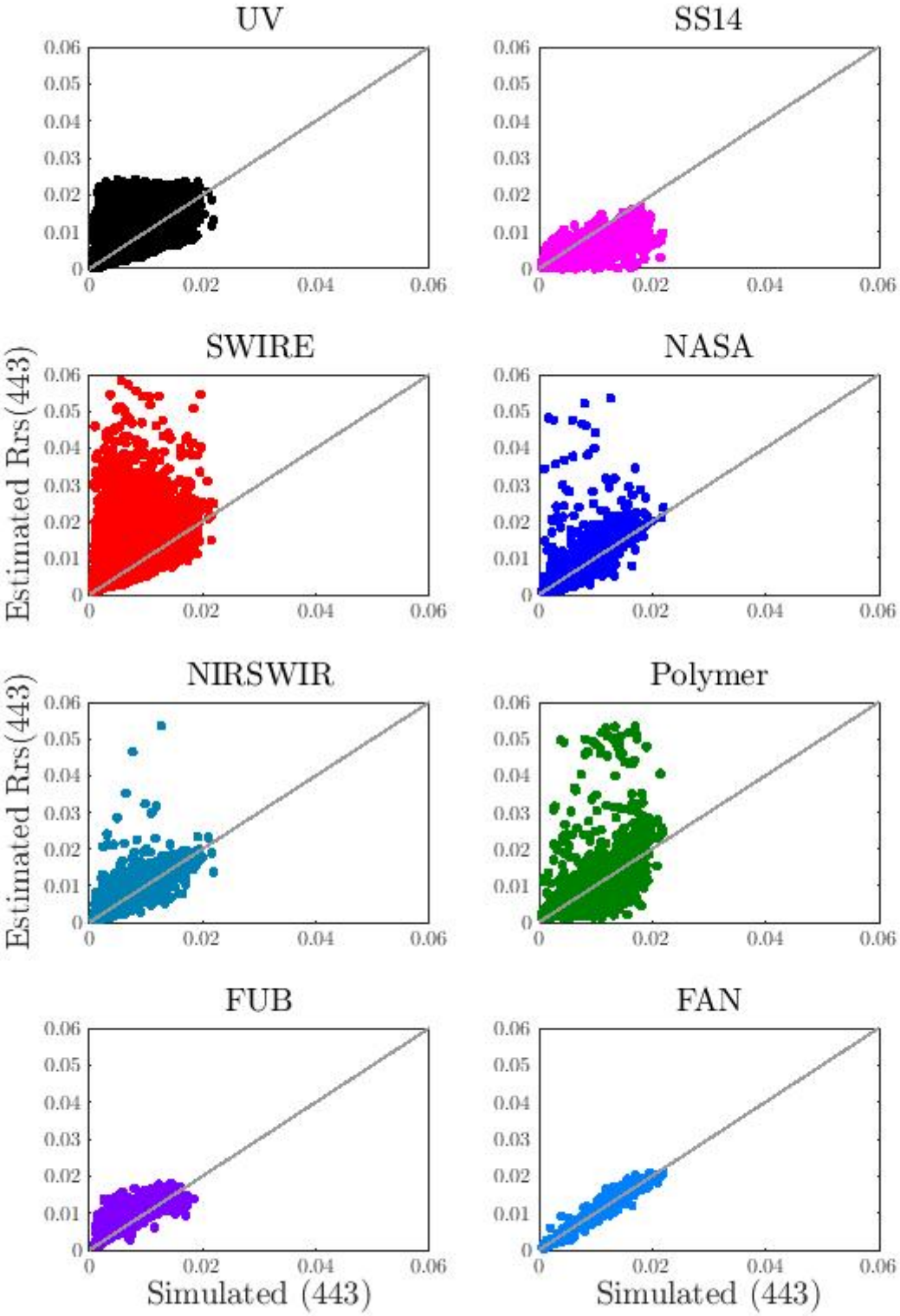
UV
SS14
SWIRE
NASA
NIRSWIR
Polymer
FUB
FAN
Estimated Rrs(443)
Estimated Rrs(443)
Simulated (443)
Simulated (443)
0
0.01
0.02
0.03
0.04
0.05
0.06

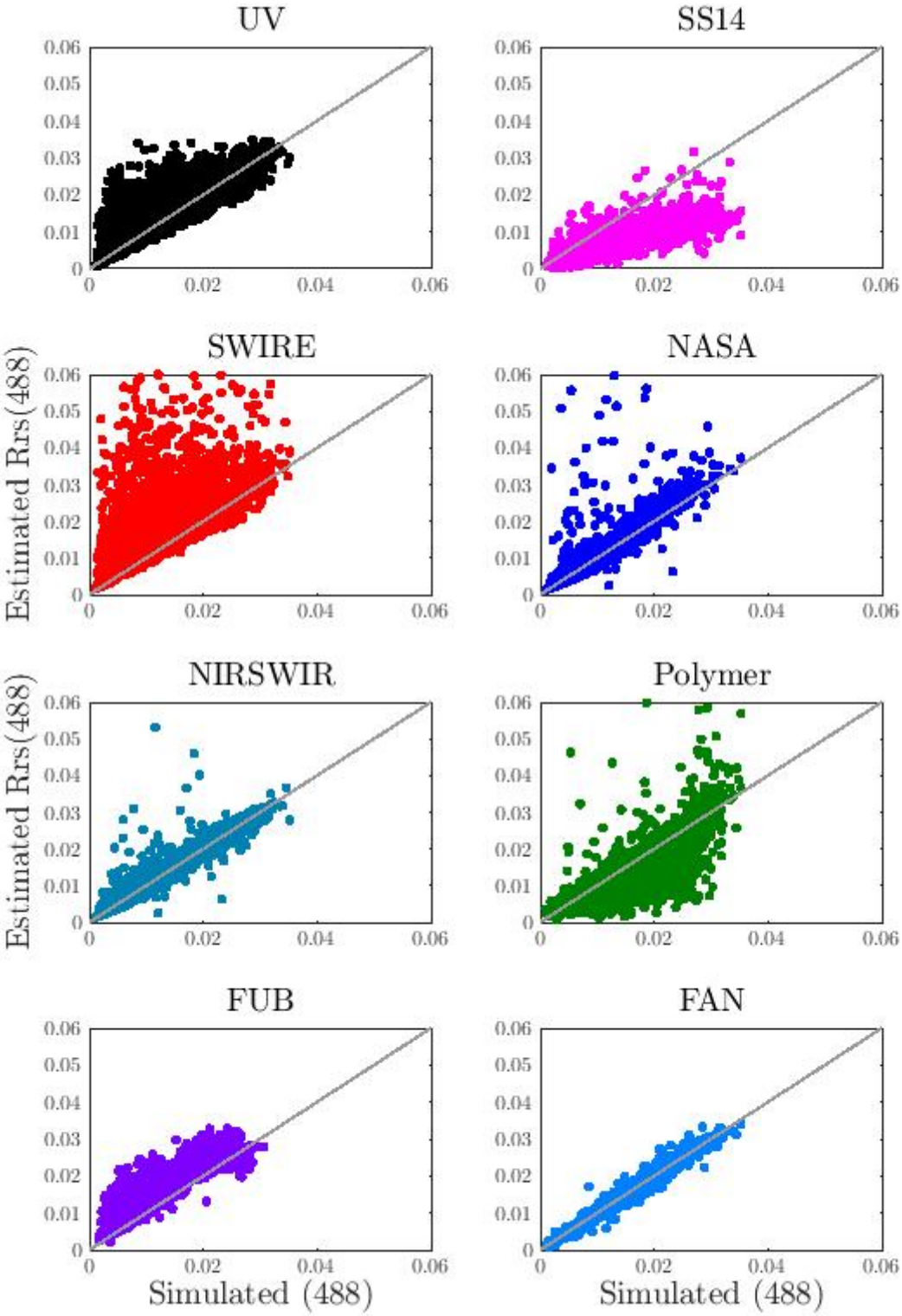
UV
SS14
SWIRE
NASA
NIRSWIR
Polymer
FUB
FAN
Estimated Rrs(488)
Estimated Rrs(488)
Simulated (488)
Simulated (488)
0
0.01
0.02
0.03
0.04
0.05
0.06

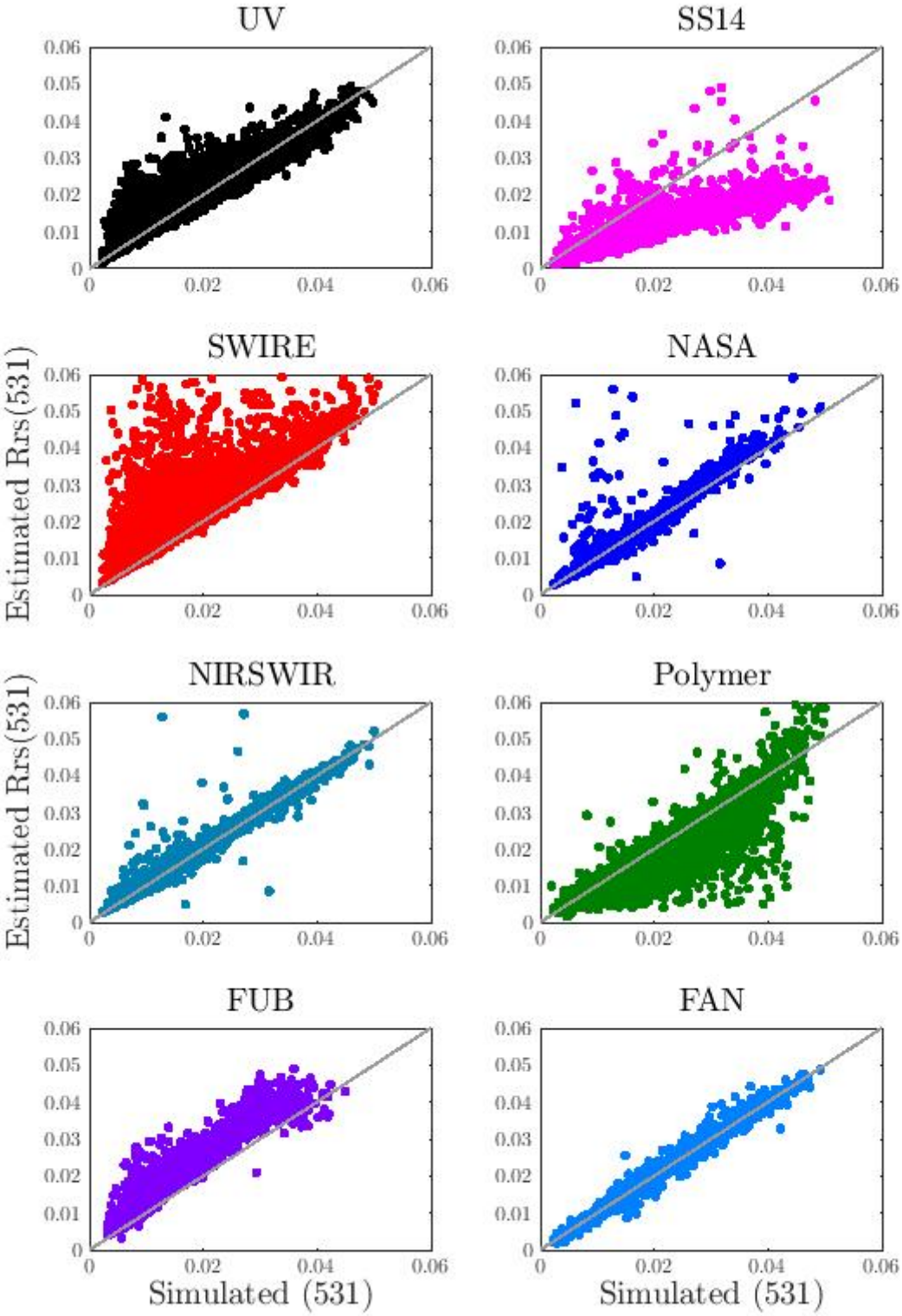
UV
SS14
SWIRE
NASA
NIRSWIR
Polymer
FUB
FAN
Estimated Rrs(531)
Estimated Rrs(531)
Simulated (531)
Simulated (531)
0
0.01
0.02
0.03
0.04
0.05
0.06

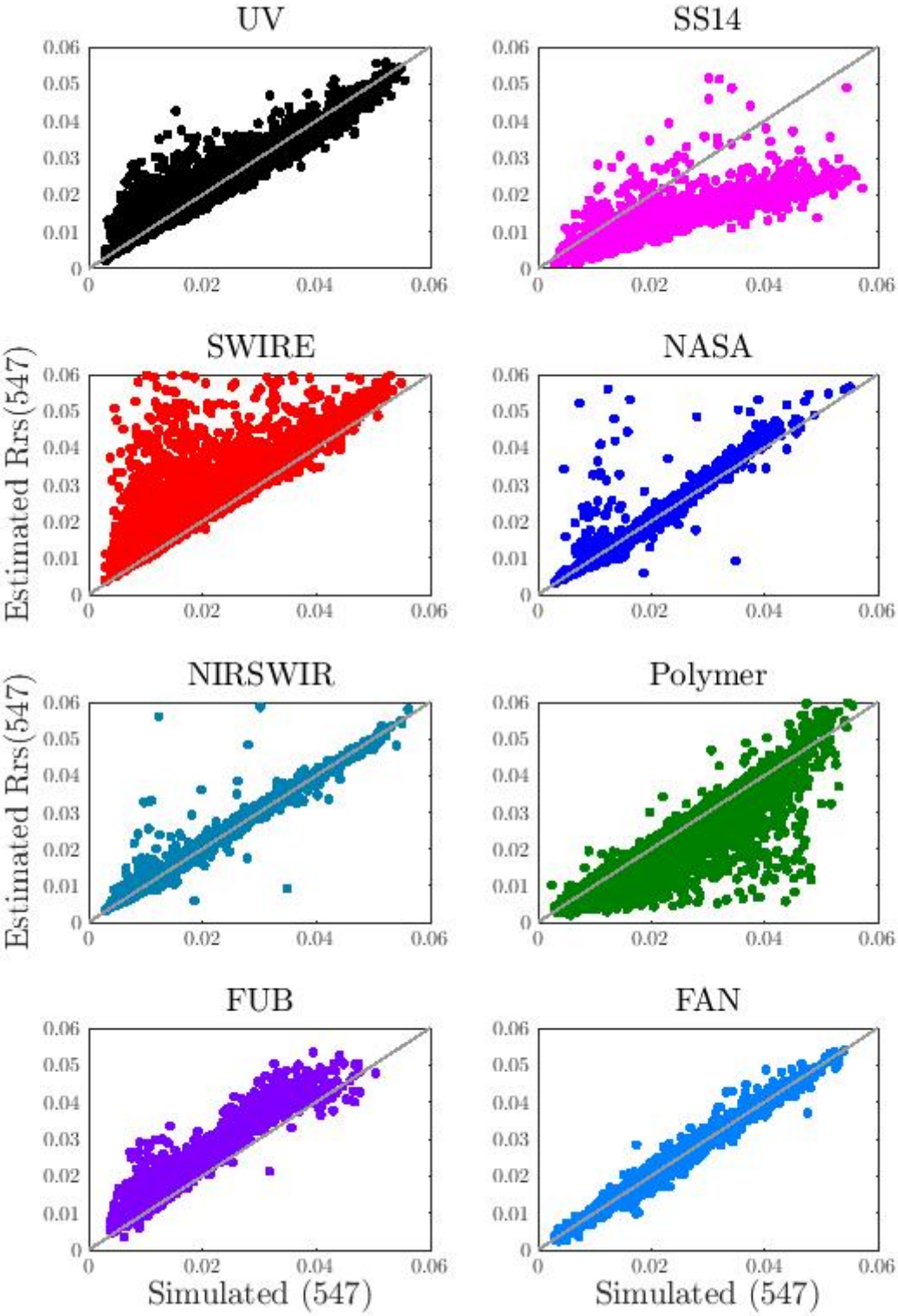
UV
SS14
SWIRE
NASA
NIRSWIR
Polymer
FUB
FAN
Estimated Rrs(547)
Estimated Rrs(547)
Simulated (547)
Simulated (547)
0
0.01
0.02
0.03
0.04
0.05
0.06

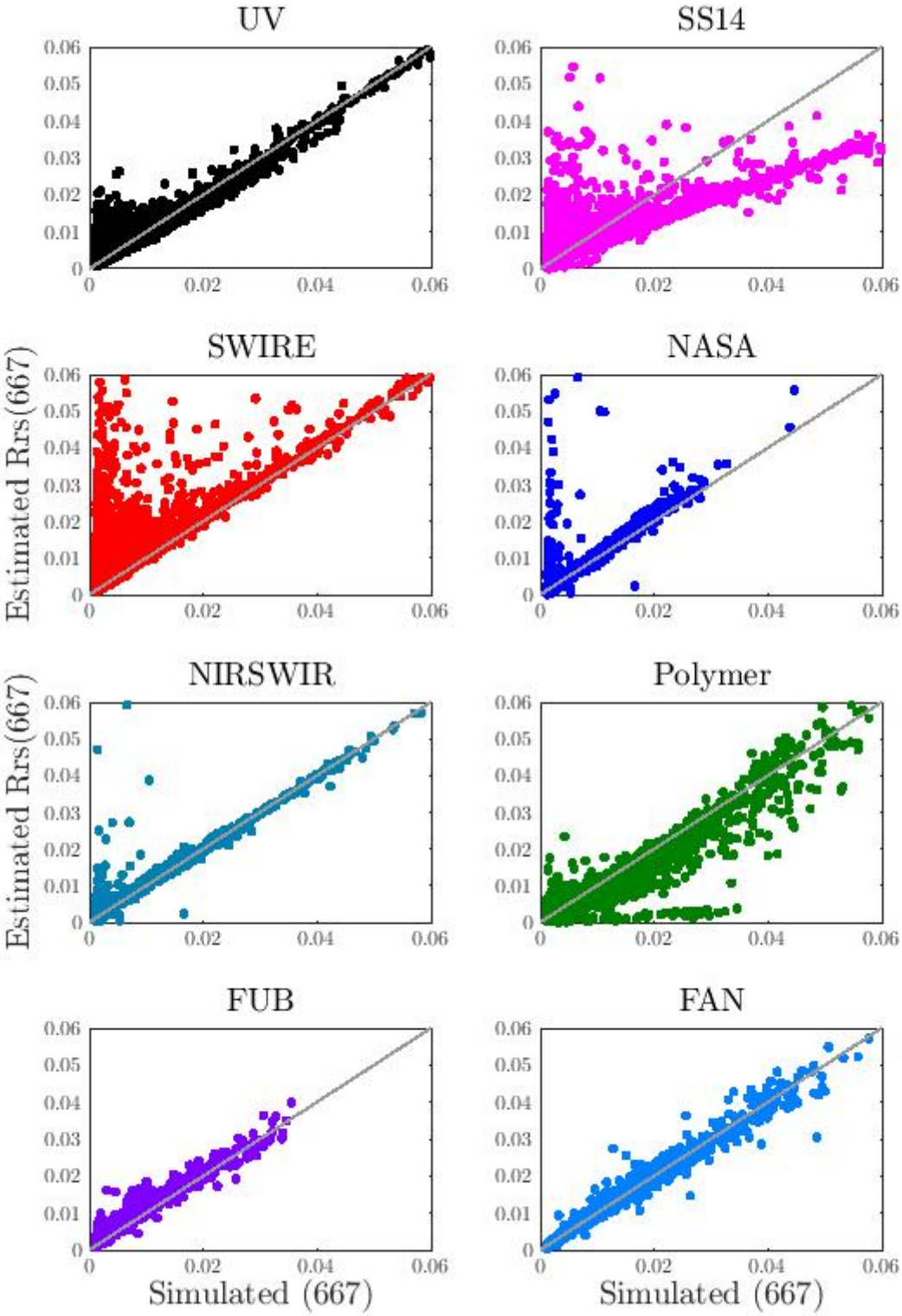
UV
SS14
SWIRE
NASA
NIRSWIR
Polymer
FUB
FAN
Estimated Rrs(667)
Estimated Rrs(667)
Simulated (667)
Simulated (667)
0
0.01
0.02
0.03
0.04
0.05
0.06